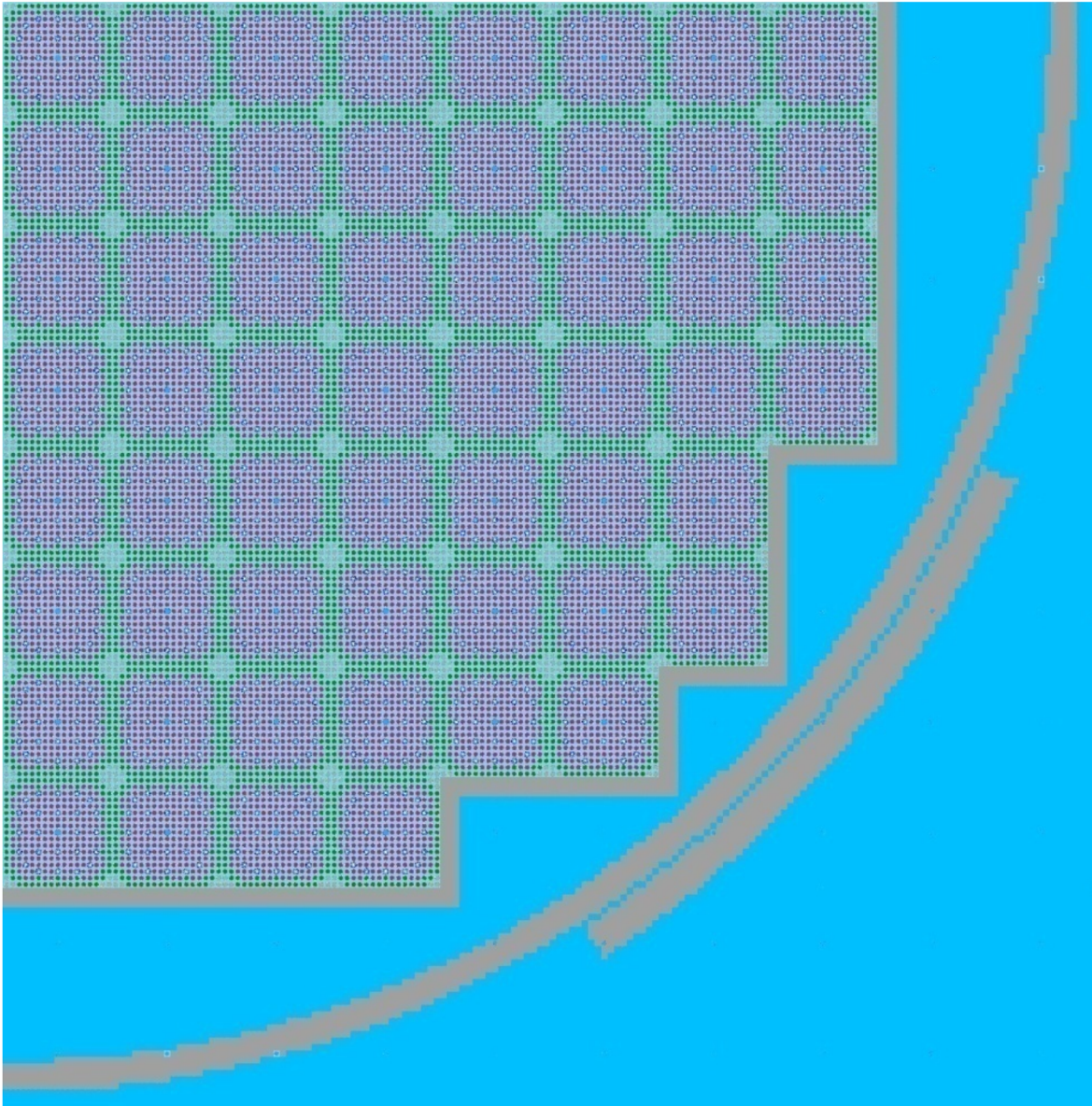


CASMO5 PWR Methods and Validation Report



Prepared by:  Digitally signed by Brandon Haugh
Date: 2015.10.22 08:39:26 -04'00'

Brandon P. Haugh, Senior Engineer Date

Prepared by:  Rodolfo M Ferrer
2015.10.26 07:12:19 -06'00'

Rodolfo M. Ferrer, Senior Engineer Date

Reviewed by: **Joel Rhodes III** Digitally signed by Joel Rhodes III
Date: 2015.11.02 07:21:04 -07'00'

Joel D. Rhodes, III, Methods Manager Date

Approved by:  David Kropaczek
2015.11.02 09:36:44 -05'00'

Dave Kropaczek, President Date

Proprietary Statement

This report is proprietary to Studsvik Scandpower, Inc. (SSP). The recipient company and/or any of its employees shall not reproduce, copy, publish or otherwise disclose this report or the SSP information therein to any third party without written permission from SSP.

This report contains information proprietary to Studsvik Scandpower, Inc. (SSP). A nonproprietary version of this report has also been prepared for distribution to the United States Nuclear Regulatory Commission (NRC). To conform to the requirements of the Commission's regulations (10CFR2.390) concerning the protection of proprietary information submitted to the NRC, the proprietary information in the proprietary version of this document is contained within brackets {}; where the proprietary information has been deleted in the nonproprietary versions, only the brackets remain (to indicate that the information contained within the brackets in the proprietary versions has been deleted). Pursuant to 10CFR2.390(b)(1), justification for claiming the information being so designated is provided in the affidavit accompanying the transmittal of these documents.

Copyright Notice

This document bears a Studsvik Scandpower, Inc., copyright notice. No right to disclose, use, or copy any of the information in this document, other than by the U.S. Nuclear Regulatory Commission (NRC), is authorized without the express, written permission of Studsvik Scandpower, Inc.

The NRC is permitted to make the number of copies of the information contained in these reports that are needed for its internal use in connection with generic reviews and approvals, as well as the issuance, denial, amendment, transfer, renewal, modification, suspension, revocation, or violation of a license, permit, order, or regulation subject to the requirements of 10 CFR 2.390 regarding restrictions on public disclosure to the extent such information has been identified as proprietary by Studsvik Scandpower, Inc., copyright protection notwithstanding. Regarding nonproprietary versions of these reports, the NRC is permitted to make the number of additional copies necessary to provide copies for public viewing in appropriate docket files in public document rooms in Washington, DC, and elsewhere as may be required by NRC regulations. Copies made by the NRC must include this copyright notice in all instances and the proprietary notice if the original was identified as proprietary.

Abstract

The Studsvik Core Management System (CMS) codes are used to perform the neutronic and thermal hydraulic analysis needed for the design, optimization, and safety analysis of nuclear reactor cores. The system of codes consists of two main computational engines. These are the lattice physics code CASMO5 and the nodal diffusion theory code SIMULATE5.

This report summarizes the methodology and validation of the CASMO5 lattice physics code for use in modeling Pressurized Water Reactor fuel assemblies. The validation of CASMO5 was performed by comparing to computational benchmarks and experimental measurements.

Revision History

Revision 0	Original Release	January 2015
Revision 1	Corrected Transcription Error In Figure 3-32 and Figure 3-34. Locations 53-C2 and 52-C2.	October 2015

Table of Contents

<i>CASMO5 PWR Methods and Validation Report</i>	<i>i</i>
<i>Proprietary Statement</i>	<i>iii</i>
<i>Abstract</i>	<i>iv</i>
<i>Revision History</i>	<i>v</i>
<i>Table of Contents</i>	<i>vi</i>
<i>Table of Tables</i>	<i>viii</i>
<i>Table of Figures</i>	<i>ix</i>
1 Introduction	1
2 CASMO5 Methodology	2
2.1 Program Flow	3
2.2 Neutron Data Library	5
2.3 CASMO5 Methods	6
2.3.1 Thermal Expansion	6
2.3.2 The Resonance Calculation	7
2.3.2.1 Equivalence Theory	7
2.3.2.2 Dancoff Factors	8
2.3.3 The Micro-Group Calculation.....	10
2.3.4 The 2D Transport Calculation	11
2.3.4.1 The Method of Characteristics.....	12
2.3.4.2 The Linear Source Approximation.....	13
2.3.4.3 The Quadrature Set.....	13
2.3.4.4 Boundary Conditions.....	13
2.3.4.5 Ray Tracing for the 2D Transport Calculation	13
2.3.4.6 Acceleration the 2D Transport Calculation	14
2.3.4.7 Transport Cross Section and Anisotropic Scattering Model	14
2.3.5 The Fundamental Mode Calculation.....	15
2.3.6 The Burnup Calculation.....	15
2.3.6.1 The Power Normalization Factor	16
2.3.6.2 The Bateman Equations and CRAM Solution	17
2.3.6.3 Depletion Mesh.....	18
2.3.7 CASMO Edits	18
2.3.7.1 Expansion of Fluxes.....	19
2.3.7.2 Cross Section and Diffusion Coefficients.....	19
2.3.7.3 Neutron Balance	19
2.3.7.4 Reaction Rates and Power distribution.....	20
2.3.7.5 Detector Edits	21
2.3.7.6 Kinetic Data	22
2.3.7.7 Xenon and Samarium Data	23

2.3.7.8	Flux Discontinuity Factors	23
2.3.8	Baffle/Reflector Calculations	23
2.3.9	Submesh Data	25
2.3.10	Gamma Transport	25
2.3.10.1	Detector Responses	26
2.3.10.2	Energy Deposition	26
2.3.11	Multi-assembly Capability	26
2.3.12	Fuel Storage Rack Capability	26
3	CASMO5 Validation	28
3.1	Method of Analysis	28
3.1.1	Differences	28
3.1.2	Average	29
3.1.3	Root Mean Square Error (RMSE)	29
3.1.4	Standard Deviation	29
3.1.5	Mean Relative Pin Power Error	30
3.2	Measurement Comparisons	30
3.2.1	Critical Experiments	30
3.2.1.1	B&W 1810	30
3.2.1.2	B&W 1484	38
3.2.1.3	KRITZ-3	45
3.2.1.4	AEA Winfrith DIMPLE	55
3.2.1.5	TCA Reflector Experiments	70
3.2.2	Isotopic Measurements	73
3.2.2.1	Yankee Rowe Measurements	73
3.2.2.2	JAERI PWR Isotopic Benchmarks	83
3.3	Higher Order Code Validation and Computational Benchmarks	96
3.3.1	C5G7 MOX Lattice Benchmark	96
3.3.2	MCNP6 Uniform Lattice Reactivity Comparisons	97
4	Summary	106
5	References	107

Table of Tables

<i>Table 3-1: B&W 1810 CASMO5 Eigenvalue Results</i>	33
<i>Table 3-2: B&W 1810 CASMO5 Fission Rate Results</i>	34
<i>Table 3-3: B&W 1810 CASMO5 Fission Rate Summary Results</i>	34
<i>Table 3-4: B&W 1484 CASMO5 Eigenvalue Results for Non-Unit Cell Configurations</i>	43
<i>Table 3-5: B&W 1484 CASMO5 Eigenvalue Results for Unit Cell Configurations</i>	44
<i>Table 3-6: KRITZ-3 Core Configuration Summary</i>	46
<i>Table 3-7: KRITZ-3 CASMO5 Summary Eigenvalue Results</i>	49
<i>Table 3-8: KRITZ-3 CASMO5 Fission Rate Summary Results</i>	55
<i>Table 3-9: CASMO5 DIMPLE Eigenvalue Results</i>	68
<i>Table 3-10: CASMO5 DIMPLE Fission Rate Summary Results</i>	69
<i>Table 3-11: CASMO5 TCA Eigenvalue and β_{eff} Results</i>	71
<i>Table 3-12: CASMO5 TCA β_{eff}/l^* Comparison (Bare Water Reflected)</i>	71
<i>Table 3-13: CASMO5 TCA Reflector Reactivity Comparisons</i>	71
<i>Table 3-14: CASMO5 C5G7 Eigenvalue Comparison</i>	96
<i>Table 3-15: CASMO5 C5G7 Power Distribution Comparison</i>	97
<i>Table 3-16: CASMO5 C5G7 Power Distribution Statistics</i>	97
<i>Table 3-17: CASMO5 BOL Reactivity Benchmark vs. MCNP6, Global Perturbations</i>	99
<i>Table 3-18: CASMO5 BOL Reactivity Benchmark vs. MCNP6, Control Rod Worth</i>	99
<i>Table 3-19: CASMO5 BOL Reactivity Benchmark vs. MCNP6, Integral Absorbers</i>	100
<i>Table 3-20: CASMO5 BOL Reactivity Benchmark vs. MCNP6, Discrete Absorbers</i>	101
<i>Table 3-21: IFBA Fission Rate Comparison Summary</i>	105

Table of Figures

Figure 2-1 CASMO5 Program Flow	3
Figure 2-2 Pin Cell Geometry with Reflective Boundary Conditions (CASMO5)	9
Figure 2-3 Circularized Pin Cell Geometry with White Boundary Conditions.....	9
Figure 2-4 Flow of Micro-Group Calculation.....	11
Figure 2-5 Calculation sequence in the CASMO Predictor-Corrector scheme.....	16
Figure 2-6 CASMO5 Reflector/Baffle model	25
Figure 3-1: B&W 1810 Core 3 Geometry.....	31
Figure 3-2: B&W 1810 Core 18 Geometry.....	32
Figure 3-3: B&W 1810 Core 1 Central Assembly Fission Rate Comparison.....	35
Figure 3-4: B&W 1810 Core 5 Central Assembly Fission Rate Comparison.....	35
Figure 3-5: B&W 1810 Core 12 Central Assembly Fission Rate Comparison.....	36
Figure 3-6: B&W 1810 Core 14 Central Assembly Fission Rate Comparison.....	36
Figure 3-7: B&W 1810 Core 18 Central Assembly Fission Rate Comparison.....	37
Figure 3-8: B&W 1810 Core 20 Central Assembly Fission Rate Comparison.....	37
Figure 3-9: B&W 1484 Core I Geometry.....	39
Figure 3-10: B&W 1484 Core II Geometry.....	40
Figure 3-11: B&W 1484 Core V Geometry	41
Figure 3-12: B&W 1484 Core XII Geometry	42
Figure 3-13: B&W 1484 CASMO5 Eigenvalue vs. Critical Height	45
Figure 3-14: KRITZ-3 Small Water Hole Model Geometry (U-WH1).....	47
Figure 3-15: KRITZ-3 Large Water Hole Model Geometry (U-WH2)	48
Figure 3-16: KRITZ-3 CASMO5 Eigenvalue vs. Temperature	49
Figure 3-17: KRITZ-3 U-WH1 Fission Rate Comparison Map (229.0°C, 1006 ppm).....	50
Figure 3-18: KRITZ-3 Pu-WH1 Fission Rate Comparison Map (223°C, 990ppm).....	51
Figure 3-19: KRITZ-3 U-WH2 Fission Rate Comparison Map (229°C, 959ppm).....	52
Figure 3-20: KRITZ-3 Pu-WH2 Fission Rate Comparison Map (25°C, 1122 ppm).....	53
Figure 3-21: KRITZ-3 Pu-WH2 Fission Rate Comparison Map (231°C, 949 ppm).....	54
Figure 3-22: DIMPLE Geometry Overview.....	56
Figure 3-23: DIMPLE S06A Fission Rate Measurement Locations.....	57
Figure 3-24: DIMPLE S06B Fission Rate Measurement Locations.....	58
Figure 3-25: S06A U235 Fission Rate Distribution (Upper Left Assembly of SE Quadrant).....	59
Figure 3-26: S06A U235 Fission Rate Distribution (Lower Left Assembly of SE Quadrant).....	60
Figure 3-27: S06A U235 Fission Rate Distribution (Lower Right Assembly of SE Quadrant).....	61
Figure 3-28: S06A U238 Fission Rate Distribution (Lower Left Assembly of SE Quadrant).....	62
Figure 3-29: S06A U238 Fission Rate Distribution (Lower Right Assembly of SE Quadrant).....	63
Figure 3-30: S06B U235 Fission Rate Distribution (Upper Left Assembly of SE Quadrant)	64
Figure 3-31: S06B U235 Fission Rate Distribution (Lower Left Assembly of SE Quadrant)	65
Figure 3-32: S06B U235 Fission Rate Distribution (Lower Right Assembly of SE Quadrant).....	66
Figure 3-33: S06B U238 Fission Rate Distribution (Lower Left Assembly of SE Quadrant)	67
Figure 3-34: S06B U238 Fission Rate Distribution (Lower Right Assembly of SE Quadrant).....	68
Figure 3-35: TCA Reflector Experiment Configuration	70
Figure 3-36: TCA Critical Steel Reflector Reactivity Effect.....	72
Figure 3-37: TCA Critical Steel/Water Reflector Reactivity Effect.....	72
Figure 3-38: Yankee Rowe U232 CASMO5 Comparison to Measurement	74
Figure 3-39: Yankee Rowe U234 CASMO5 Comparison to Measurement	74
Figure 3-40: Yankee Rowe U235 CASMO5 Comparison to Measurement	75
Figure 3-41: Yankee Rowe U236 CASMO5 Comparison to Measurement	76
Figure 3-42: Yankee Rowe U238 CASMO5 Comparison to Measurement	76
Figure 3-43: Yankee Rowe Np237 CASMO5 Comparison to Measurement.....	77

Figure 3-44: Yankee Rowe Pu236 CASMO5 Comparison to Measurement.....	77
Figure 3-45: Yankee Rowe Pu238 CASMO5 Comparison to Measurement.....	78
Figure 3-46: Yankee Rowe Pu239 CASMO5 Comparison to Measurement.....	78
Figure 3-47: Yankee Rowe Pu240 CASMO5 Comparison to Measurement.....	79
Figure 3-48: Yankee Rowe Pu241 CASMO5 Comparison to Measurement.....	80
Figure 3-49: Yankee Rowe Pu242 CASMO5 Comparison to Measurement.....	80
Figure 3-50: Yankee Rowe Am241 CASMO5 Comparison to Measurement	81
Figure 3-51: Yankee Rowe Am243 CASMO5 Comparison to Measurement	81
Figure 3-52: Yankee Rowe Cm242 CASMO5 Comparison to Measurement	82
Figure 3-53: Yankee Rowe Cm244 CASMO5 Comparison to Measurement	82
Figure 3-54: JAERI Isotopic Comparisons to CASMO5 for Sample SF95 Fission Products	84
Figure 3-55: JAERI Isotopic Comparisons to CASMO5 for Sample SF95 Actinoids	85
Figure 3-56: JAERI Isotopic Comparisons to CASMO5 for Sample SF96 Fission Products	86
Figure 3-57: JAERI Isotopic Comparisons to CASMO5 for Sample SF96 Actinoids	87
Figure 3-58: JAERI Isotopic Comparisons to CASMO5 for Sample SF97 Fission Products	88
Figure 3-59: JAERI Isotopic Comparisons to CASMO5 for Sample SF97 Actinoids	89
Figure 3-60: JAERI Isotopic Comparisons to CASMO5 for Sample 91E07 Fission Products	90
Figure 3-61: JAERI Isotopic Comparisons to CASMO5 for Sample 91E07 Actinoids	90
Figure 3-62: JAERI Isotopic Comparisons to CASMO5 for Samples 89G01, 89G03 and 89G05 Fission Products.....	91
Figure 3-63: JAERI Isotopic Comparisons to CASMO5 for Samples 89G01, 89G03 and 89G05 Gadolinium Isotopes.....	92
Figure 3-64: JAERI Isotopic Comparisons to CASMO5 for Samples 89G01, 89G03 and 89G05 Actinoids.....	93
Figure 3-65: JAERI Isotopic Comparisons to CASMO5 for Samples 89G08, 89G10 Fission Products	94
Figure 3-66: JAERI Isotopic Comparisons to CASMO5 for Samples 89G08, 89G10 Actinoids	95
Figure 3-67: C5G7 Benchmark Geometry	96
Figure 3-68: CASMO5 vs. MCNP6 Moderator Temperature Defect.....	102
Figure 3-69: CASMO5 vs. MCNP6 Doppler Defect.....	102
Figure 3-70: W15x15 Hot Fission Rate Comparison, 16 IFBA @ 3.0 mg/cm ¹⁰ B	103
Figure 3-71: W15x15 Hot Fission Rate Comparison, 148 IFBA @ 3.0 mg/cm ¹⁰ B	103
Figure 3-72: W17x17 Hot Fission Rate Comparison, 32 IFBA @ 3.0 mg/cm ¹⁰ B	104
Figure 3-73: W17x17 Hot Fission Rate Comparison, 200 IFBA @ 3.0 mg/cm ¹⁰ B	104

1 INTRODUCTION

The objectives of this report are to briefly describe the computational methods and models of CASMO5 to be validated, to describe the intended applications of these models in the preparation of cross-sections for use in other CMS codes (i.e. CMSLINK and SIMULATE), and to demonstrate the accuracy of CASMO5 by comparing calculated data to measurements and higher order computer codes.

The qualification is intended to allow the use of CASMO5 for all PWR fuels with the following attributes:

- Pin lattice geometries ranging from 14x14 to 17x17 including both large and small water hole designs.
- Integral burnable absorbers types: Gadolinia (Gd_2O_3) and IFBA (ZrB_2).
- Discrete absorber types: WABA, B_4C - AlO_3 , Boron Silicate Glass and Hafnium Suppression Rods.
- Control Rod absorber types: B_4C , Ag-In-Cd, W and Hafnium.
- Low enriched, ≤ 5.0 wt% ^{235}U , Uranium Oxide (UO_2) fuel.
- Soluble Boron in the coolant.
- In-Core Detector types of movable fission chambers and fixed designs.

In the instance where new fuel designs are developed that fall outside of the listed attributes, only significant changes need to be evaluated. What is significant could be a large deviation in fuel enrichments and/or materials, burnable absorber materials or significant geometry changes (e.g. non-square lattice).

Beyond strictly validating the accuracy of CASMO5, the comparisons to measurements and higher order codes in this report provide data for the construction of uncertainty factors by either: customers (as an element of non-Studsvik uncertainty factor methodologies) or as part of a forthcoming uncertainty methodology developed by Studsvik specifically for the CMS system.

2 CASMO5 METHODOLOGY

CASMO5 is a multigroup two-dimensional transport theory code for burnup calculations on Pressurized Water Reactor (PWR) assemblies or simple pin cells. The code handles a geometry consisting of cylindrical fuel rods of varying composition in a square pitch array with allowance for absorber-loaded fuel rods, Integral Fuel Burnable Absorber (IFBA), burnable absorber rods, cluster control rods, in-core instrument channels, and water gaps. Reflector and baffle calculations can also be performed with CASMO5.

CASMO5 incorporates the direct microscopic depletion of burnable absorbers into the main calculation and a fully heterogeneous model is used for the two-dimensional transport calculation.

Some characteristics of CASMO5 are:

- The two-dimensional transport solution is based upon the Method of Characteristics (MoC) with a linear source approximation.
- The multigroup energy discretization can be carried out in a number of different energy group structures, with the finest structure using 586 groups and the default for the MoC calculation using 19 groups for UO₂ fuel and 35 groups for MOX.
- Nuclear data for CASMO5 are collected in a library containing microscopic cross sections in 586 energy groups. Neutron energies cover the range from 10⁻⁵ eV to 20 MeV.
- CASMO5 can accommodate non-symmetric fuel assemblies. It can perform the calculations in half, quadrant, or octant symmetry.
- Absorber rods or water holes covering 1x1, 2x2, 3x3, or 4x4 pin cell positions are allowed within the assembly.
- Thermal expansion of dimensions and densities is performed.
- Effective resonance cross sections are calculated individually for each fuel pin.
- Microscopic depletion is calculated in each fuel and burnable absorber pin.
- The neutron transport and burnup calculations are coupled via a predictor-corrector approach which greatly improves accuracy. This is particularly important when burnable poison rods are involved. A special quadratic depletion model is used for lattices containing gadolinium. The burnup equations are solved with the Chebyshev Rational Approximation Method (CRAM).
- CASMO5 generates output edits of few-group cross sections and reaction rates for any region of the assembly. An ASCII card image file (CI-file) is created for linking to various diffusion theory core analysis programs, e.g., CMSLINK/SIMULATE.
- Reflector calculations are performed and discontinuity factors are calculated at the assembly boundaries and for reflector regions.
- CASMO5 can perform an 18-group gamma transport calculation if required.
- Multi-assembly calculations in CASMO5 for BWRs and PWRs use the same transport theory methodology (Method of Characteristics) as the single assembly calculations.

2.1 Program Flow

The simplified flow of calculations in the CASMO5 program is shown in the diagram illustrated in Figure 2-1.

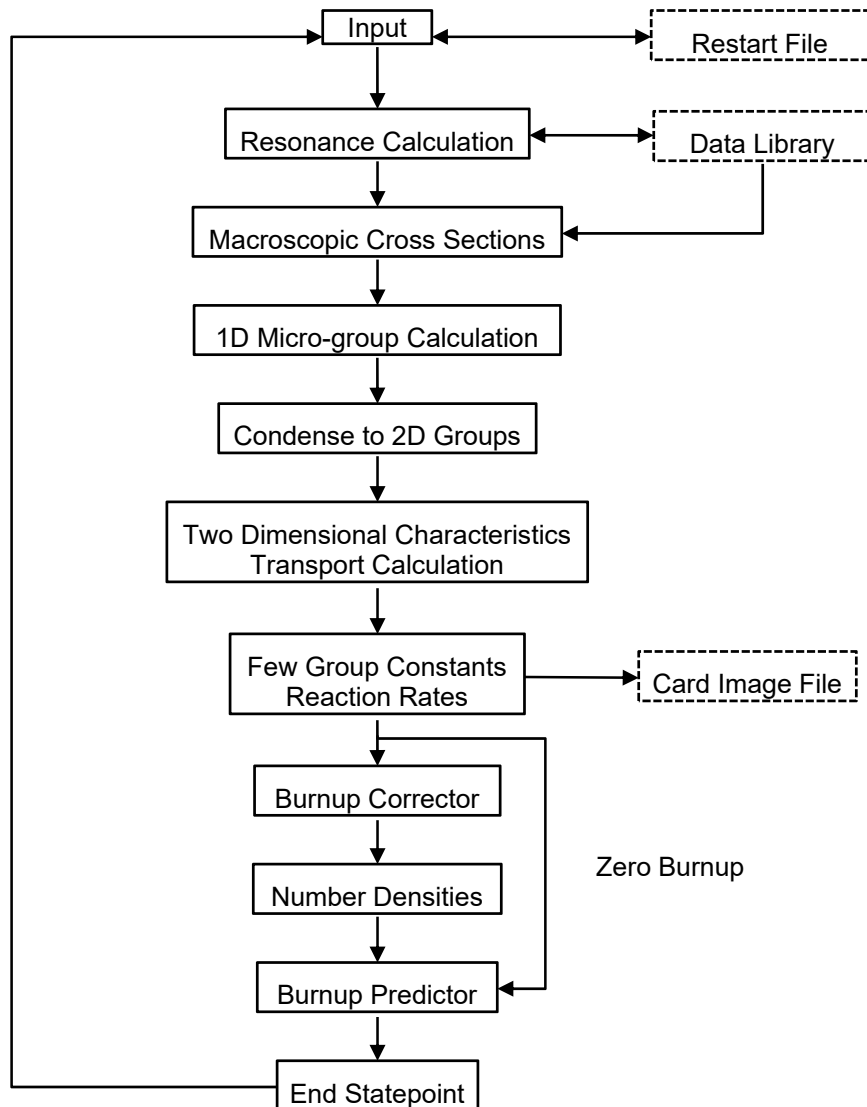


Figure 2-1 CASMO5 Program Flow

In the initial steps of the calculation the macroscopic group cross sections are prepared for the micro-group calculations. The nuclear data library in 586 energy groups is an integral part of the code system and macroscopic cross sections are directly calculated from the densities, geometries, etc., provided in the user's input.

The effective cross sections in the resonance energy region for resonance absorbers are calculated using an equivalence theorem which relates tabulated effective resonance integrals

for each resonance absorber in each resonance group to the particular heterogeneous problem. The equivalence expression is derived from rational approximations for the fuel self-collision probability. The resonance integrals obtained from the equivalence theorem are used to calculate effective absorption and fission cross sections. The “shadowing” effect between different pins is taken into account through the use of Dancoff factors that are calculated internally by CASMO5.

The 586 group neutron data library has 42 thermal groups (below 0.625 eV) and 375 fine groups between 0.625 eV and 10.0 eV. The resonance region (the energy region where data is explicitly shielded in CASMO5) is defined to lie between 10 eV and 9118 eV. Absorption above 9118 eV is assumed to be unshielded. The 1 eV resonance in Pu-240, the 6.67 eV resonance in U-238, and other low energy resonances are adequately covered by the concentration of narrow epithermal groups around these resonances and are consequently excluded from the special resonance treatment.

The effective cross sections are used in a series of 1D, collision probability micro-group calculations to obtain detailed neutron energy spectra in 586 energy groups for use in the energy condensation of the cross sections.

The 1D micro-group calculation is repeated for each pin type to determine individual spectra of pins containing fuel of different enrichments. To provide micro-group spectra for condensation of an absorber pin cell, a micro-group calculation is carried out for the absorber rod surrounded by coolant and a buffer region representing the surrounding fuel pins. The same procedure is used to determine micro-group spectra for water holes within the assembly.

The data generated in the previous steps constitute the input to the heterogeneous, two-dimensional characteristics-based transport calculation, normally performed in 19 or 35 energy groups, which calculates the eigenvalue and the associated flux distribution.

Isotopic depletion as a function of burnup is calculated for each fuel pin and for each region containing a burnable absorber.

The burnup calculation is performed using a predictor-corrector approach. For each burnup step, the solution to the Bateman equations is calculated twice, first using the spectra at the start of the step, and then after a new spectrum calculation, using the spectra at the end of the step. Average number densities from these two calculations are then used as starting values for the next burnup step. Important gadolinium isotopes, e.g., Gd-155, Gd-157, are treated with a special quadratic depletion model.

CASMO5 has a flexible output and edits the eigenvalue, the power distribution, reaction rates and few-group parameters for use in core calculations. The output also contains flux discontinuity factors for assembly interfaces and reflector regions. These discontinuity factors can be used by SIMULATE in two, or multi-group diffusion theory in order to preserve net currents calculated by the CASMO5 multigroup transport solution.

Reflector data, including data for homogenized baffle and water, are accurately generated by a two-dimensional, 95-group calculation modeling one segment plus the reflector on one side.

CASMO5 can also calculate prompt and delayed gamma sources from (n, γ) reactions, and solve the 18-group, 2D gamma transport problem so that the gamma detector response may be calculated.

Multi-assembly calculations are performed by looping over the various modules (resonance calculation, micro-group calculation, etc.) for each segment and then combining the whole configuration for the two-dimensional transport calculation.

2.2 Neutron Data Library

The CASMO5 neutron data library is based on ENDF/B-VII.1 data files (supplemented with TENDL-2012 data) and was processed with NJOY-94.105 [1] and NJOY-2012.8 [2]. In addition, other auxiliary Studsvik programs were used to calculate cross sections for complex materials and to extract and handle decay constants, fission yields, fission spectra, and delayed neutron data. A full description of the library is available in the CASMO5 User's manual [3].

The library contains cross sections, decay constants, and fission yields for 1095 nuclides/materials, most of which are individual nuclides. Some materials are elements with natural isotopic composition, and cross sections for these materials were obtained by adding cross sections for the constituent nuclides according to their natural abundance. Other materials, such as construction materials, are mixtures of elements. Cross sections for these materials are obtained by adding the cross sections of the constituent elements according to the composition of the material. Since many natural elements that were present in ENDF/B-VI evaluation are no longer present in the ENDF/B-VII evaluation, e.g., natural Zr and natural Si, the isotopic constituents for these elements have been placed on the library, and CASMO5 will mix them according to natural abundances.

Microscopic neutron cross sections are tabulated in 586 energy groups. This group structure fulfills the following requirements:

- The 128 fast groups provide enough detail in the fast energy region to calculate the leakage and fast fission accurately.
- The 41 resolved resonance groups (10.0 eV to 9118 eV) provide correct flux levels as a function of energy for the calculation of resonance absorption.
- The 392 narrow, constant energy width groups explicitly map out resonances in the 10 eV to 0.2 eV range.
- The 25 additional thermal groups below 0.2 eV have energy widths of 0.01 or 0.005 eV, and make the thermal cross sections independent of the weighting spectrum used for their generation.

The CASMO5 neutron data libraries contain absorption, fission, ν *fission, transport, and scattering cross sections. Data are tabulated as functions of temperature when needed. Shielded resonance integrals versus background cross section and temperature are tabulated for resonance absorbers (typically 4 to 10 temperatures and up to 18 background cross section sets).

The libraries further contain decay constants for fission products and heavy nuclides, and fission product yield values. The structure of the fission product representation determines whether independent or cumulative yield is used for each fission product. The selected structure and yield values give yield sums for each fission precursor very close to 2.0.

The CASMO5 neutron data library contains fission yield data for 27 fissioning species. Nuclides that are on the southeast edge of the CASMO depletion chains are represented with cumulative yield, whereas other nuclides are represented with an independent yield. The cumulative yield for a nuclide is the independent yield of that nuclide plus the sum of independent yields to radioactive decay precursors of that nuclide, accounting for decay branching fractions.

In summary, the CASMO5 library has these additional attributes:

- There are 119 heavy nuclides ($Z > 86$), where Z is the atomic number.
- There are 491 fission products ($30 \leq Z \leq 67$), where Z is the atomic number.
- There are potentially 2341 reactions modeled (when extended depletion chains are activated).
- This library has no yield/decay models as nuclides that were previously only yield/decay now have at least an absorption-only model (using TENDL-2012 data).
- Fission products with resonance data have been shielded down to 50 barns.
- The CASMO5 library primarily implements ENDF/B-VII.1 fission yields, radioactive decay, and delayed neutron data.

2.3 CASMO5 Methods

2.3.1 Thermal Expansion

Thermal expansion of dimensions and densities is performed automatically by CASMO5. Hence, the user must input cold dimensions in the input file so that automatic thermal expansion is done correctly. In certain instances, such as when the user specifies a material composition using nuclide number densities in the input or when a reflector or fuel storage rack calculation is requested, the thermal expansion will be turned off by the code.

CASMO5, CMSLINK, and SIMULATE are designed to work together in this regard. CASMO5 performs the thermal expansion calculation such that hot cross sections and pin power data are calculated based on conditions representative of core operation (nominal conditions are input to CASMO5). In SIMULATE, all geometrical data (e.g., node height and width) are based on cold dimensions and there is no thermal expansion calculation required, since the effect of thermal expansion is already implicit in the cross sections and the pin library data. The assumption here is that the error introduced by using the cold dimensions for the 3D nodal mesh is small.

2.3.2 The Resonance Calculation

CASMO5 performs an explicit resonance treatment for energies between 10 eV and 9118 eV. Resonance absorption (and fission) above 111.09 keV is regarded as being unshielded. The 392 narrow energy groups explicitly map out resonances in the 10 eV to 0.2 eV range and are consequently excluded from the special resonance treatment. The library description in the User's manual [3] indicates which nuclides are treated as resonance absorbers.

2.3.2.1 Equivalence Theory

Standard equivalence theory is used to relate the heterogeneous resonance absorption problem to an equivalent homogeneous problem. The group-averaged absorption cross sections are defined as (pp. 923 in [4])

$$\sigma_{a,g} = \frac{\int_{E_g}^{E_{g-1}} \sigma_a(E) \phi(E) dE}{\int_{E_g}^{E_{g-1}} \phi(E) dE} \quad (2.1)$$

where $\sigma_a(E)$ and $\phi(E)$ are the microscopic absorption cross section and the scalar flux spectrum as a function of the continuous energy variable E , respectively. The energy group g is defined by $E_g \leq E < E_{g-1}$. Since the actual flux spectrum is not known, an approximate spectrum must be used in order to evaluate Eq. (2.1).

Standard equivalence theory assumes the Narrow Resonance (NR) approximation for the flux spectrum $\phi(E)$ (pp. 992-993 in [4])

$$\phi(E) = \left[1 - P_{ff} + \frac{\sigma_p}{\sigma_t(E)} P_{ff} \right] \frac{1}{E} \quad (2.2)$$

where σ_p and $\sigma_t(E)$ are the potential and total microscopic cross sections, and P_{ff} is the fuel-to-fuel collision probability (see the text preceding Eq. 94 in [4] for the derivation of this equation). Substituting Eq. (2.2) into Eq. (2.1) gives

$$\sigma_{a,g} = \frac{\int_{E_g}^{E_{g-1}} \left[1 - P_{ff} + \frac{\sigma_p}{\sigma_t(E)} P_{ff} \right] \sigma_a(E) \frac{dE}{E}}{\int_{E_g}^{E_{g-1}} \left[1 - P_{ff} + \frac{\sigma_p}{\sigma_t(E)} P_{ff} \right] \frac{dE}{E}} \quad (2.3)$$

Rearranging the numerator in Eq. (2.3) results in the definition of the resonance integral in the narrow resonance approximation

$$RI = \int_{E_g}^{E_{g-1}} \frac{\sigma_a(E)}{\sigma_t(E)} \left[(1 - P_{ff}) \sigma_t(E) + \sigma_p P_{ff} \right] \frac{dE}{E} \quad (2.4)$$

A two-term rational approximation for the fuel-to-fuel collision probability [5]

$$P_{ff} = X \left(\frac{\beta}{X + \alpha_1} + \frac{1 - \beta}{X + \alpha_2} \right) \quad (2.5)$$

Substituting Eq. (2.5) into Eq. (2.3) results in the following expression

$$\sigma_{a,g} = \frac{RI_{1,g} + RI_{2,g}}{\tau_g - \frac{RI_{1,g}}{\sigma_p + \alpha_1 \sigma_e} - \frac{RI_{2,g}}{\sigma_p + \alpha_2 \sigma_e}} \quad (2.6)$$

where $\tau_g = \int_{E_g}^{E_{g-1}} \frac{dE}{E}$ is the group lethargy width. The terms in the denominator have been simplified by assuming no resonance scattering, i.e. $\sigma_t(E) = \sigma_p + \sigma_a(E)$.

The effective resonance integrals, $RI_{1,g}$ and $RI_{2,g}$, are obtained by interpolation from tables of homogeneous resonance integrals in the data library. The homogeneous resonance integrals are tabulated with potential cross section σ_p and temperature T as independent variables and the interpolation is based on a $\sqrt{\sigma_p}$ and \sqrt{T} dependence. A first-order correction for the interaction associated with the presence of several nuclides in the same material is included. This is known as the resonance interference model [6].

2.3.2.2 Dancoff Factors

Characteristic-based Dancoff factors are calculated using the MoC method on a single pin cell geometry [7]. The classic definition of a Dancoff factor is (see Eq. (11) in [6])

$$D = \Gamma_\infty = \lim_{\Sigma_f \rightarrow \infty} \frac{1 - P_{ff}}{1 - p_{ff}} \quad (2.7)$$

where P_{ff} and p_{ff} are fuel-to-fuel collision probabilities in an infinite array of pins and in an isolated pin, respectively.

The method used in previous versions of CASMO to calculate Dancoff factors uses this definition and region-to-region collision probabilities obtained from a circularized problem (Wigner-Seitz approximation) with a white boundary condition (Figure 2-3). The new characteristics-based method in CASMO5 calculates Dancoff factors using the same definition, but with the two collision probabilities, P_{ff} and p_{ff} , obtained directly from the square pin cell geometry problem, (Figure 2-2). For the characteristics solution of the pin cell transport problem, the total cross section of fuel region (region 1) Σ_f is set to a large number to be consistent with the definition of Dancoff factor (infinite cross section) and a uniform, isotropic source q is assigned in that fuel region. A fixed source transport problem is then solved for the fluxes in the fuel region ϕ_f using the method of characteristics. This solution is repeated twice, once with a reflective boundary condition and another with a vacuum boundary condition.

Figure 2-2 Pin Cell Geometry with Reflective Boundary Conditions (CASMO5)

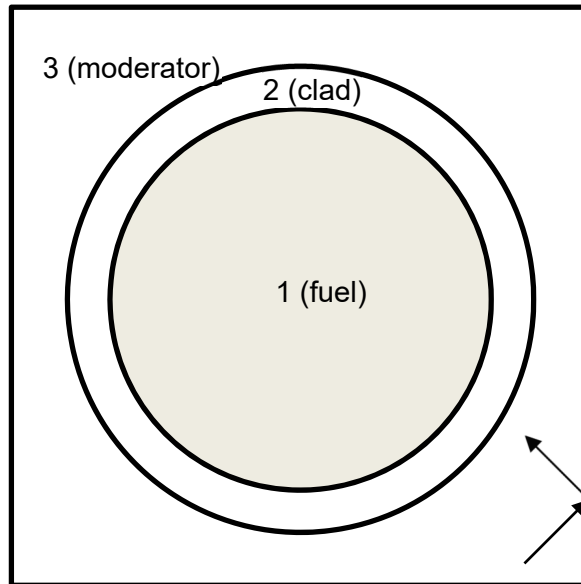
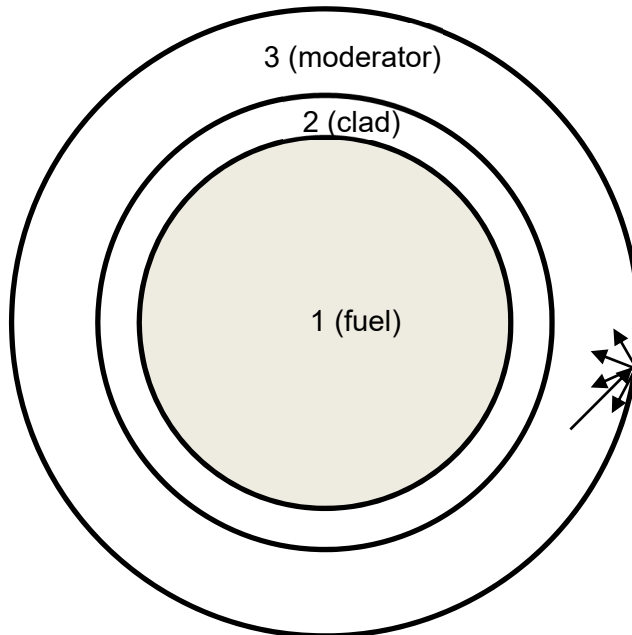


Figure 2-3 Circularized Pin Cell Geometry with White Boundary Conditions



These Dancoff factors are obtained assuming an infinite lattice of identical pins using reflective boundary conditions. Individual Dancoff factors for each pin are used to correct the “infinite lattice” Dancoff factor assumption by accounting for the shadowing of neighboring pin cells.

2.3.3 The Micro-Group Calculation

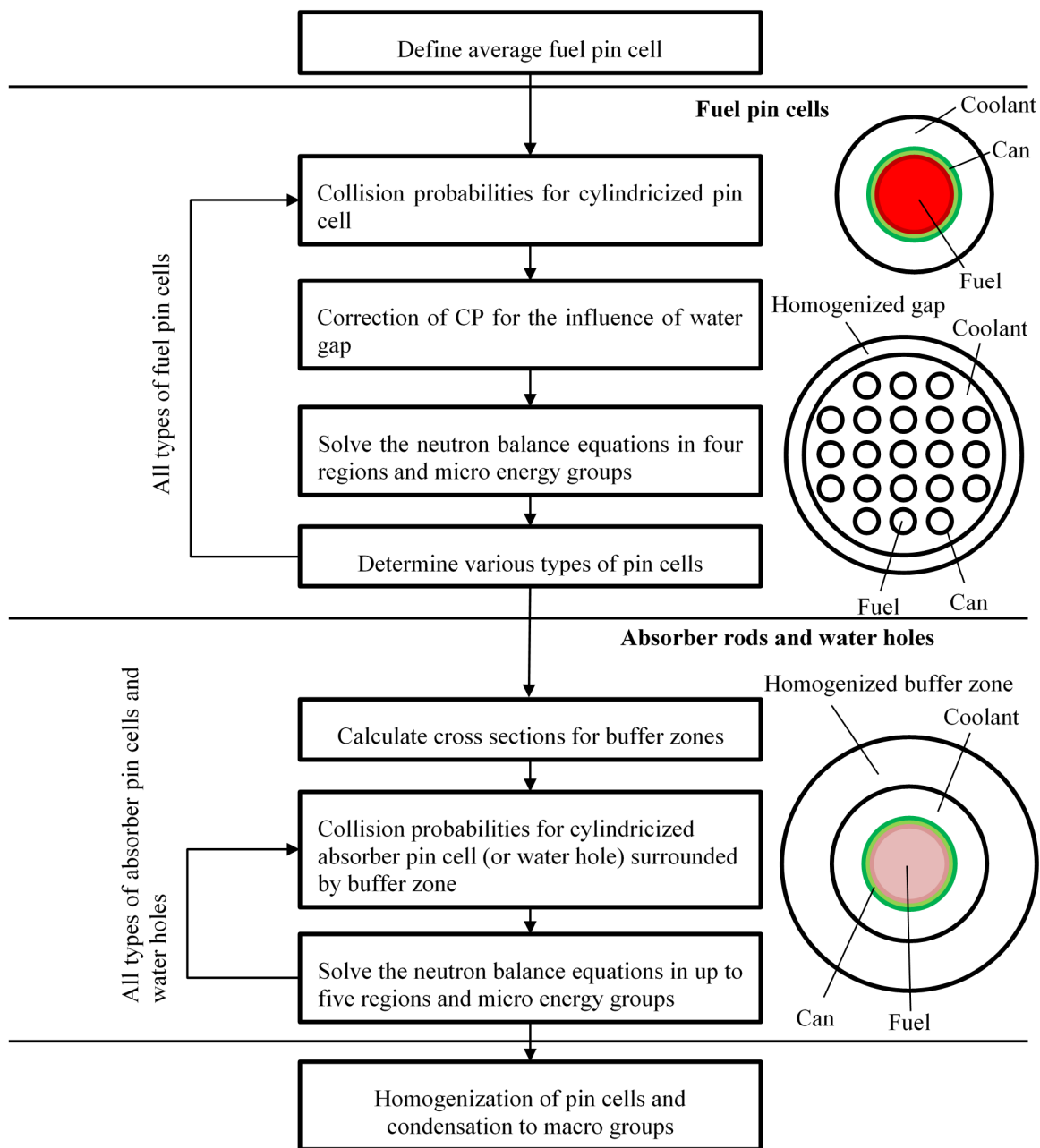
One of the primary objectives of CASMO5 is to generate multi-group data for SIMULATE. The accuracy of the data is dependent upon the accuracy of the CASMO flux distribution used to homogenize and collapse the cross sections. It is desirable, therefore, to have as accurate a flux distribution as possible. The most accurate solution may be obtained by modeling the true heterogeneous nature of the lattice in the energy group structure of the nuclear data library.

However, to decrease execution time, some of the detail must be removed from the problem, and this is achieved by performing the 2D lattice transport calculation in a smaller number of energy groups. At the same time, accuracy must not be compromised, and this requires that the cross sections in the smaller energy group structure be representative of those from the original group structure. To this end, the cross sections must be condensed with an appropriate flux spectrum.

The energy condensation scheme in CASMO5 consists of one-dimensional pin cell calculations performed before the 2D lattice calculation. The pin cell calculations are performed in the micro-group structure of the cross section library (586 groups).

Normally, a micro-group calculation is performed for each pin type in the fuel assembly. Collision probabilities are determined in a simplified geometry consisting of the different material regions of the pin type. Accurate collision probabilities for the cylindrical pin cell with flat source in each region are calculated using the FLURIG-2 method developed by Carlvik [9]. Normal fuel pins are modeled using either three or four regions (e.g., fuel, air, cladding and coolant). If the lattice being modeled contains water gaps outside the fuel assembly, an additional region representing the water gap (and box wall, if present) is added to the cell. This region creates the “softening” effect which the bypass region has on the flux distribution across the cell. For inert rods (e.g., water rods, guide tubes, etc.), a fuel-containing “buffer” region is added to the outside of the coolant and is used to drive the flux across the cell. Burnable absorber rods, specifically fuel rods containing gadolinium or erbium, are modeled using a geometry similar to that used for inert rods. The fuel region of the gadolinium rod, however, is automatically split into many annular subregions, used to represent the strong variations in the number density of the burnable absorber across the fuel region once the pin begins to deplete. A flow chart of the micro-group calculation is shown below.

Figure 2-4 Flow of Micro-Group Calculation



2.3.4 The 2D Transport Calculation

CASMO5 performs a two-dimensional, heterogeneous transport calculation on the entire lattice using a particular energy structure referred to as the “2D-group structure.” The spatial domain is discretized into pin cell sized regions referred to as “macro-regions.” Each macro-region contains the fine-mesh or “micro-regions”, in which the heterogeneous transport calculation is performed. Cross sections for each micro-region of the lattice are condensed to the 2D-group structure using the spectra from the micro-group pin cell calculation. The flux distribution throughout the lattice is

subsequently determined by solving the Boltzmann transport equation using the Method of Characteristics (MoC).

2.3.4.1 The Method of Characteristics

In the Method of Characteristics [4], parallel lines or ‘characteristics’ are overlaid on the spatial domain in discrete angular directions. Tracks or ‘segments’ are defined along each characteristic corresponding to regions where the flux is assumed to be constant (or linear) and the material cross section constant. The 2D transport equation is reduced to a one-dimensional ordinary differential equation (see p. 1105 in [4])

$$\frac{d\psi_{m,i}^g}{ds_m} + \Sigma_{tr,i}^g \psi_{m,i}^g = Q_{m,i}^g \quad (2.8)$$

where the notation follows standard usage and can be readily solved using integration by parts

$$\psi_{m,i}^g(s_m) = \psi_{m,i}^g(0)e^{-\Sigma_{tr,i}^g s_m} + \frac{Q_{m,i}^g}{\Sigma_{tr,i}^g} (1 - e^{-\Sigma_{tr,i}^g s_m}) \quad (2.9)$$

The resulting solution, referred to as the characteristics equation, is averaged over the track to obtain the balance equation

$$\bar{\psi}_{m,i}^g = \frac{Q_{m,i}^g}{\Sigma_{tr,i}^g} + \frac{\Delta_{m,i}^g}{\Sigma_{tr,i}^g s_{m,i}} \quad (2.10)$$

where $\Delta_{m,i}^g = \psi_{m,i}^g(0) - \psi_{m,i}^g(s_{m,i})$. The characteristics equation is also evaluated at the track endpoint in order to obtain a ‘propagation’ equation. Assuming the source and boundary conditions are fixed, or come from a previous iterate, the region-wise scalar flux is updated by performing a transport ‘sweep’ along every characteristic in every direction (both azimuthal and polar directions.) The track-average angular flux is obtained from the balance equation. The outgoing angular flux is subsequently computed from the propagation equation and is used as the incoming angular flux for the next source region. The scalar flux is ‘accumulated’ by computing the contribution of the track-average angular flux to the scalar flux

$$\phi_i^g = \frac{q_i^g}{\Sigma_{tr,i}^g} + \frac{4\pi}{\Sigma_{tr,i}^g V_i} \sum_m \omega_m \sin \theta_m \delta A_m \sum_k \Delta_{m,k,i}^g \quad (2.11)$$

The sources in each region are updated based on the latest scalar flux solution and this procedure continues until a convergence criteria is satisfied. In practice, various acceleration schemes are applied in order to reduce the total number of transport sweeps performed in a calculation. These are discussed in a later section below. In the process of performing the transport sweep, net currents and surface fluxes are also accumulated.

2.3.4.2 The Linear Source Approximation

The Method of Characteristic is capable of accurately representing the source region boundary (incoming and outgoing) angular flux. However, under the flat-source assumption, problems involving large regions with significant scattering, such as water reflector regions, may require many small flat-source regions in order to capture the spatially-varying source shape. If the size of the source regions becomes very small due to spatial refinement, the computational efficiency is decreased since the number of tracks to sweep increases rather quickly relative to the number of mesh regions. In order to circumvent these difficulties, CASMO5 uses a Linear Source (LS) method as the default transport solver [10]. The order of accuracy for the MoC under the flat source assumption can be improved by relaxing the constant source shape assumption in favor of a linearly-varying source along each track length and in the mesh cell.

2.3.4.3 The Quadrature Set

Quadrature sets used by the characteristics routine are generated internally by CASMO5. For a specified number of azimuthal and polar angles, the boundaries for each subdivision are distributed evenly. Evenly-spaced azimuthal directions are subsequently slightly updated to ensure perfect reflection (pp. 1145-1151 in [4]). The corresponding weights are also updated for each azimuthal direction.

The azimuthal angles are used to represent neutron motion in the x,y -plane of the problem. To model motion out of this plane, each azimuthal angle is modeled at a specified number of polar angles. Because two-dimensional problems have no material boundaries along the z -axis, neutron motion out of the plane of the problem will be the same in the upper hemisphere as it is in the lower hemisphere. Therefore, motion need only be tracked in one hemisphere.

By default, CASMO5 uses the Tabuchi-Yamamoto optimal quadrature up to 3 polar angles [11], and uses a standard Gauss-Legendre quadrature for more than 3 polar angles.

2.3.4.4 Boundary Conditions

The boundary conditions available in the CASMO5 MoC solution scheme are: mirror, periodic, black, and rotational boundary conditions. The mirror and black boundary conditions may also be referred to as reflective and vacuum boundary conditions, respectively. Boundary conditions can be specified for each side of the problem domain (west, south, east, and north.) By default the code will apply mirror boundary conditions to all four sides. Alternatively, the user can specify the boundary conditions for each of the sides through the code input.

2.3.4.5 Ray Tracing for the 2D Transport Calculation

The ray tracing routine determines the track lengths which pass through the various mesh of the problem in each azimuthal direction contained in the quadrature set. The program first passes through the geometry setup and assigns cell types to each individual cell. Cell types are determined, not only by what lies within a cell, but also by what lies around a cell.

Cell types are determined internally by the code and the user has no control over them. Each cell type has a ray tracing routine developed specifically for its own unique geometry. Any cell may contain embedded annular cylinders and/or slabs and arcs. Arcs may have their center of

curvature anywhere within the cell or within neighboring cells. Annular cylinders need not be centered within the cell.

Following the declaration of cell types, the code begins tracing through the system. Ray tracing takes place only for the azimuthal directions of motion. The resulting track lengths are then raised out of the plane of the problem to the various polar angles. For any given azimuthal direction, the tracing routine first determines the number of characteristics which begin along the x and y axes and then determines the origin of each characteristic along the boundary.

The code first determines what cell the track is crossing. Based on the cell type, the code proceeds to enter the appropriate tracing subroutine. Regardless of what lies within the cell, the tracing routines are primarily concerned with finding the intersections of lines and arcs with the characteristic as it passes through the cell. This ray-tracing approach is generally referred to as a modular ray-tracing [4], and offers significant computational efficiency in comparison to other methods.

2.3.4.6 Acceleration the 2D Transport Calculation

The non-linear iteration techniques commonly used in advanced nodal diffusion codes (to accelerate higher-order diffusion models with low order diffusion models) can also be used to accelerate directly the MOC transport solutions [12]. This can be achieved by superimposing a rectangular acceleration mesh on the heterogeneous geometry, and tallying volume-averaged scalar fluxes and surface-averaged net currents during each transport sweep. Following each transport sweep, a set of finite-difference-like, coarse-mesh diffusion (CMFD) equations are constructed on the rectangular mesh. Coarse-mesh cross sections are computed by flux-volume weighting cross sections of each heterogeneous sub-region contained in each coarse mesh. Diffusion-like coupling coefficients for the coarse-mesh equations are constructed to match the average net current (from the transport sweep) on each face of the rectangular mesh [12]

$$J_{M+}^g = -D_{M+}^g(\phi_{M+1}^g - \phi_M^g) - \tilde{D}_{M+}^g(\phi_{M+1}^g - \phi_M^g) \quad (2.12)$$

For simplicity (as well as for edits needed for CASMO) the fine-mesh diffusion acceleration is defined on the “pin cell” mesh. Since the dominance ratio of the diffusion problem is known to be independent of the diffusion solution mesh, it is natural to extend the single-level diffusion acceleration to a multi-level diffusion acceleration. For multi-assembly calculations in CASMO5 an additional coarse-mesh diffusion level is defined by the physical assembly mesh [12].

2.3.4.7 Transport Cross Section and Anisotropic Scattering Model

Traditionally, anisotropic scattering effects in CASMO5 have been modeled by use of a transport corrected P_0 transport cross section. Many codes approximate the transport cross section by using the P_1 out-scatter approximation, since it does not require the computation of the P_1 angular flux. Conversely, CASMO5 uses the P_1 in-scatter approximation to obtain the transport cross section by solving the P_n equation for a uniform fission spectrum source in a homogenous medium consisting of moderator material.

Anisotropic scattering is optionally available in the 2D transport solution from order 0 to 5 [7]. The P_n scattering cross section data for all relevant nuclides is available in the neutron cross section library. The MoC solutions in this case are very similar to the isotropic case, except that the source must be directional, and require the evaluation of angular flux moment in each direction through

the spherical harmonics expansion of the scattering kernel. In addition, angular flux moments are ‘accumulated’ during the transport sweep, instead of just a single scalar flux in the case of isotropic scattering.

2.3.5 The Fundamental Mode Calculation

In single assembly calculations a fundamental buckling mode [4], based on the diffusion approximation may be used for modifying the infinite lattice results obtained from the transport calculation to include the effects of leakage. The fundamental mode calculation is activated when generating data for SIMULATE-3. Conversely, the fundamental mode calculation is bypassed when generating SIMULATE5 (S5) data since S5 already takes into account the inter-assembly leakage *in situ*. The fundamental mode calculation is also bypassed in calculations involving multiple segments, reflectors, and fuel storage racks.

2.3.6 The Burnup Calculation

The CASMO5 burnup calculation is typically a two-step process. In going from the time t_{n-1} to t_n a “predictor” step is first taken using the fluxes obtained from the neutron calculation at t_{n-1} . The predictor step provides predicted number densities at t_n . The cross sections are then updated, and the new spectrum calculation gives fluxes to be used in a “corrector” step. The average value of the final number densities from the predictor and corrector steps become the initial number densities for the next burnup step (from t_n to t_{n+1}). The calculation sequence in the predictor-corrector scheme is illustrated by Figure 2-5.

The burnup calculations which are described in Sections 2.3.6.1-2.3.6.2 are identical for the predictor and corrector steps. Only the input parameters (being the one-group flux $\phi(t_{n-1})$, and the one-group cross sections $\sigma(t_{n-1})$ in the predictor step; and $\phi(t_n)$, and $\sigma(t_n)$ in the corrector step) differ between the two steps. The isotopic depletion is calculated and tracked separately in each fuel pin and in each burnable absorber region.

Figure 2-5 Calculation sequence in the CASMO Predictor-Corrector scheme

CASMO burnup step	Exposure			
	E_{n-1}	E_n	E_{n+1}	E_{n+2}
n	(ϕ_n) N_{n-1}	ϕ_n $N_n(c)$	N_n (ϕ_n) N_n	$N_{n+1}(p)$
$n + 1$		(ϕ_{n+1}) N_n	ϕ_{n+1} $N_{n+1}(c)$	N_{n+1} (ϕ_{n+1}) N_{n+1}

N = Number densities

ϕ = Fluxes

σ = Cross sections

$N_n(p)$ = Predictor number densities computed with ϕ_{n-1} and σ_{n-1}

$N_n(c)$ = Corrector number densities computed with ϕ_n and σ_n

$N_n = (N_n(c) + N_n(p))/2$

Final number densities to be used as initial NDs in step t_n to t_{n+1}

2.3.6.1 The Power Normalization Factor

The fluxes ϕ obtained from the transport calculation are normalized such that the total source in the lattice is equal to unity. Before depletion, the fluxes are re-normalized such that the average power density is equal to the input parameter BUR' , the power density in W/(g fuel) [4].

The time step Δt_n in seconds is given by

$$\Delta t_n = \frac{BU}{BUR' \sum_{i \in \text{fuel}} \rho_i V_i} \quad (2.13)$$

BU is the burnup step expressed in $W \cdot s$ (or J), computed as

$$BU = 86400 \cdot \Delta E_n \sum_i V_i \rho_i H_i \quad (2.14)$$

ρ_i is the region mass density, V_i is the region volume, and ΔE_n is the burnup step in MW-d/tU, i.e., MW-day per metric tonne initial heavy metal. The factor of 86400 converts days to seconds. The weight fraction of heavy metal in fuel region i is computed as

$$H_i = 1 - \sum_{m'} \frac{w_{i,m'}}{100} \quad (2.15)$$

$w_{i,m'}$ is the weight percent of nuclide m' in fuel region i , and the sum is taken over all nuclides which are not depleted.

The power normalization factor f_p is now determined by solving the following equation for f_p

$$BU = f_p \sum_{i \in \text{fuel}} V_i \sum_m \kappa_m \int_t^{t+\Delta t} N_{m,i}(t') dt' \sum_g \sigma_{f,m,i,g} \phi_{i,g} \quad (2.16)$$

where κ_m is the recoverable energy released per fission of actinoid nuclide m . The fluxes $\phi_{i,g}$ and cross sections $\sigma_{f,m,i,g}$ are assumed to be time independent during a burnup step, and the integral $\int_t^{t+\Delta t} N_{m,i}(t') dt'$ is obtained by integrating Eq. (2.19) over the time step. $\phi_{i,g}$ is defined by Eq. (2.20).

2.3.6.2 The Bateman Equations and CRAM Solution

Given fluxes and cross sections, time-dependent number densities can be determined by the solution of a system of first-order ordinary differential equations known as the burnup or Bateman equations.

The balance equation for nuclide m for one region is [4]

$$\begin{aligned} \frac{dN_m(t)}{dt} = & -(\lambda_m + \sigma_{a,m}\phi)N_m + \sum_{m' \neq m} \gamma_{m' \rightarrow m} \lambda_{m'} N_{m'} + \sum_{m' \neq m} \sigma_{m' \rightarrow m} \phi N_{m'} \\ & + \sum_{m'} Y_{m' \rightarrow m} \sigma_{f,m'} \phi N_{m'} \quad , \quad m = 1, \dots, M \end{aligned} \quad (2.17)$$

where

- N_m : time-dependent number density for nuclide m
- λ_m : decay constant for nuclide m
- $\sigma_{a,m}$: one-group absorption cross section for nuclide m
- ϕ : one-group flux (normalized to produce the desired power) in the region of interest
- $\gamma_{m' \rightarrow m}$: decay branching ratio from nuclide m' to m
- $\sigma_{m' \rightarrow m}$: cross section for production of nuclide m from nuclide m'
- $\sigma_{f,m'}$: fission cross section for fissionable nuclide m'
- $Y_{m' \rightarrow m}$: fission yield from fissionable nuclide m' to fission product nuclide m
- M : total number of nuclides tracked, including heavy nuclides and fission products

The first term on the right-hand side of Eq. (2.17) is the loss of nuclide m from decay and neutron absorption. The second term is the production of nuclide m by its decay precursors. The third term includes production from neutron-induced reactions. CASMO5 tracks (n, γ) , $(n, 2n)$, $(n, 3n)$, and $(n, 4n)$ reactions. (Although previous versions of CASMO inferred the $(n, 2n)$ cross section

from a negative absorption cross section in high-energy groups, CASMO5 reads and stores the (n, xn) cross sections individually.) The fourth term is the fission production of nuclide m .

There are M such equations, one for each nuclide. These equations form a system of equations which can be written in matrix notation as

$$\frac{d\vec{N}}{dt} = A \vec{N} \quad (2.18)$$

The number densities have been placed in a vector \vec{N} , and the transition rates are placed in the sparse matrix A . The diagonal entry A_{ii} is the loss coefficient of nuclide i , and A_{ij} is the production coefficient from nuclide j to i .

The Chebyshev rational approximation method (CRAM) [13] is currently the default solver used in CASMO5 for the solution to the burnup (Bateman) system of ordinary differential equations [14]. The CRAM k -order approximation of the matrix exponential in Eq. (2.18) is

$$\vec{N}(\Delta t) = \alpha_0 \vec{N}_0 + 2\Re \left[\sum_{i=1}^{k/2} \alpha_i (A \Delta t - I \theta_i)^{-1} \vec{N}_0 \right] \quad (2.19)$$

Here, the poles and residues $\{\theta_i, \alpha_i\}_{i=0}^{k/2}$ are complex and are pre-computed. The identity matrix I is the same size as A . CRAM is accurate for matrices whose eigenvalues lie near the negative real axis in the complex plane. The A matrix in the burnup equations has been observed to meet this condition in all lattice depletion cases examined [15].

2.3.6.3 Depletion Mesh

For most fuel pins, CASMO5 tracks the nuclide inventory using one spatial depletion zone per pin. For pins containing gadolinium as a burnable absorber, the code automatically subdivides the pin into concentric rings and tracks the nuclide inventory individually in each ring. The depletion zones for control rods and other burnable compositions follow the user's input.

CASMO5 also is capable of an optional azimuthal depletion calculation where the pins are further sub-divided into either four or eight sectors.

2.3.7 CASMO Edits

The editing part of CASMO provides

- Lattice and region averaged constants
- Neutron balances
- Reaction rates for individual nuclides in the fuel
- The power distribution
- Reaction rates in detectors
- Delayed neutron yields, etc.

2.3.7.1 Expansion of Fluxes

In CASMO, the group flux $\phi_{k,h}$ from the 2D transport calculation is expanded to micro-groups and micro-regions (fuel, can, coolant, etc.) using the spectra from the micro-group calculations (see Eq. (45) in Chapter 10, Ref. [6])

$$\phi_{i,g} = \phi_{k,h} V_k \frac{\phi'_{i,g}}{\sum_{i \in k} V_i \sum_{g' \in h} \phi'_{i,g'}} \quad (2.20)$$

i = micro-region
 g = micro-group
 k = macro-region containing micro-region i
 h = 2D group
 $\phi_{k,h}$ = 2D group flux in the macro-region k
 $\phi'_{i,g}$ = fluxes from the micro-group calculation

Eq. (2.20) ensures that $\phi_{i,g} \propto \phi'_{i,g}$ and that the volume-weighted sum of the expanded flux $\phi_{i,g}$ in the micro-regions $i \in k$ and groups $g' \in h$ will equal the 2D flux $\phi_{k,h}$, that is,

$$\phi_{k,h} = \frac{1}{V_k} \sum_{i \in k} V_i \sum_{g' \in h} \phi_{i,g'} \quad (2.21)$$

The fluxes defined by Eq. (2.20) are then used for the calculation of the neutron balance and reaction rates.

2.3.7.2 Cross Section and Diffusion Coefficients

Lattice and region averaged cross sections may be printed in any available group structure. Volume and flux weighting is used for condensation and homogenization. The diffusion coefficient is obtained from the transport cross section, i.e.,

$$D_g = \frac{1}{3\Sigma_{tr,g}} \quad (2.22)$$

The energy condensation of the diffusion coefficient to the few-group structure is performed by volume and flux weighting D_g .

2.3.7.3 Neutron Balance

The neutron balance may be printed for any part of the lattice. The neutron balance includes region-averaged fluxes, absorption rates, fission rates, nu-fission rates, leakages, out-scatter, in-scatter, sources, and currents (see pp. 1230-1231 in [4])

$$RIF_{l,h} = \sum_{k \in l} V_k \phi_{k,h} \quad (2.23)$$

where $\phi_{k,h}$ is the expanded macro-region, micro-group flux given by Eq. (2.20).

$$RAF_{l,h} = RIF_{l,h}/V_l \quad (2.24)$$

$$ABS_{l,h} = RIF_{l,h} \Sigma_{a,l,h} \quad (2.25)$$

$$FISS_{l,h} = RIF_{l,h} \Sigma_{f,l,h} \quad (2.26)$$

$$NUFISS_{l,h} = RIF_{l,h} \nu \Sigma_{f,l,h} \quad (2.27)$$

$$LEAK_{l,h} = RIF_{l,h} D_{cell,h} B^2 \quad (2.28)$$

$$OUTSC_{l,h} = RIF_{l,h} \sum_{h' \neq h} \Sigma_{h \rightarrow h',l} \quad (2.29)$$

$$INSC_{l,h} = \sum_{h' \neq h} RIF_{l,h'} \Sigma_{h' \rightarrow h,l} \quad (2.30)$$

$$SOURCE_{l,h} = \frac{\lambda_h}{k_{eff}} \sum_{h'} RIF_{l,h'} \nu \Sigma_{f,l,h} \quad (2.31)$$

$$INCURR_{l,h} = ABS_{l,h} + LEAK_{l,h} + OUTSC_{l,h} - INSC_{l,h} - SOURCE_{l,h} \quad (2.32)$$

k = macro region

l = any combination of macro regions

h = Edit-A (2-group), or Edit-B (8-group) edits

The flux is normalized so that $\sum_h NUFISS_{l,att,h} = 1$.

2.3.7.4 Reaction Rates and Power distribution

Fuel rod reaction rate edits are available, along with fission rate distribution, heat surface flux, maximal linear loading, and maximal heat surface flux. Fuel rod reactions for nuclide m are calculated from

$$FRR_{x,m,i,h} = V_i \sum_{g \in h} N_{m,i} \sigma_{x,m,i,g} \phi_{i,g} \quad (2.33)$$

h = Edit-A group index, e.g., 1 or 2

g = micro-group index

i = fuel region index

m = nuclide index

x = absorption, fission or capture

N = number density

V = volume

The cross sections used are those including shielding in the resonance region. $\phi_{i,g}$ is given by Eq. (2.20).

The fission rate distribution for fuel pin i is given by

$$P1_i = \sum_m \sum_h FRR_{f,m,i,h} \quad (2.34)$$

$P1_i$ is normalized so that $\sum_i P1_i = I$, where I is the total number of fuel pins in the assembly. The power caused by fissions in each fuel pin is given by

$$P2_i = \sum_m \sum_h \kappa_m FRR_{f,m,i,h} \quad (2.35)$$

$P2_i$ is normalized so that $\sum_i P2_i = I$. Note that κ is the average energy released per fission.

The heat surface flux (W/cm²) is

$$P3_i = \frac{P2_i}{2\pi r_{c,i}} \quad (2.36)$$

$P3_i$ is normalized by $\sum_i P3_i r_{c,i} = \sum_i r_{c,i}$, where $r_{c,i}$ is the outer radius of canning/clad.

Assuming that the power distribution from gamma irradiation is flat over the assembly, the gamma smeared power distribution is obtained by

$$P4_i = (1 - \gamma)P2_i + \gamma \quad (2.37)$$

where γ is the approximate fraction of the fission energy released as gamma irradiation and which escapes the fuel rod when fission occurs. It is given the approximate value 0.095 in CASMO5, which is obtained by comparing power distributions from energy deposition calculations using explicit gamma transport calculations to those obtained from Eq. (2.37)

$P4_i$ is normalized so that $\sum_i P4_i = I$.

2.3.7.5 Detector Edits

Detector reaction rates are determined by

$$RR_{x,m,j} = \sum_g \phi_{j,g} \sigma_{x,m,g} \quad (2.38)$$

Here x denotes absorption or fission.

$RR_{x,m,j}$ may be obtained for any nuclide for which there is data in the library. The cross sections corresponding to the reaction rates are also calculated as

$$\sigma_{x,m,j,h} = \frac{\sum_{g \in h} \phi_{j,g} \sigma_{x,m,g}}{\sum_{g \in h} \phi_{j,g}} \quad (2.39)$$

The reaction rate in a PRM detector sensitive to fissions or absorptions in a specified region and for a specified nuclide is calculated as

$$RR = \sum_g \phi_g \sigma_{x,m,g} \quad (2.40)$$

where ϕ_g is the flux in the detector region defined by input. The reaction rate is normalized to the average power in the assembly.

The flux ratio center-to-lattice is defined by

$$FR_h = \frac{\phi_{c,h}}{\phi_{latt,h}} \quad (2.41)$$

where c is the innermost region of the center pin cell and $latt$ refers to the assembly plus gaps (CASMO segment) average flux. h denotes the Edit-A energy group.

The U-235 fission cross section at the center is determined by

$$\sigma_{center,h}^{235} = \frac{\sum_{g \in h} \sigma_{f,g}^{235} \phi_{c,g}}{\sum_{g \in h} \phi_{c,g}} \quad (2.42)$$

The rhodium detector Y factors are calculated for an Rh detector located in the innermost region of the center pin cell.

2.3.7.6 Kinetic Data

The effective delayed neutron yield for the standard six delayed-group precursors is computed in CASMO5 by using a spatially-averaged flux and adjoint spectrum weighted formulation. The basic delayed neutron data for relevant heavy nuclides is based on the Tuttle data set [108]. The mean neutron generation time is also edited by CASMO based on the flux and adjoint spectra.

The delayed neutron yields are given by

$$\bar{\beta}_l = \sum_m \beta_{m,l} \sum_g \frac{NUFISS_{m,g}}{NUFISS} \quad (2.43)$$

and the corresponding decay constants are

$$\lambda_l = \frac{\sum_m \lambda_{m,l} \beta_{m,l} \sum_g NUFISS_{m,g}}{\bar{\beta}_l \times NUFISS} \quad (2.44)$$

where

$$NUFISS_{m,g} = \sum_i \nu \sigma_{f,i,m,g} V_i \phi_{i,g} N_{i,m} \quad (2.45)$$

$$NUFISS_m = \sum_g NUFISS_{m,g} \quad (2.46)$$

$$NUFISS = \sum_m \sum_g NUFISS_{m,g} = 1 \quad (2.47)$$

l = delayed neutron group

m = fissionable nuclide

β_m = total fraction of delayed neutrons from nuclide m

$\beta_{m,l} = \beta_m a_{m,l}$

$a_{m,l}$ = the fraction of delayed neutrons from nuclide m related to delayed neutron group l

$\lambda_{m,l}$ = the decay constant for delayed neutron group l after fission in nuclide m

The average energy of the delayed fission spectrum is lower than that of the prompt fission spectrum. Therefore, the delayed neutrons have a smaller chance to leak out of (or into) the system, and they do not cause fast fission. The effective delayed neutron yield is defined as (see p. 302 in [17])

$$\beta_{eff,l} = \frac{\sum_m (\sum_h \phi_h^* \chi_{l,h}) \beta_{m,l} NUFISS_m}{\sum_m [(1 - \sum_l \beta_{m,l}) (\sum_h \phi_h^* \chi_h) + \sum_l \beta_{m,l} (\sum_h \phi_h^* \chi_{l,h})] NUFISS_m} \quad (2.48)$$

where

- m = fissile nuclide
- ϕ_h^* = adjoint lattice-average flux for micro-group h
- $\chi_{l,h}$ = neutron spectra for delayed group l
- $\beta_{m,l}$ = neutron fraction for delayed group l
- χ_h = prompt fission spectra

The adjoint flux ϕ_h^* is calculated by default from the adjoint fundamental mode equation (see Eq. (609) in [4]). Alternatively, a two-dimensional adjoint option is available in CASMO5 which uses the transport-equivalent Coarse Mesh Finite Difference (CMFD) data to solve the two-dimensional adjoint diffusion equation over the acceleration mesh. While the adjoint spectrum is sufficiently accurate for single segment cases, using the two-dimensional adjoint option is highly recommended for cases involving multiple segments with reflectors.

The lattice average values of the inverse neutron velocity are calculated by three different collapsing schemes, which involve weighting the inverse velocity using the adjoint spectrum, and flux spectrum, or both.

The adjoint spectrum is also used to compute the mean neutron generation time Λ (see p. 306 in [17]). The prompt neutron lifetime is given by $\Lambda \times k_\infty$.

2.3.7.7 Xenon and Samarium Data

If the equilibrium xenon calculation is turned on, then the xenon number densities obtained from the burnup calculation are replaced by equilibrium xenon number densities.

2.3.7.8 Flux Discontinuity Factors

Flux discontinuity factors [18][19] are calculated for each side of the assembly (segment) using the “infinite” lattice spectrum, i.e., the spectrum without correction for the fundamental mode leakage (off by default in CASMO5). Discontinuity factors are also calculated for baffle/reflector regions when modeled through input by the user.

The discontinuity factors calculated by CASMO are defined such that the net currents on an interface calculated by multigroup transport theory in CASMO are preserved in the neutronics calculation in SIMULATE [20].

In single assembly calculations, net currents on the boundary are zero and the flux discontinuity factors are determined by the ratio between the surface and average fluxes.

2.3.8 Baffle/Reflector Calculations

Traditionally, nodal codes have ignored direct treatment of the PWR baffle and reflector and have, instead, relied on user-adjusted albedos to treat the neutron reflection at the fuel/baffle interface. The primary reason is that traditional nodal models have been essentially one-group in nature,

and the complicated group coupling in the reflector region is inaccurately treated with direct reflector modeling.

Advanced nodal models do properly model the complicated group coupling, and they are capable of treating the baffle/reflector regions directly. The baffle is typically a stainless steel plate with an approximate thickness of 2-4 cm, depending on the reactor manufacturer. Direct treatment of the baffle requires that the nodal mesh accommodate small baffle regions, and the number of mesh points in the nodal problem nearly quadruples. Therefore, nodal models usually employ a uniform radial mesh which requires that the baffle be homogenized with the surrounding water reflector. The drastic differences between the neutronic properties of the baffle and reflector make proper determination of homogenized constants difficult. In fact, attempts at adjusting two-group cross sections for use in homogenized baffle/reflector regions are usually no more satisfactory than the adjustment of albedos in conventional nodal models.

In Studsvik CMS, the baffle/reflector problem is treated directly in CASMO. The reflector option allows specification of the thickness and composition of the baffle and radial reflector. CASMO performs a multi-group neutron transport calculation for a fuel assembly with baffle and reflector regions adjoining one edge of the assembly. A black boundary condition is imposed on the reflector edge facing away from the fuel assembly. This solution provides a high-order approximation to the flux and leakage distribution at the fuel/baffle interface as well as reaction rates in the baffle and reflector.

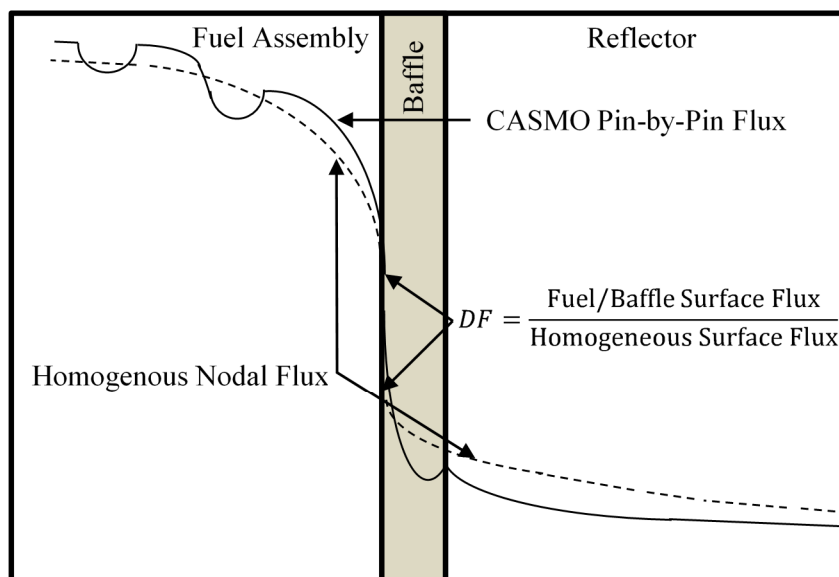
Discontinuity factors for the homogenized baffle/reflector region are computed by calculating the homogeneous flux distribution in the reflector, using the same basis function that will be used in SIMULATE.

The cross sections required in the reflector region are flux-volume weighted over the baffle/reflector region, and the required boundary conditions are taken from the CASMO solution. Discontinuity factors for the homogenized baffle/reflector region are defined by the respective ratios of heterogeneous and homogeneous surface fluxes, as depicted in Figure 2-6. This figure shows that the drastic fast flux depression in the baffle does not occur in the homogenized model. Therefore, the fast-group discontinuity factor required to preserve the leakage and reaction rates must be greater than one, and typical values are 1.25 to 1.30. In the thermal group, the situation is reversed. The baffle is a large absorber of thermal neutrons; and this produces a localized thermal flux depression which the homogenized model cannot predict, resulting in the thermal discontinuity factors with typical values in the range of 0.20 to 0.35. These discontinuity factors preserve the group-wise core leakage and the reflector absorption.

CASMO typically calculates cross sections and discontinuity factors for a pure water reflector or for a steel baffle surrounded by water when reflector is modeled through input. (Of course, reflector data can be generated for other materials as well.)

The reflector calculation generates net currents, surface fluxes, and region-average fluxes in the 2D energy group structure. The cross sections, discontinuity factors, currents, surface and average fluxes are printed to the card image file. SIMULATE uses the cross sections and discontinuity factors for the homogenized baffle/reflector.

Figure 2-6 CASMO5 Reflector/Baffle model



2.3.9 Submesh Data

In order to generate submesh data for SIMULATE5, an assembly is divided into $N \times N$ "sub-meshes" (typically $N=5$), where the rectangular sub-meshes follow pin cell boundaries [21]. For PWRs, the outer layer is chosen to be one pin cell layer thick in order to capture intra-assembly mismatch effects (build-up of plutonium etc.). All reflector regions outside the active core are treated in an analogous manner. In addition, PWR baffles are represented explicitly.

Sub-mesh cross sections and discontinuity factors are generated by CASMO5 together with the assembly average data. The sub-mesh data is generated in a manner consistent with the generation of the assembly-averaged nodal data.

Although a sub-mesh, consisting of a number of pin cells or of a section of the water gap including any control rod, is not materially uniform, it is considerably less heterogeneous than the full assembly itself. The sub-mesh cross sections and discontinuity factors are therefore less dependent on the CASMO5 boundary conditions (the zero net current assumption) than the full assembly counterparts.

2.3.10 Gamma Transport

After the neutron transport calculation is finished, gamma sources from neutron capture, fission, and inelastic scattering can be calculated for all regions of the problem, and a characteristics-based gamma transport calculation performed using the same two-dimensional model that is used for the neutron transport calculation.

The CASMO5 gamma library is an 18 gamma energy group library based on ENDF/B-VII.0 data. The photo-atomic library is unchanged between ENDF/B-VII.0 and ENDF/B-VII.1. The gamma production matrices are tabulated in 70 groups.

The gamma transport calculation is done directly in the energy group structure of the gamma library. The calculation can be performed either separately for prompt and for delayed gamma sources, or using the combined total gamma source. Gamma fluxes are calculated for all regions of the assembly, but only fluxes in the detector location and the gamma detector response are normally edited.

The gamma cross sections are temperature independent; all data are evaluated at 296 K.

2.3.10.1 Detector Responses

After the gamma sources and cross sections have been determined for all regions, the program enters the 2D transport module to carry out the two-dimensional gamma transport calculation. At this point, the gamma sources have already been determined, and the 2D transport module therefore performs a fixed source calculation, which is done either separately for prompt and delayed sources or using the total source, depending on which option the user has chosen via input.

2.3.10.2 Energy Deposition

CASMO has the capability to calculate the energy deposited in any micro-region from the slowing down and absorption of neutrons and from gamma absorption.

2.3.11 Multi-assembly Capability

In the multi-assembly calculation each assembly may have its own individual design and rotation. Control rods may be inserted in any location and each assembly may be modeled at separate conditions (e.g., fuel temperature, void fraction, etc.). In addition, the multi-assembly calculation provides for the easy modeling of empty locations, which are filled with material moderator (typically unvoided water). The Method of Characteristics (MoC) is used to solve for the 2D flux distribution for the entire problem. Furthermore, the full depletion capability of single assembly calculations is available in multi-assembly geometries as well as gamma calculations.

Each segment is processed on an individual basis until the 2D MoC transport module is reached, at which time the complete problem geometry is constructed. Following the 2D calculation, the segments are de-coupled and once again treated on an individual basis for edits and burnup.

More specifically, pin cell calculations (i.e., the micro-group calculation) are performed on an individual segment basis. Following the pin cell calculations, the cross sections are condensed to the 2D group structure, and the 2D MoC transport calculation is performed on the entire multi-segment problem. It is at this point that the segments are rotated into their proper orientation and placed into the appropriate location. The 2D transport calculation is then performed with the same detail as is used in single segment applications. Also, by default the fundamental mode calculation is skipped. If a gamma calculation has been requested then it is performed at this point before taking any burnup steps.

2.3.12 Fuel Storage Rack Capability

The CASMO5 fuel storage rack model allows up to 100 slabs of arbitrary thickness on each side of the segment, each of which may be subdivided into up to 10 arbitrary lengths and unique compositions. The model is implemented through two CASMO5 input models: the FSS (Fuel Storage Side) and the FSC (Fuel Storage Corner).

The FSS input describes a single “side” of the rack in terms of slabs of various thicknesses, lengths and compositions. These lengths must all sum to the width of the segment (out to, and including, the outer gaps). By projecting the slab dimensions into a corner, the discretization of the corner regions is automatically defined by the intersection of the slabs. The user then simply uses the FSC input to specify the compositions of these corner regions.

Racks are frequently symmetric. Therefore, the input allows the same FSS/FSC cards to be used for all four sides. However, by providing multiple FSS/FSC inputs, each side and corner is allowed to be unique.

The FSS/FSC fuel storage rack model is intended to produce a high-fidelity transport solution. The calculation is performed in 95 energy groups, which helps model leakage at high energies. Thermal expansion is off, and the fundamental mode calculation is omitted.

The FSS/FSC model is supported for multi-assembly applications. The FSC/FSS model is only supported in full geometry.

3 CASMO5 VALIDATION

The validation of CASMO5 was performed to demonstrate the code can predict reactivity, burnup (i.e. isotopics), and reaction rates for typical PWR assembly configurations.

The validation consists of two methods: the comparison to physical measurements and the comparison to higher order computer codes (i.e. MCNP). While the use of physical measurements for comparison is always the ultimate goal of validation, the cost and difficulty in obtaining the measurements limits the range of conditions available. The use of higher order code calculations and computational benchmarks allows one to study the mechanics of the codes and help to ensure proper method implementation over the full range of conditions.

The validation shows that CASMO5 is suitable for modeling all PWR fuels with the following attributes:

- Pin lattice geometries ranging from 14x14 to 17x17 including both large and small water hole designs.
- Integral burnable absorbers types Gadolinia (Gd_2O_3) and IFBA (ZrB_2).
- Discrete absorber types: WABA, B_4C - AlO_3 , Boron Silicate Glass and Hafnium Suppression Rods.
- Control Rod absorber types: B_4C , Ag-In-Cd, W and Hafnium.
- Low enriched Uranium Oxide (UO_2) fuel.
- Soluble Boron in the coolant.
- In-Core Detector types of movable fission chambers and fixed designs.

3.1 Method of Analysis

During the validation process, the results of CASMO5 calculation are compared to either experimental measurements or higher order code calculations. This section will present the methods used to compare the results.

3.1.1 Differences

In the validation calculations two types of differences are used.

Reaction rates are compared by determining an absolute difference scaled by 100 to express it in percent. This is deemed the most appropriate form of difference for reaction rates due to the fact they are already normalized to a relative basis. The form is shown in equation 3.1. The reference quantity is an experimental measurement or higher order code calculation result.

$$\text{Percent Absolute Error} = (\text{CASMO5} - \text{Reference}) * 100 \quad (3.1)$$

Isotopic quantities are compared by determining a relative difference expressed in percent. This is deemed appropriate for quantities that are not presented on a relative or normalized basis. The

form is shown in equation 3.2. The reference quantity is that taken from an experimental measurement or higher order code calculation result.

$$\text{Percent Relative Error} = \frac{(\text{CASMO5} - \text{Reference})}{\text{Reference}} * 100 \quad (3.2)$$

3.1.2 Average

The average as discussed in this report is the arithmetic mean as shown in equation 3.3.

$$\text{Average} = \frac{1}{N} \sum_{i=1}^N a_i \quad (3.3)$$

Where a_i is a calculated value or a relative difference.

3.1.3 Root Mean Square Error (RMSE)

The RMSE is used in this report to quantify how well CASMO5 predicts a distribution of data as compared to experimental measurements or higher order code calculations. Here the root mean square of the relative differences is used as shown in equation 3.4. The resulting RMSE value is sometimes scaled by 100 to express it in percent.

$$\text{RMSE} = \sqrt{\frac{1}{N} \sum_{i=1}^N (\text{CASMO5}_i - \text{Reference}_i)^2} \quad (3.4)$$

3.1.4 Standard Deviation

The standard deviation is used to measure the spread of the data from the mean. The sample standard deviation is used in this report, often called the 'n-1' method.

$$\text{St. Dev. Sample} = \sqrt{\frac{1}{N-1} \sum_{i=1}^N (X_i - \bar{X})^2} \quad (3.5)$$

Where \bar{X} is the average of the quantity in the set as described by equation 3.3.

When calculating the standard deviation of eigenvalues, the result is scaled by 10^5 to express results in percent milli.

3.1.5 Mean Relative Pin Power Error

The C5G7 MOX benchmark described in Reference 38 and discussed in section 3.3.1 has specific quantities that are used to compare to the benchmark results. The only unique quantity not previously defined is the MRE. It is defined below in equation 3.6.

$$MRE = \frac{\sum_N |e_n| * p_n}{N * p_{avg}} \quad (3.6)$$

Where e_n is the percent relative error of the pin power as defined in equation 3.2, p_n is the relative pin power at location n , and p_{avg} is the average pin power as described in equation 3.3 for all fueled pins.

3.2 Measurement Comparisons

There are two categories of measurement comparisons that are presented. The first category is critical experiments, and second is measured depleted fuel isotopic compositions from post irradiation examinations.

3.2.1 Critical Experiments

The list of experimental configurations modeled in this validation report is not meant to be exhaustive. They have been chosen to demonstrate the range of attributes discussed at the beginning of Section 3.

3.2.1.1 B&W 1810

The Babcock & Wilcox 1810 critical experiments described in Reference 22 were designed to represent realistic reactor configurations. The experiments consisted of a ~5x5 array of either PWR 15x15 type assemblies (i.e., Westinghouse or Babcox & Wilcox designs) or PWR 16x16 type assemblies (i.e., Combustion Engineering design). The central “assembly” was modified from one experiment to the next. Some cores contained gadolinium fuel pins, Ag-In-Cd (AIC), or B₄C control rods, or hollow rods. All core configurations from this set were analyzed in Reference 32, with the exception of Core 11, which was specifically designed to measure resonance parameters.

The geometry of Cores 1 through 17 represents a Babcock & Wilcox, Westinghouse, KWU, etc. type of reactor design (see Figure 3-1). The core consists of a 5x5 array of pseudo-assemblies (individual pins without spacers), each containing a 15x15 pin array. Cores 1 through 10 consisted of a uniform fuel enrichment distribution. Cores 12 through 17 consisted of a high enrichment central area surrounded by a low enriched zone. From one core to the next, the central pseudo-assembly was modified with gadolinium fuel pins, Ag-In-Cd or B₄C control rods or hollow tubes.

The geometry of Cores 18 through 20 represents a Combustion Engineering type of reactor design (see Figure 3-2). The core consists of a 5x5 array of pseudo-assemblies, each containing a 16x16 pin array. All cores contain a high enrichment central area surrounded by a low enriched zone. The cores differ only in the number of gadolinium fuel pins present.

All measurements are reported at a facility temperature of 25°C (77°F).

The calculated CASMO5 eigenvalues are shown in Table 3-1 and agree well with the experiment. The comparison of the measured to calculated fission rate is summarized in Table 3-2 and compare well with measurement with errors typically less than 1%.

The BAW-1810 results demonstrate that CASMO5 can adequately model both large and small water hole assembly designs, which include the presence of Gadolinia integral burnable absorber, B4C and AIC control rods as well as fixed Rhodium detectors.

Figure 3-1: B&W 1810 Core 3 Geometry

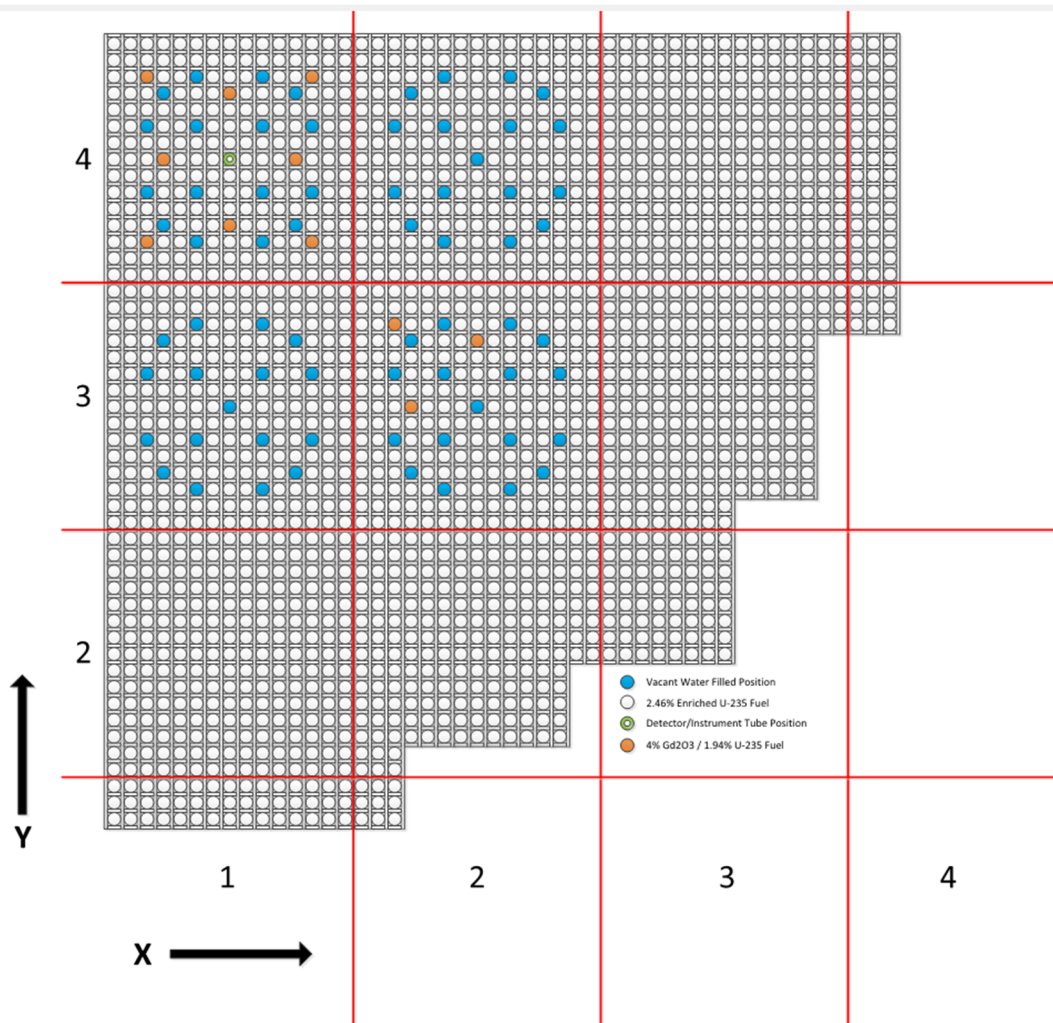


Figure 3-2: B&W 1810 Core 18 Geometry

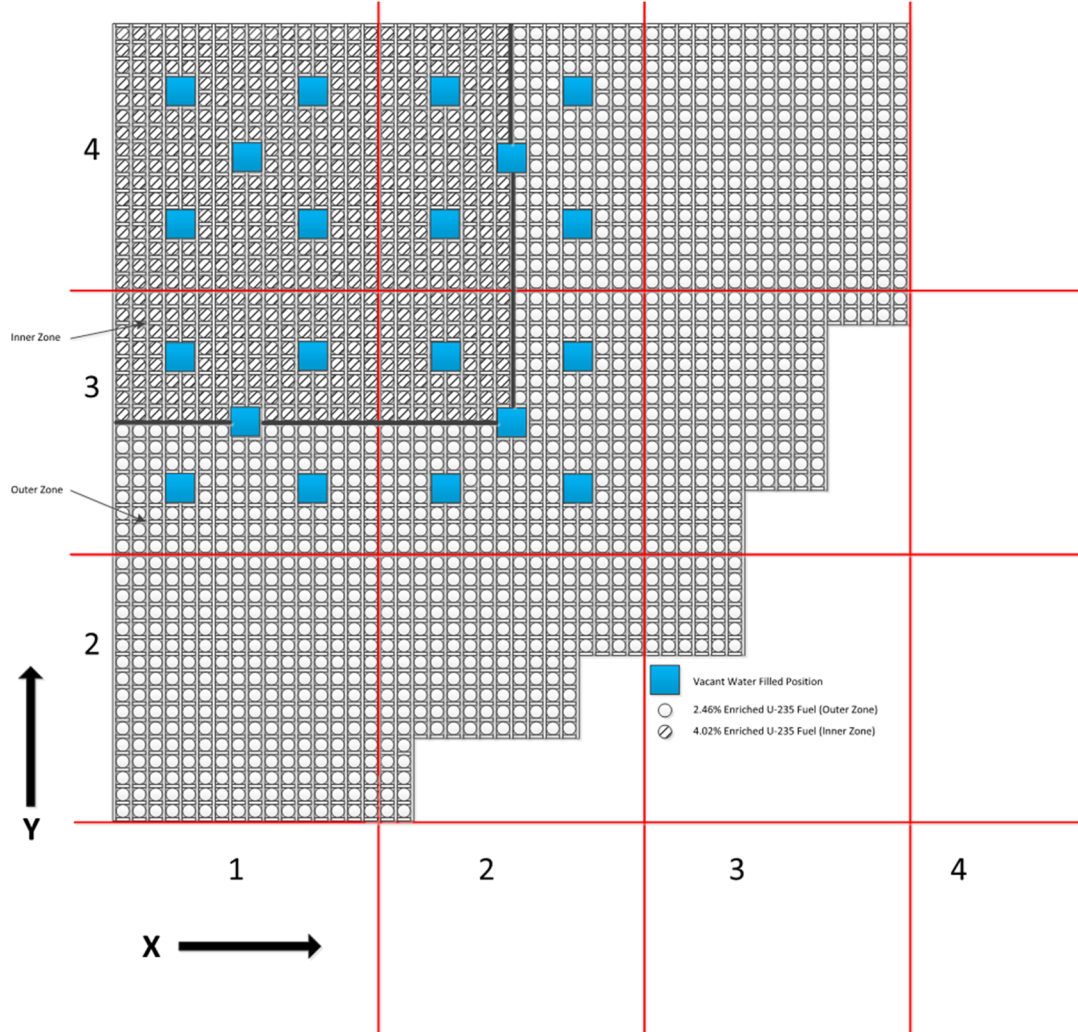


Table 3-1: B&W 1810 CASMO5 Eigenvalue Results

Core	Boron (ppm)	Lattice Design	Central Region	4% Gd Fuel (# Pins)	Ag-In-Cd (# Rods)	B ₄ C (# Rods)	K _{eff}
Core 1	1337.9	15x15	Uniform	0	0	0	{ }
Core 2	1250.0	15x15	Uniform	0	16	0	{ }
Core 3	1239.3	15x15	Uniform	20	0	0	{ }
Core 4	1171.7	15x15	Uniform	20	16	0	{ }
Core 5	1208.0	15x15	Uniform	28	0	0	{ }
Core 5a	1191.3	15x15	Uniform	32	0	0	{ }
Core 5b	1207.1	15x15	Uniform	28	0	0	{ }
Core 6	1155.8	15x15	Uniform	28	16	0	{ }
Core 6a	1135.6	15x15	Uniform	32	16	0	{ }
Core 7	1208.8	15x15	Uniform	28 (Annular)	0	0	{ }
Core 8	1170.7	15x15	Uniform	36	0	0	{ }
Core 9	1130.5	15x15	Uniform	36	16	0	{ }
Core 10	1177.1	15x15	Uniform	36	0	0	{ }
Core 11	<i>Not Analyzed</i>						
Core 12	1899.3	15x15	Two-Region	0	0	0	{ }
Core 13	1635.4	15x15	Two-Region	0	0	16	{ }
Core 14	1653.8	15x15	Two-Region	28	0	0	{ }
Core 15	1479.7	15x15	Two-Region	28	0	16	{ }
Core 16	1579.4	15x15	Two-Region	36	0	0	{ }
Core 17	1432.1	15x15	Two-Region	36	0	16	{ }
Core 18	1776.8	16x16	Two-Region	0	0	0	{ }
Core 19	1628.3	16x16	Two-Region	16	0	0	{ }
Core 20	1499.0	16x16	Two-Region	32	0	0	{ }
AVERAGE							{ }
STANDARD DEVIATION							{ } pcm

Table 3-2: B&W 1810 CASMO5 Fission Rate Results

Core	Lattice Design	Central Region	4% Gd Fuel (# Pins)	Ag-In-Cd (# Rods)	B ₄ C (# Rods)	K-EFF	Central Assembly Fission Rate RMS Error
Core 1	15x15	Uniform	0	0	0	{ }	{ }
Core 5	15x15	Uniform	28	0	0	{ }	{ }
Core 12	15x15	Two-Region	0	0	0	{ }	{ }
Core 14	15x15	Two-Region	28	0	0	{ }	{ }
Core 18	16x16	Two-Region	0	0	0	{ }	{ }
Core 20	16x16	Two-Region	32	0	0	{ }	{ }

Table 3-3: B&W 1810 CASMO5 Fission Rate Summary Results

Core Type	Value	Number of Measured Points
All Cores		
Average Absolute Error	{ }	192
Absolute Error Standard Deviation	{ }	
Small Water Hole, 15x15		
Average Absolute Error	{ }	128
Absolute Error Standard Deviation	{ }	
Large Water Hole, 16x16		
Average Absolute Error	{ }	64
Absolute Error Standard Deviation	{ }	

Figure 3-3: B&W 1810 Core 1 Central Assembly Fission Rate Comparison

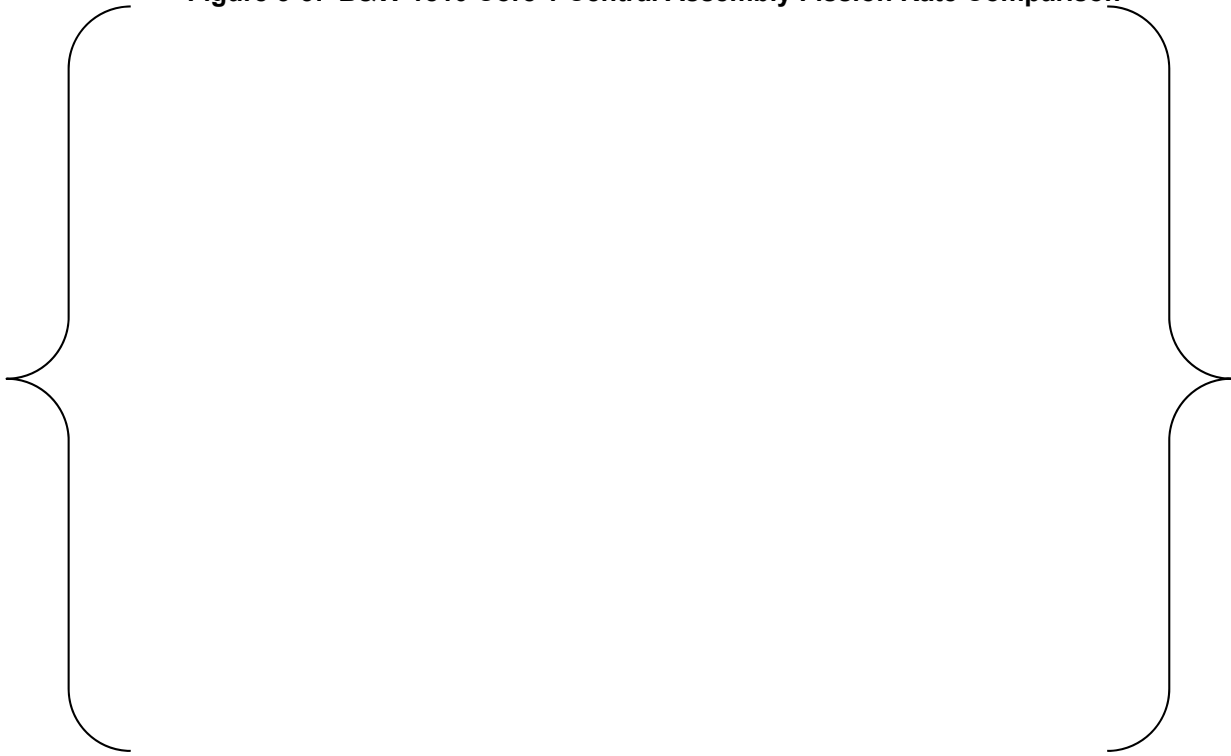


Figure 3-4: B&W 1810 Core 5 Central Assembly Fission Rate Comparison



Figure 3-5: B&W 1810 Core 12 Central Assembly Fission Rate Comparison

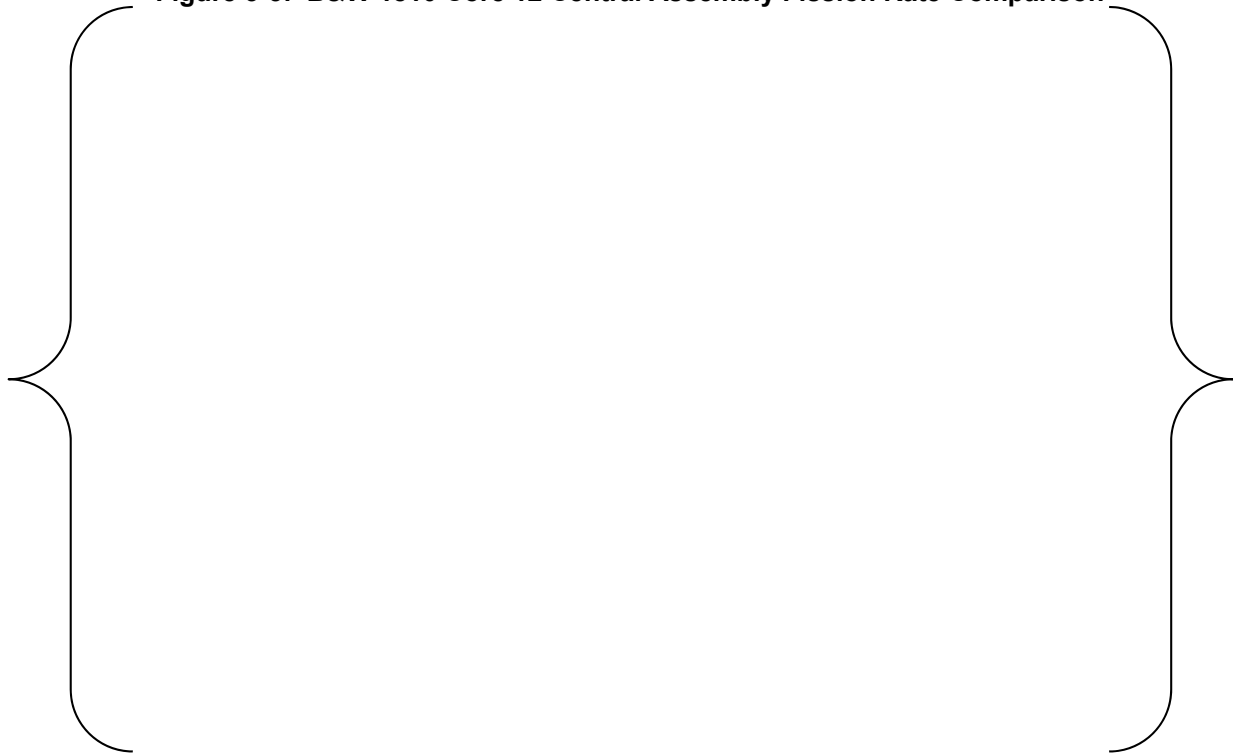


Figure 3-6: B&W 1810 Core 14 Central Assembly Fission Rate Comparison

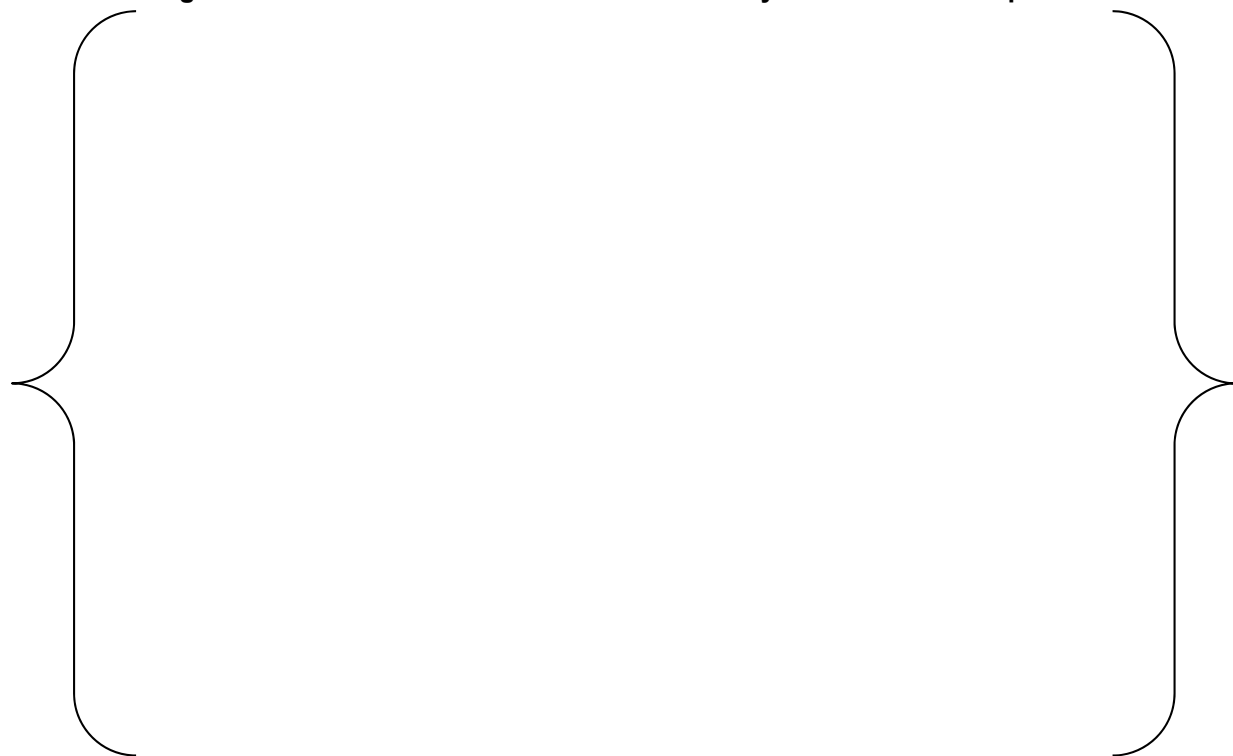


Figure 3-7: B&W 1810 Core 18 Central Assembly Fission Rate Comparison

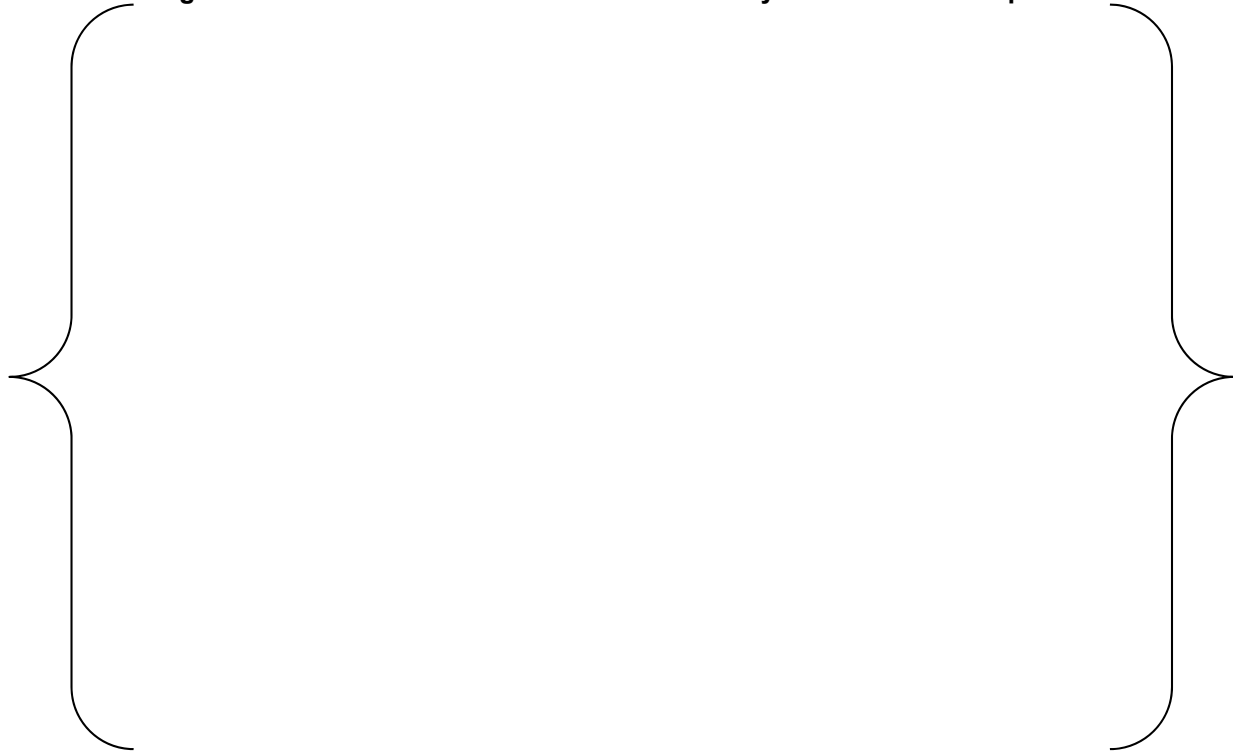
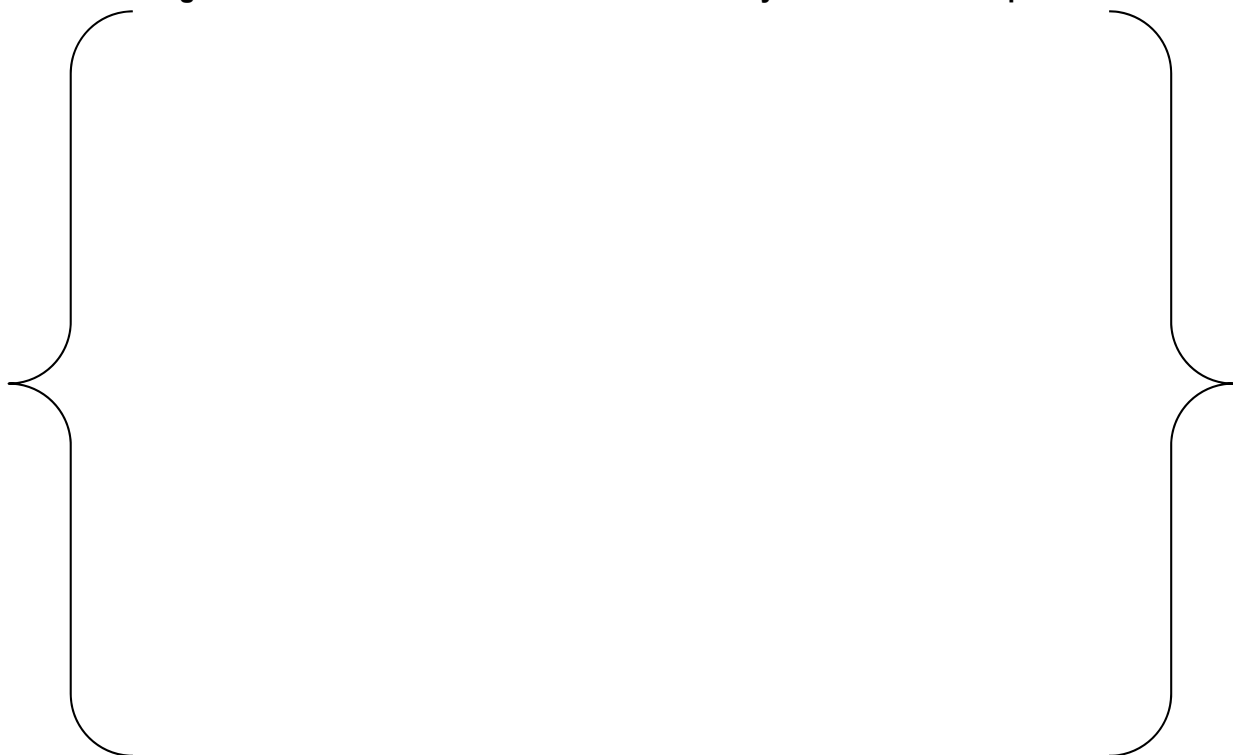


Figure 3-8: B&W 1810 Core 20 Central Assembly Fission Rate Comparison



3.2.1.2 B&W 1484

The Babcock & Wilcox (B&W) series 1484 (Reference 23) critical experiments consist of twenty-one different geometric configurations (or cores). This experiment was analyzed in Reference 33 to demonstrate that the CASMO5 transport code can accurately model pseudo core configurations that range from low to high leakage. It will also demonstrate the ability of the CASMO5 transport code to model simulated PWR fuel storage configurations.

Cores I (Figure 3-9) and II (Figure 3-10) contain no heterogeneities (e.g., water holes, absorber rods, enrichment splits) but since the cores differ in size and shape, they present a wide range of radial leakage. Core I consists of 458 identical fuel pins (2.459 wt% ^{235}U) arranged in a circular shape. The axial leakage represents 2% of the total reactivity of the core; however, the radial leakage represents nearly 35%, so this core is a very high leakage core. Core II consists of 1764 identical fuel pins (2.459 wt% ^{235}U) arranged in a square shape. The axial leakage represents 2% of the total reactivity of the core and the radial leakage represents roughly 15%, so this core is a relatively low leakage core.

Cores III through IX represent simplified potential fuel storage configurations where 15x15 pseudo-assembly (individual pins without spacers, i.e. non-unit cell) configurations are arranged in 3x3 spaced lattice configurations. The spacing between the assemblies and the configuration of absorber pins in the space are varied. The geometry of Core V is shown in Figure 3-11 as an example.

Cores X through XXI represent simplified fuel storage configurations where 15x15 fuel assembly configurations (arranged in unit cells that are movable) are arranged in 3x3 spaced lattice configurations. The presence and composition of isolating/absorbing plates between the fuel assemblies are varied. The geometry of Core XII is shown in Figure 3-12 as an example.

The calculated CASMO5 eigenvalues for Cores 1 through IX (non-unit cell configurations) are shown in Table 3-4. The results agree very well with the experiment.

The calculated CASMO5 eigenvalues for Cores X through XXI (unit cell configurations) are shown in Table 3-5. The results here show more variation. A good portion of the variation can be attributed to some experimental uncertainty in the concentration of boron in the borated aluminum sheets that are present in Cores XIII through XXI.

The experimental report (Reference 23) shows uncertainties of the boron content ranging from 1% to 4%. The model results are very sensitive to the boron content as the sheets have a large surface area in the experiment. To further understand the effect of the boron uncertainty, a configuration of each boron plate type was modeled to examine the sensitivity to boron content. Six configurations were run reducing the boron content to the 95% confidence interval, where we assume the quoted uncertainty is 1.0σ within a normal distribution (95% confidence interval $=1.96\sigma$). The results of these calculations are shown in the black triangles of Figure 3-13. From the comparison, we can see that reducing the boron content does increase the eigenvalue as intended and the spread of the data is also reduced. Without more information from the experiment it is difficult to form any solid conclusions. What we can conjecture is that the uncertainty of the boron content in the boron plates is significant. This can be supported by the work that B&W did in Reference 23 to adjust the vendor supplied plate data.

The results of the comparisons show that CASMO5 can effectively model low and high leakage configurations and various storage configurations.

Figure 3-9: B&W 1484 Core I Geometry

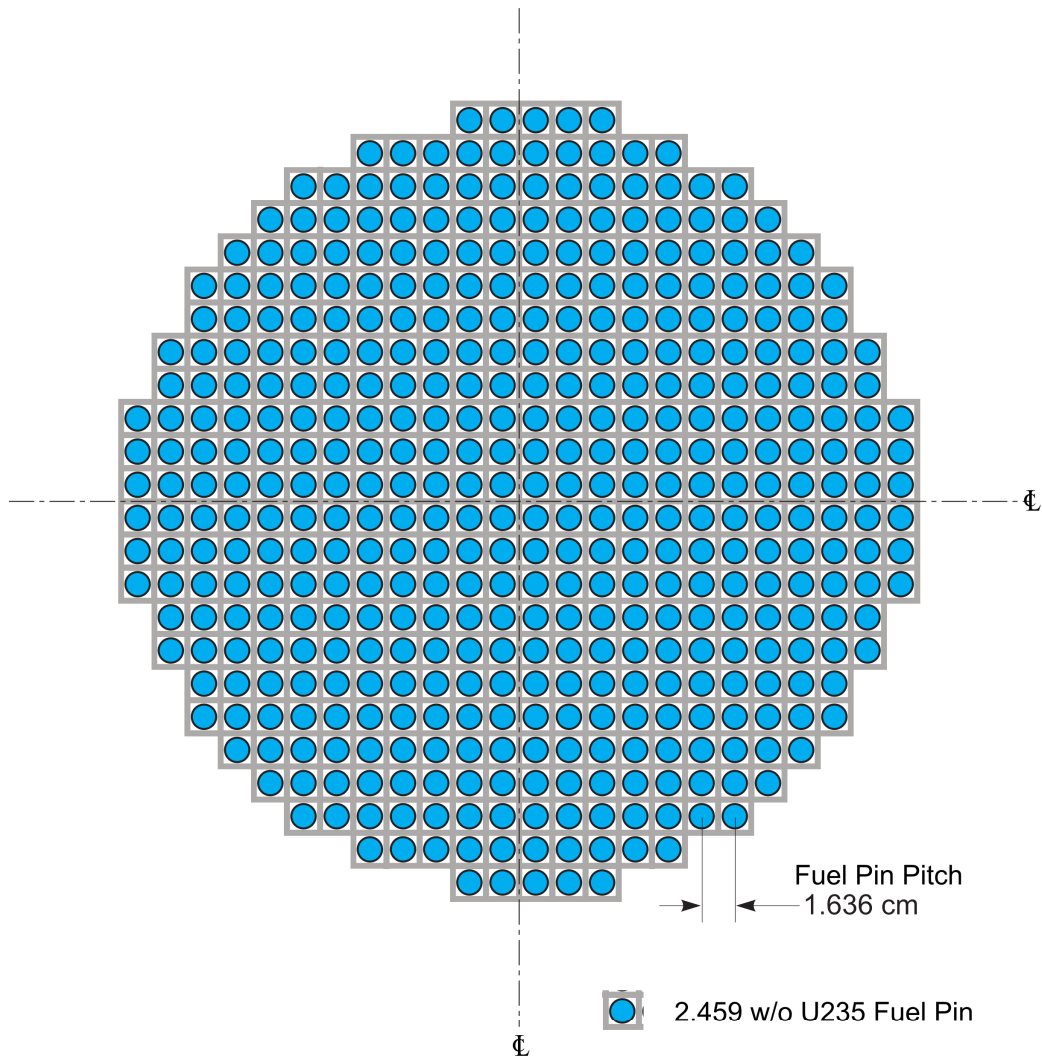


Figure 3-10: B&W 1484 Core II Geometry

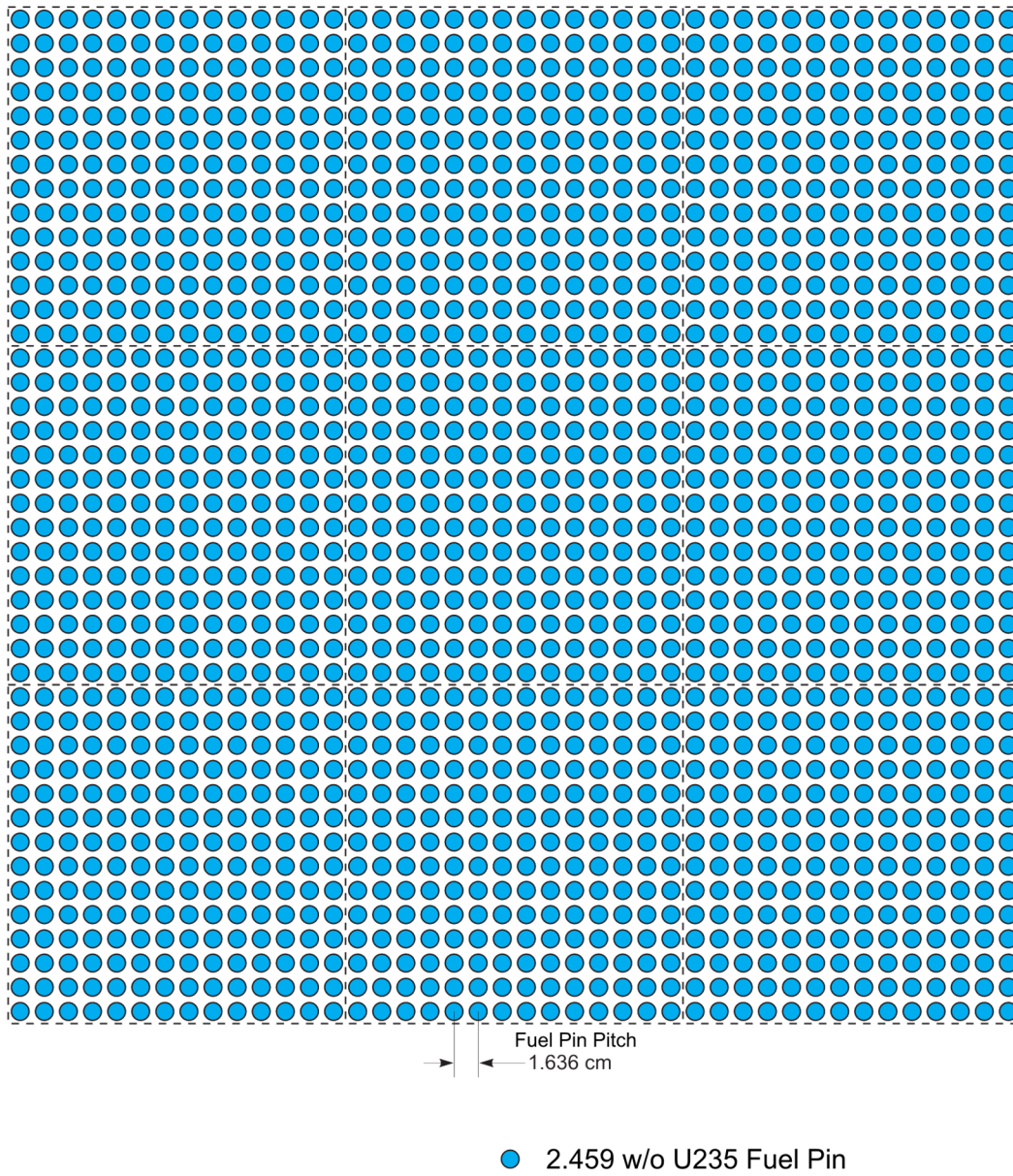


Figure 3-11: B&W 1484 Core V Geometry

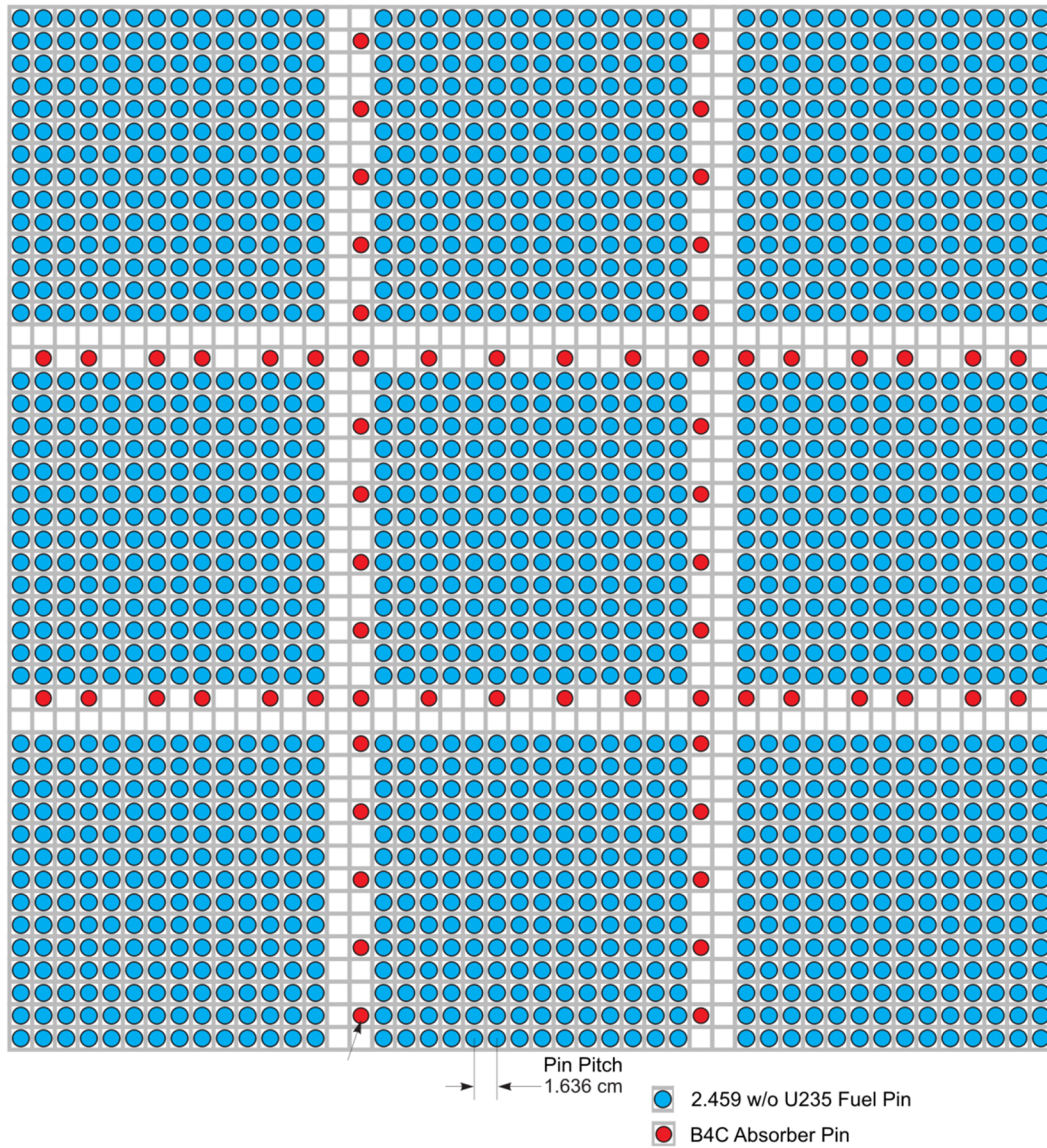


Figure 3-12: B&W 1484 Core XII Geometry

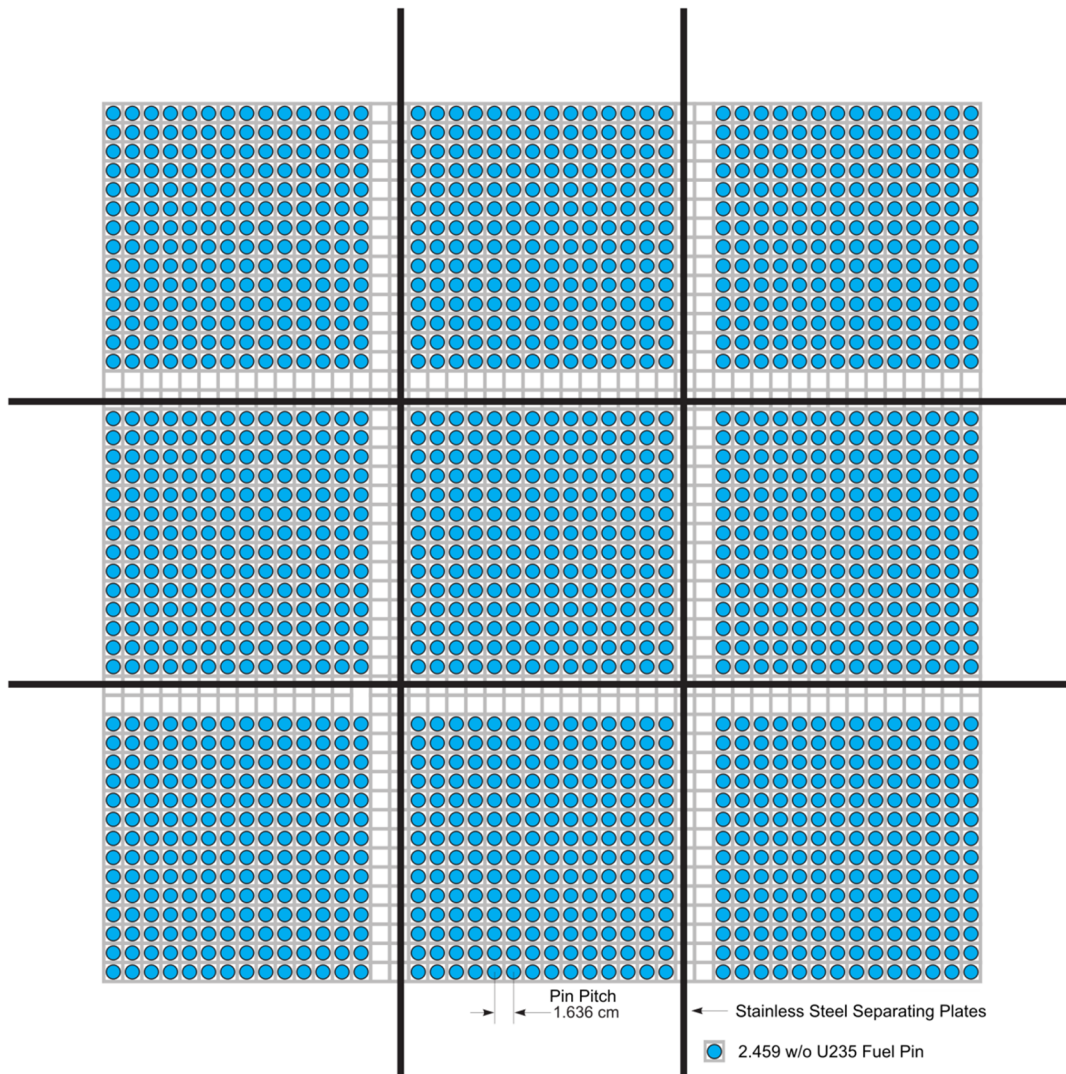


Table 3-4: B&W 1484 CASMO5 Eigenvalue Results for Non-Unit Cell Configurations

Configuration	CASMO5 K_{effective}
I	{ }
II	{ }
IIIa	{ }
IIIb	{ }
IIIc	{ }
IIId	{ }
IIIe	{ }
IIIf	{ }
IIIg	{ }
IV	{ }
V	{ }
VI	{ }
VII	{ }
VIII	{ }
IX	{ }
Average	{ }
Standard Dev.	{ } pcm

Table 3-5: B&W 1484 CASMO5 Eigenvalue Results for Unit Cell Configurations

Configuration	CASMO5 K_{effective}
X	{ }
XIa	{ }
XIb	{ }
XIc	{ }
XId	{ }
XIe	{ }
XIf	{ }
XIg	{ }
XII	{ }
XIII	{ }
XIIIa	{ }
XIV	{ }
XV	{ }
XVI	{ }
XVII	{ }
XVIII	{ }
XIX	{ }
XX	{ }
XXI	{ }
Average	{ }
Standard Dev.	{ } pcm

Figure 3-13: B&W 1484 CASMO5 Eigenvalue vs. Critical Height

3.2.1.3 KRITZ-3

The KRITZ-3 high temperature critical experiment described in Reference 25, were performed under contract between Kraftwerk Union Aktiengesellschaft Mülheim West Germany (KWU) and AB Atomenergi Studsvik Sweden.

The critical experiments are fairly unique in that they are not just at cold (i.e. room temperature) conditions. The temperature range is from { } to { }, while the range does not cover all operational conditions of a PWR it shows the ability of CASMO5 to predict reactivity as function of varying operational conditions.

The experimental geometry is a cylindrical core loaded with three different fuel pins, Uranium fuel enriched to { } w/o ^{235}U and mixed oxide fuel with a Plutonium fissile content of { } and { } w/o respectively. The Plutonium fuel pins, when present in the core, were loaded in the central zone. Eight different core configurations have been analyzed with different critical conditions such as variation in; boron concentration, moderator temperature, water level/neutron leakage (axial buckling) and with or without presence of control rod fingers. The eight core configurations, summarized in Table 3-6, are divided in two subsets of layout; small (see Figure 3-14) or large (see Figure 3-15) water holes depending on CR finger cluster studied.

All of the 89 configurations were modeled in CASMO5 and show good agreement to measured data. The summary of the eigenvalue results is presented in Table 3-7. Out of the 89 cases, 5

of the experiments contained detailed normalized fission rate measurement data. These were also compared with CASMO5 predictions. Figure 3-17 through Figure 3-21 show the distributions of the measurements collapsed to the upper right quarter core, as done in Reference 25. These comparisons include the CASMO5 predicted fission rate, measured fission rate and absolute percent difference. Table 3-8 summarizes the fission rate comparison results. The CASMO5 average fission rate results agree well with measurement and fall within the 95% confidence experiment error is { }.

These critical experiments covered a wide range of operating temperatures to better demonstrate code performance at closer to PWR operating conditions. The calculated CASMO5 eigenvalues are plotted as a function of temperature in Figure 3-16 with good results. As can be seen in the figure there is a slight trend in eigenvalue with temperature, an approximate increase of { } pcm of the average. This trend is within the minimum to maximum spread of data, roughly { } pcm.

Overall the CASMO5 results compare well with measured reactivity and fission rate data. This shows that CASMO5 can perform PWR calculations at varying operating temperatures.

Table 3-6: KRITZ-3 Core Configuration Summary

Core Type	Fuel	Water holes	Control rods	Acronym
1	All UO2	Small	-	U-WH1
1	All UO2	Small	16	U-CR1
1	Central Pu	Small	-	Pu-WH1
1	Central Pu	Small	16	Pu-CR1
2	All UO2	Large	-	U-WH2
2	All UO2	Large	5	U-CR2
2	Central Pu	Large	-	Pu-WH2
2	Central Pu	Large	5	Pu-CR2

Figure 3-14: KRITZ-3 Small Water Hole Model Geometry (U-WH1)

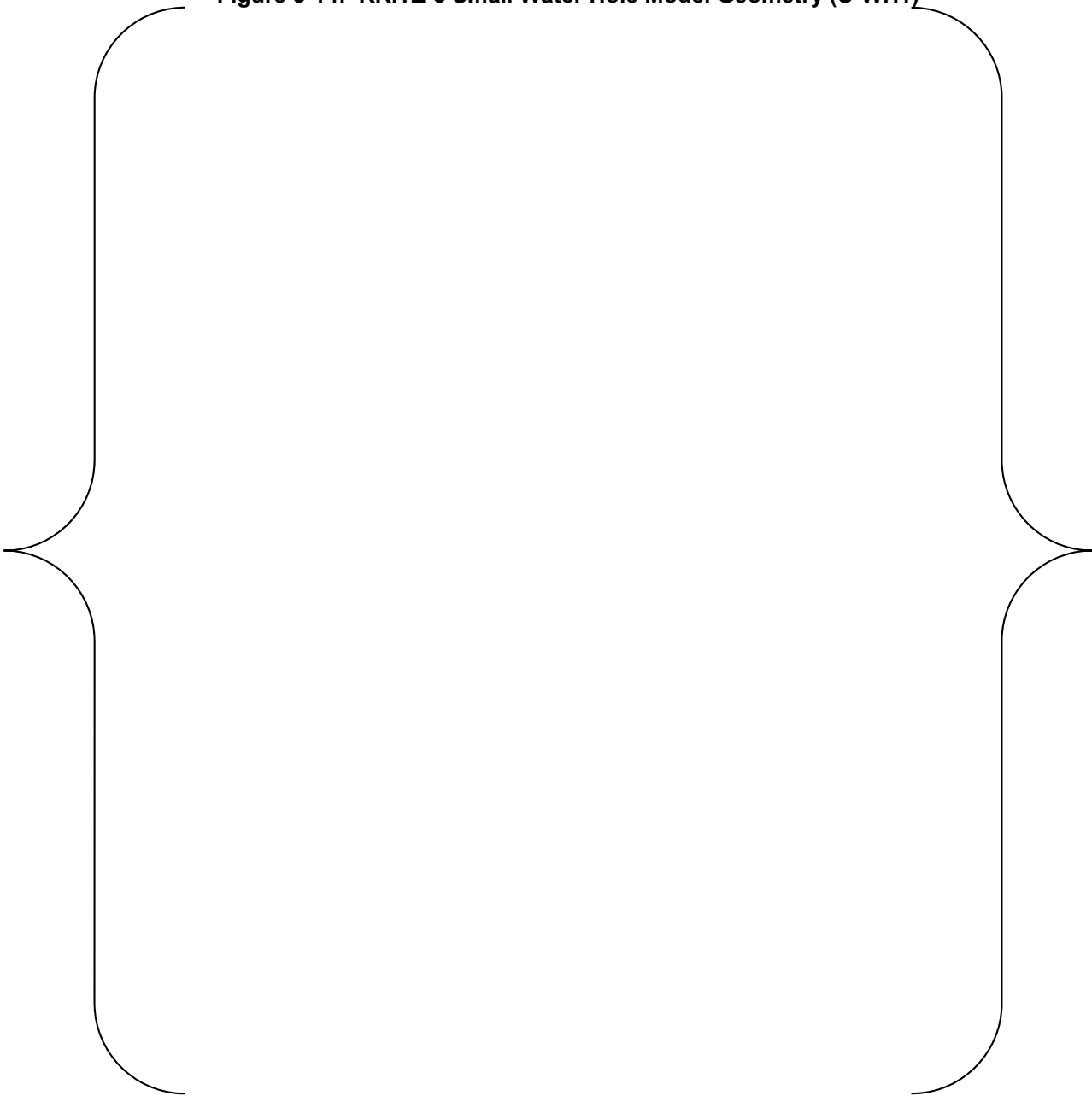


Figure 3-15: KRITZ-3 Large Water Hole Model Geometry (U-WH2)

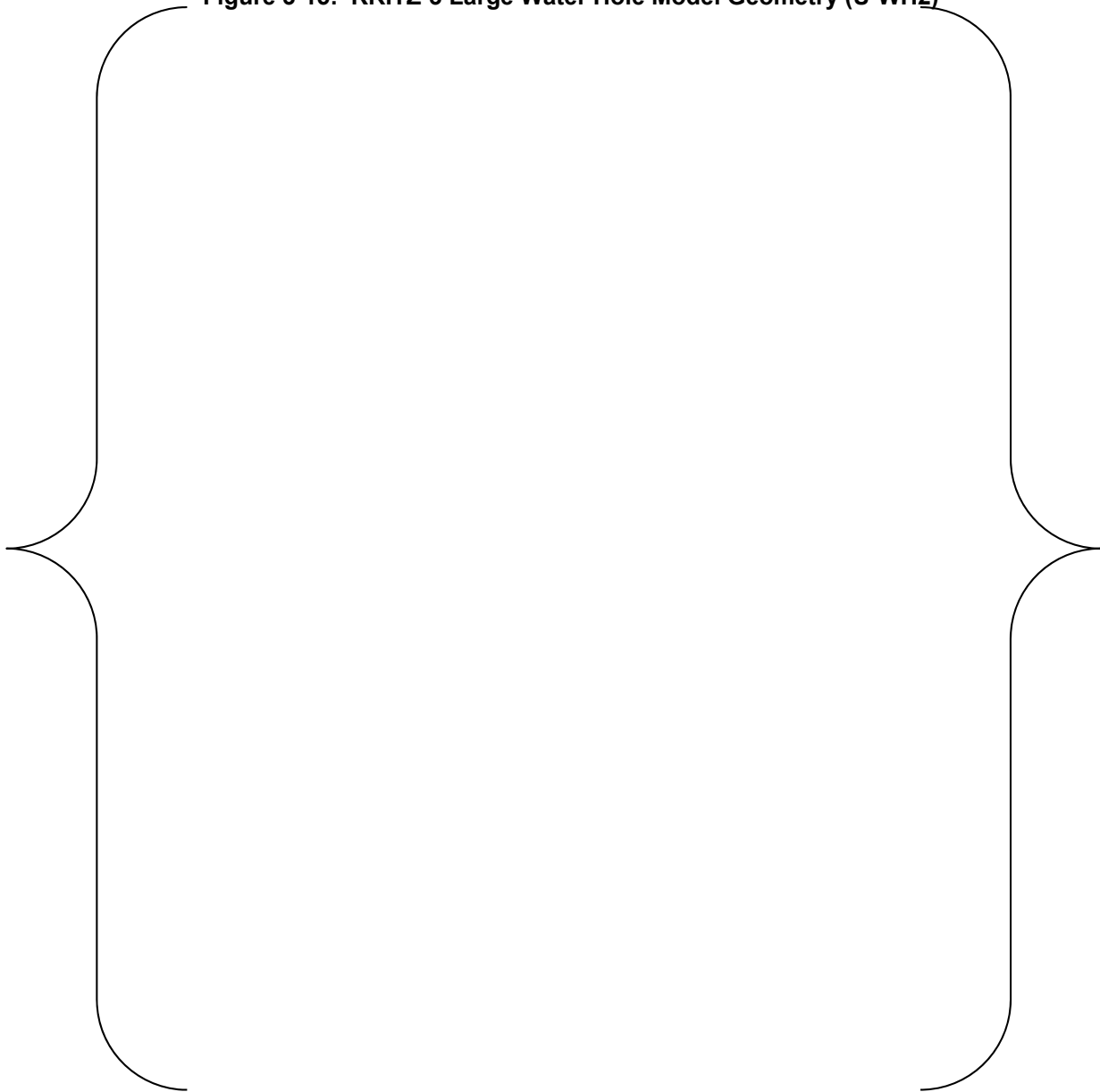


Table 3-7: KRITZ-3 CASMO5 Summary Eigenvalue Results

Core type	Average Eigenvalue	Standard-Deviation of Differences (pcm)	Number of measurement points
All	{ }	{ }	89
UO2	{ }	{ }	43
Pu	{ }	{ }	46
Type 1 Small Guide Tubes			
UO₂ and Pu core	{ }	{ }	45
AIC CR inserted	{ }	{ }	23
Type 2 Big Guide Tubes			
UO₂ and Pu core	{ }	{ }	44
B₄C CR inserted	{ }	{ }	20

Figure 3-16: KRITZ-3 CASMO5 Eigenvalue vs. Temperature



Figure 3-17: KRITZ-3 U-WH1 Fission Rate Comparison Map (229.0°C, 1006 ppm)

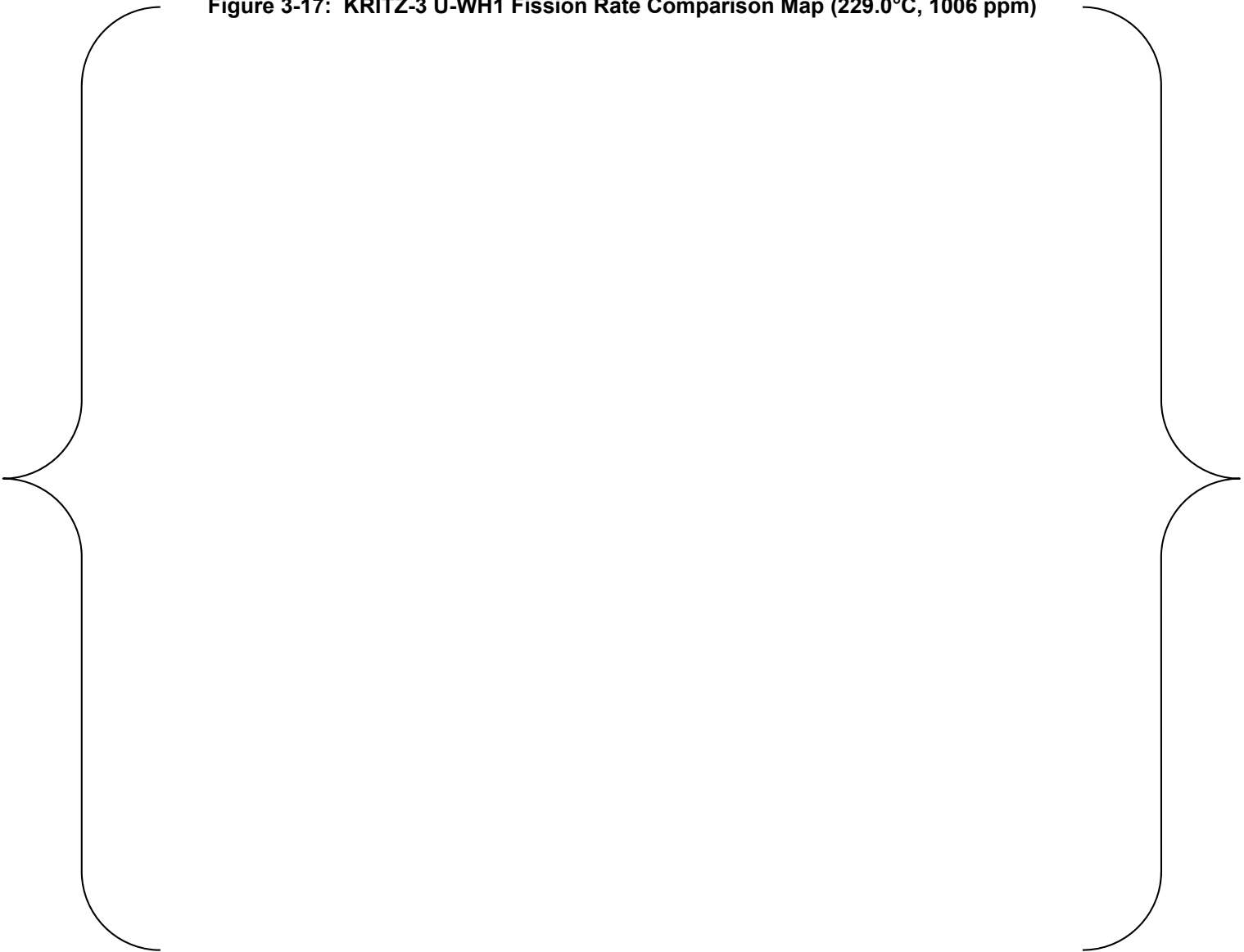


Figure 3-18: KRITZ-3 Pu-WH1 Fission Rate Comparison Map (223°C, 990ppm)

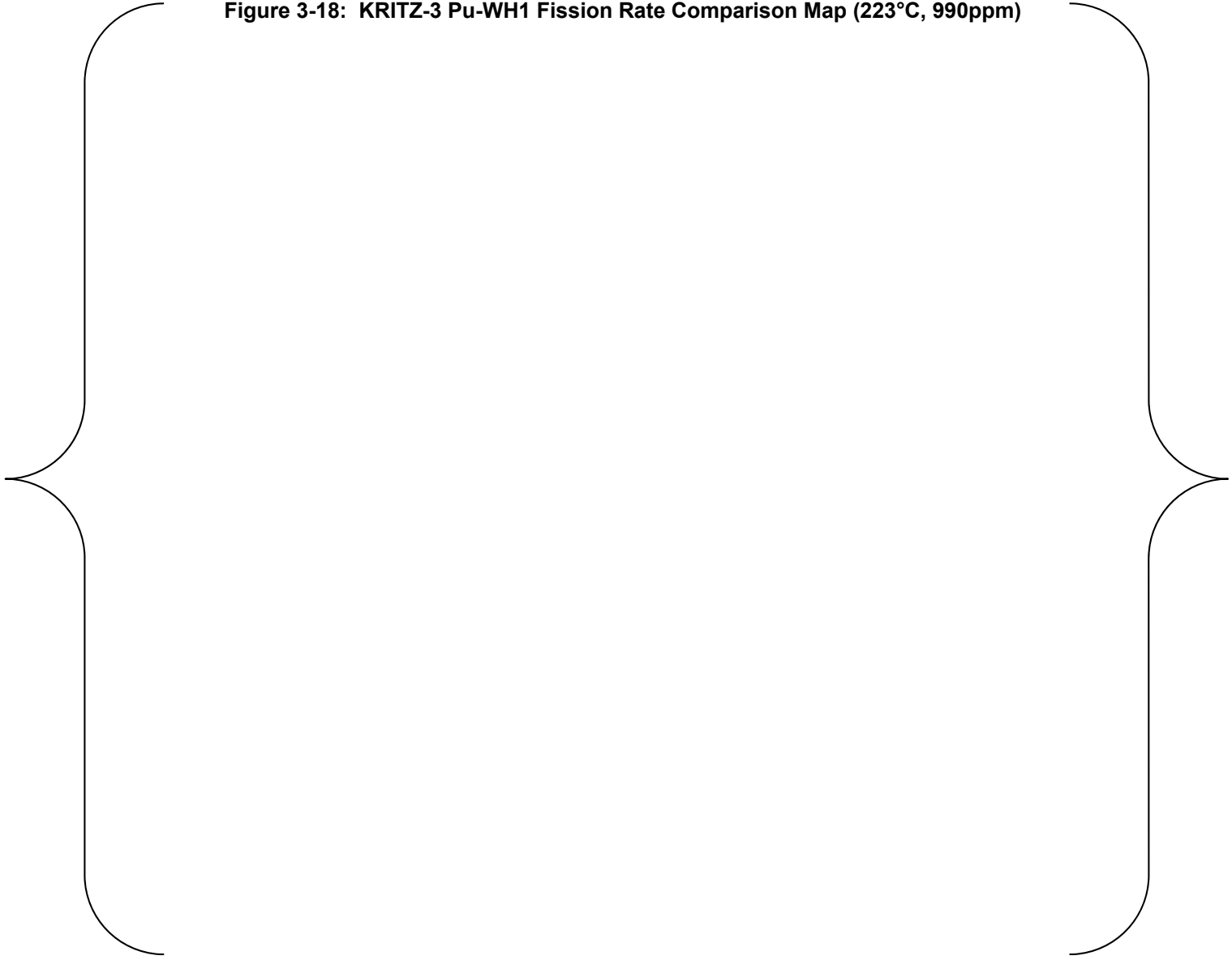


Figure 3-19: KRITZ-3 U-WH2 Fission Rate Comparison Map (229°C, 959ppm)

Figure 3-20: KRITZ-3 Pu-WH2 Fission Rate Comparison Map (25°C, 1122 ppm)

Figure 3-21: KRITZ-3 Pu-WH2 Fission Rate Comparison Map (231°C, 949 ppm)

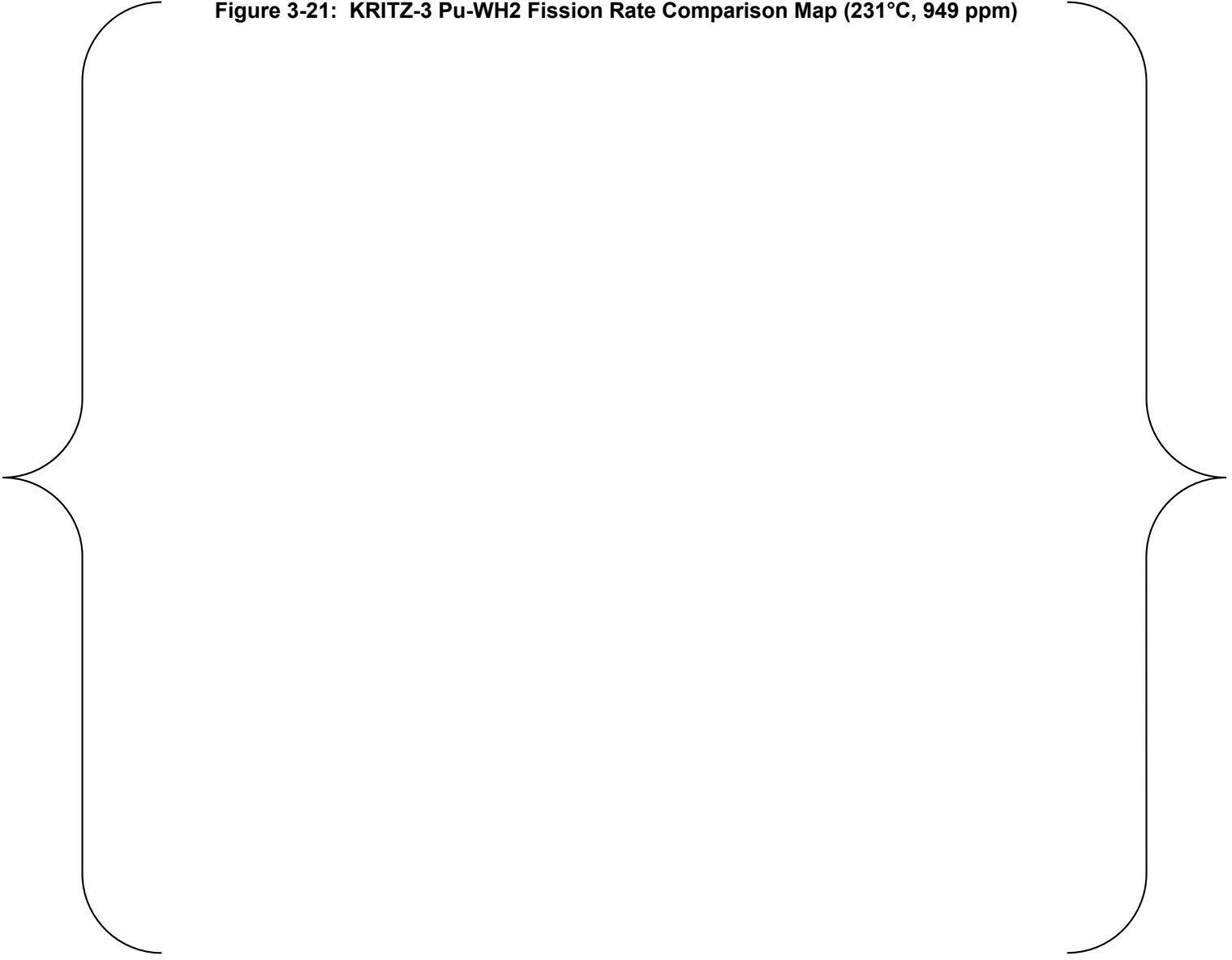


Table 3-8: KRITZ-3 CASMO5 Fission Rate Summary Results

Core Type	Value	Number of Measured Points
All Cores		
Average Absolute Error	{ }	110
Absolute Error Standard Deviation	{ }	
UO₂ Cores		
Average Absolute Error	{ }	31
Absolute Error Standard Deviation	{ }	
Pu Cores		
Average Absolute Error	{ }	79
Absolute Error Standard Deviation	{ }	

3.2.1.4 AEA Winfrith DIMPLE

The DIMPLE criticals are modeled to demonstrate that CASMO5 can model core configurations with and without a baffle. It also provides detailed fission rate comparisons to validate both fast the thermal fission distributions.

The AEA Winfrith DIMPLE experimental program extended previous studies in water-reflected cylindrical systems to power reactor geometries by assembling a cruciform array of 3%-enriched uranium dioxide fuel pins. The array simulated the rectangular corner configuration of a Pressurized Water Reactor (PWR) and effectively represented twelve PWR fuel assemblies (see Figure 2-1). Two versions of the cruciform assembly were constructed (Reference 24), the first being water-reflected as with the cylindrical systems. The assembly was then surrounded azimuthally by a stainless steel region simulating a PWR core baffle. The experiments were performed in three separate phases, collectively known as the S06 series. The first phase, S06A and B, have been analyzed with CASMO5, Reference 35.

The CASMO5 calculated eigenvalues are shown in Table 3-9 and agree well with the experiment and demonstrate that CASMO5 can predict reactivity well with and without a baffle present.

These experiments also include detailed fission rate measurements by isotope. Normalized fission rate distributions of the South East quarter core assemblies are shown for ²³⁵U (thermal fissions) and ²³⁸U (fast fissions). The S06A distributions are shown in Figure 3-25 through Figure 3-29 and the S06B distributions are shown in Figure 3-30 through Figure 3-34. The comparisons show good overall and spatial agreement of CASMO5 with the experimental values. The summary of the fission rate comparison results are shown in Table 3-10, with average errors all less than 1%.

Figure 3-22: DIMPLE Geometry Overview

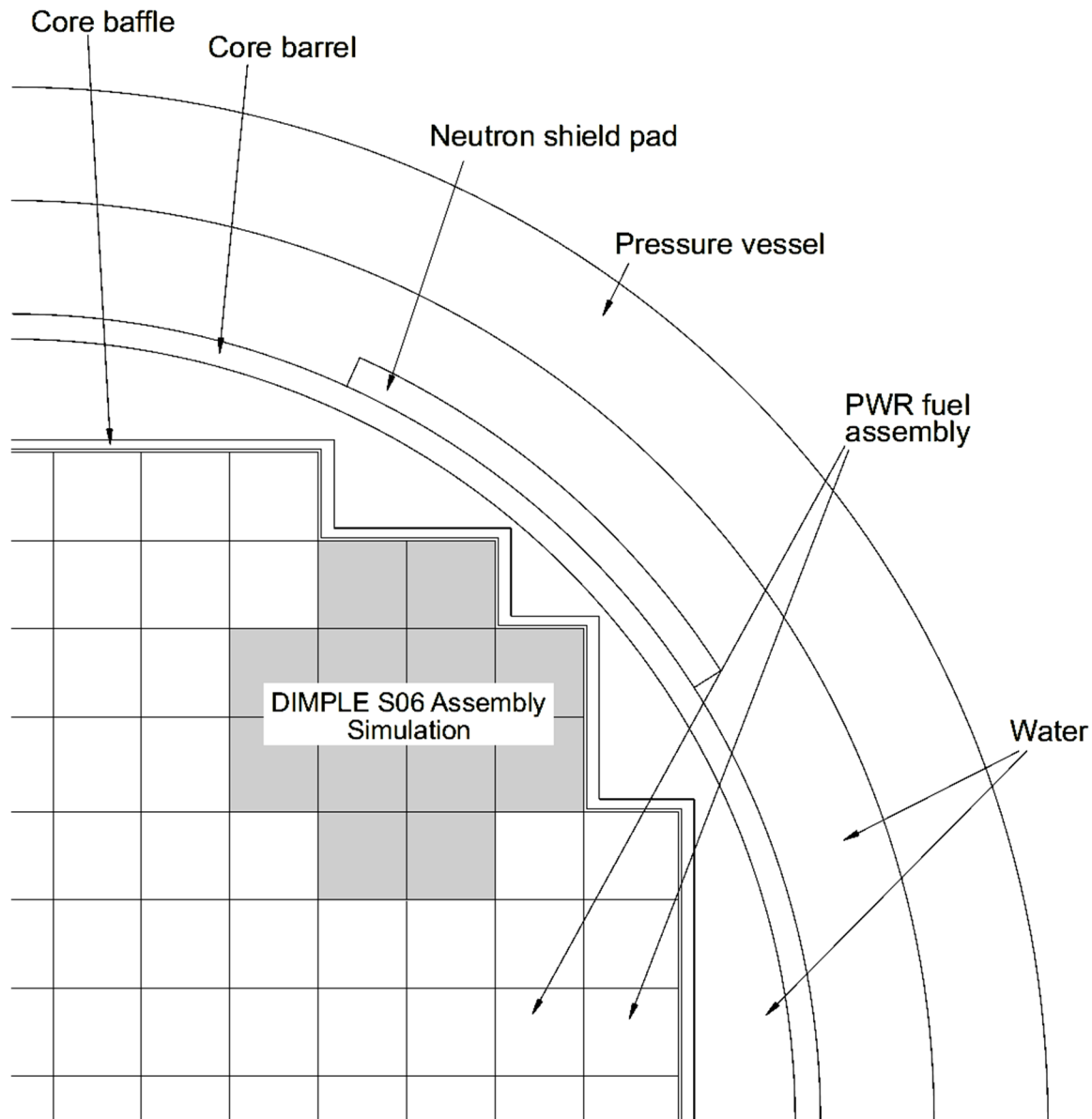


Figure 3-23: DIMPLE S06A Fission Rate Measurement Locations

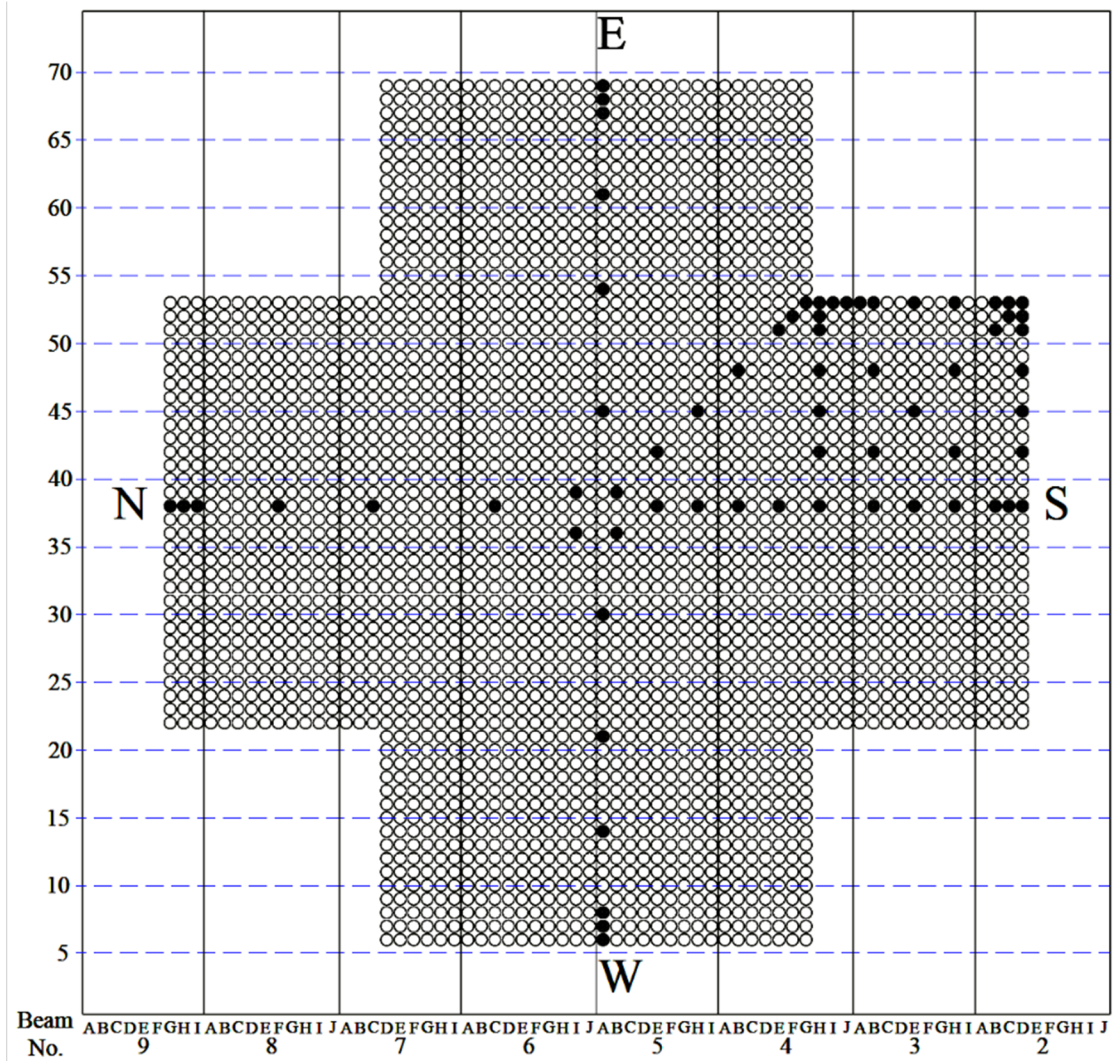


Figure 3-24: DIMPLE S06B Fission Rate Measurement Locations

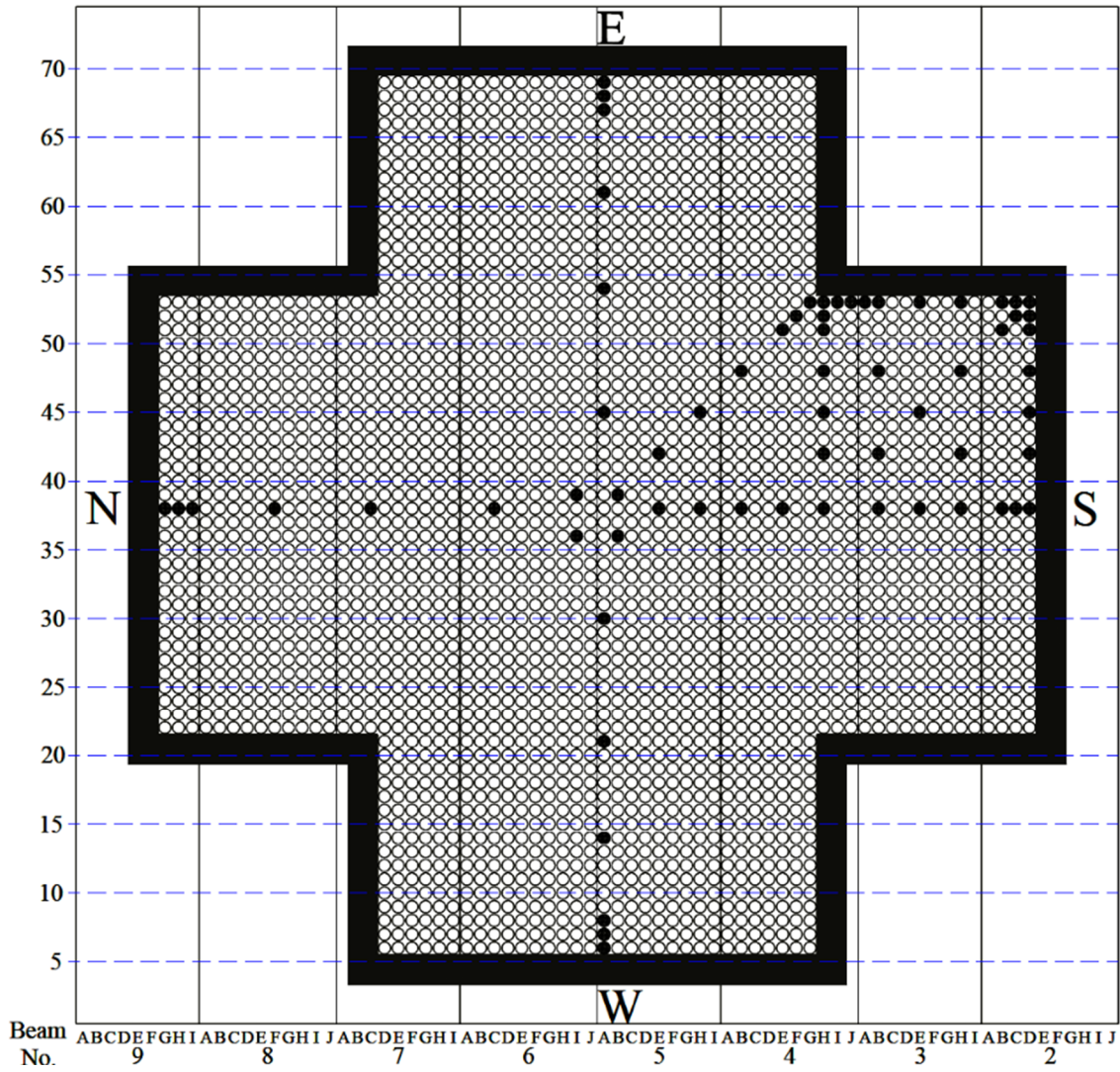


Figure 3-25: S06A U235 Fission Rate Distribution (Upper Left Assembly of SE Quadrant)



Figure 3-26: S06A U235 Fission Rate Distribution (Lower Left Assembly of SE Quadrant)

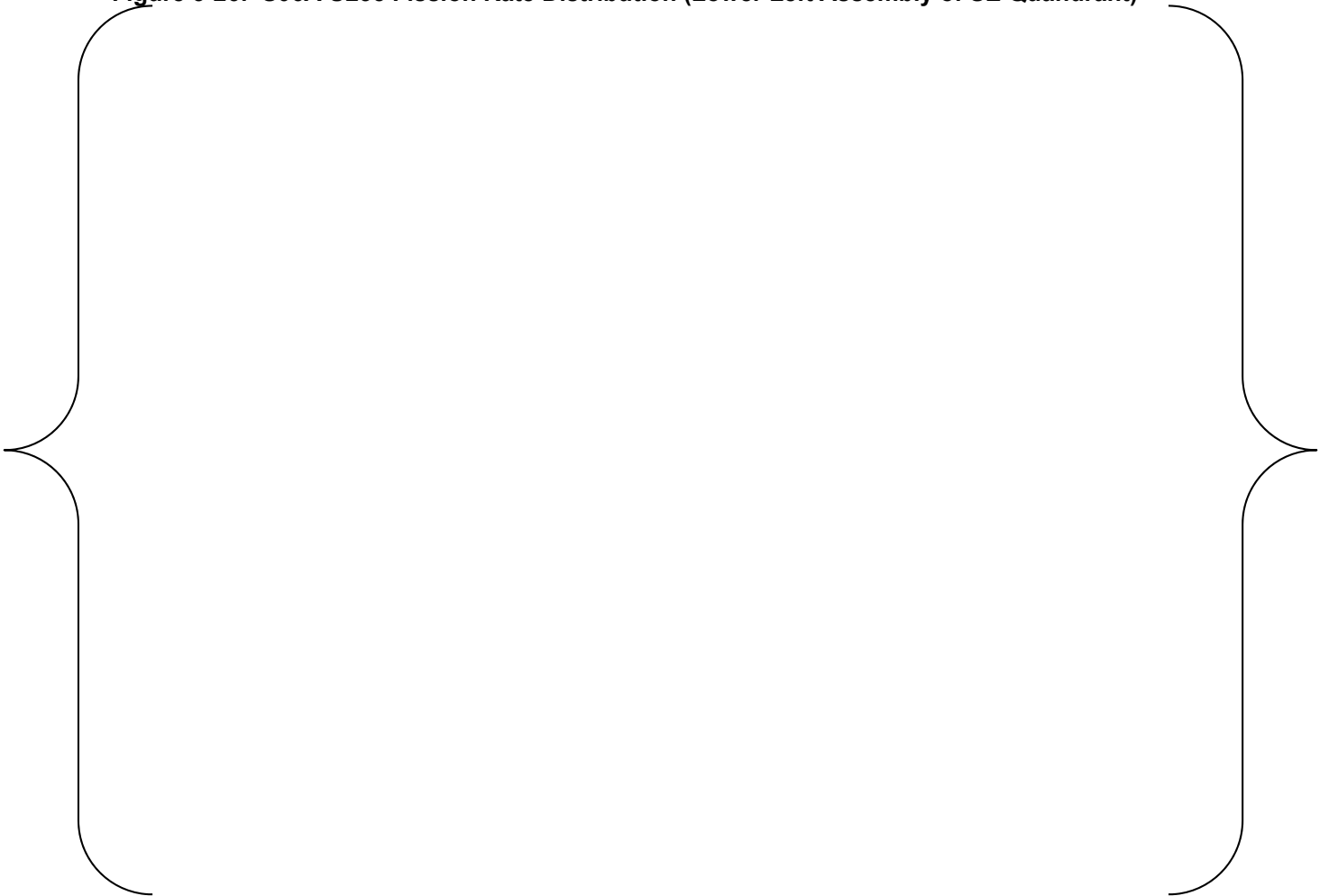


Figure 3-27: S06A U235 Fission Rate Distribution (Lower Right Assembly of SE Quandrant)

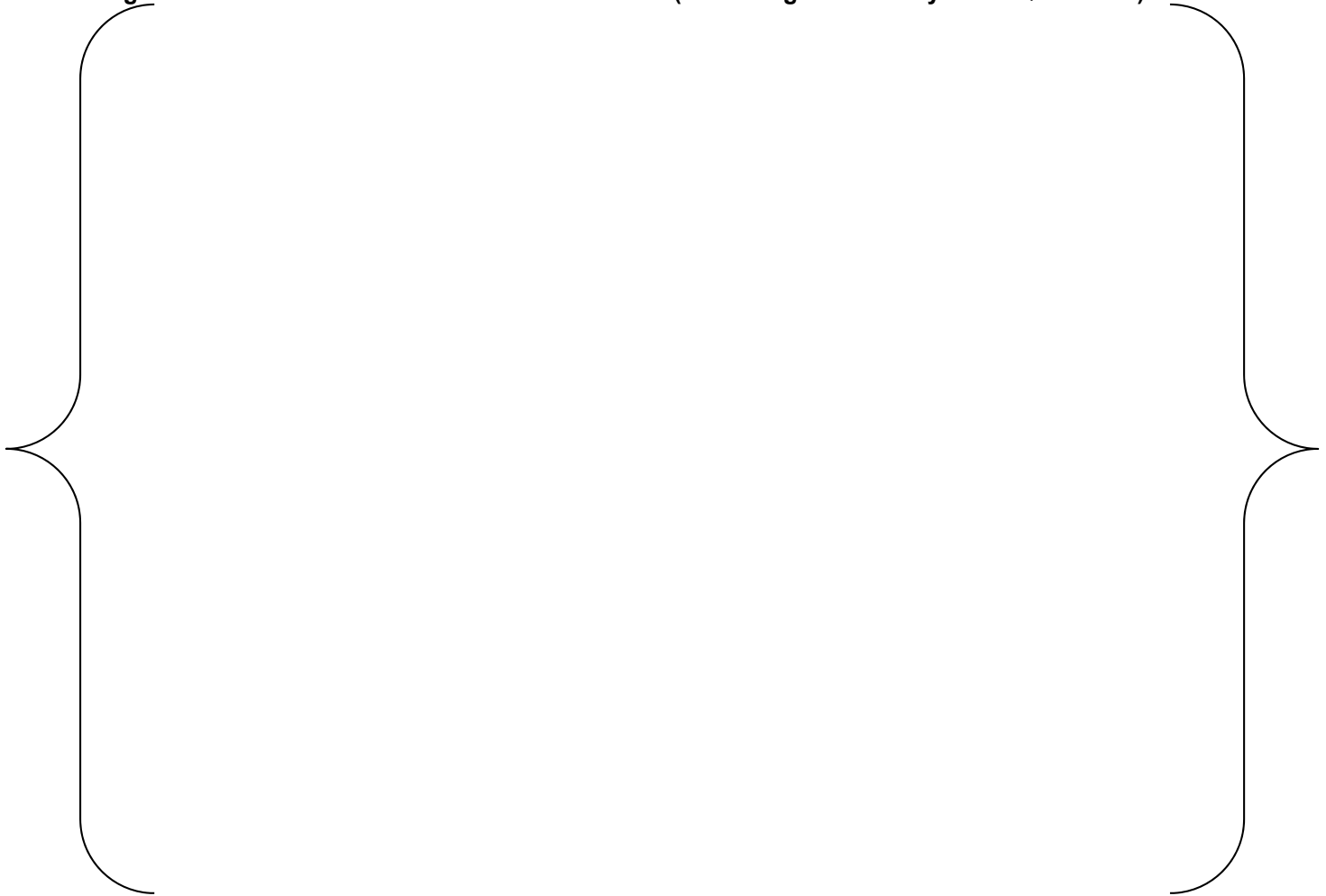


Figure 3-28: S06A U238 Fission Rate Distribution (Lower Left Assembly of SE Quadrant)

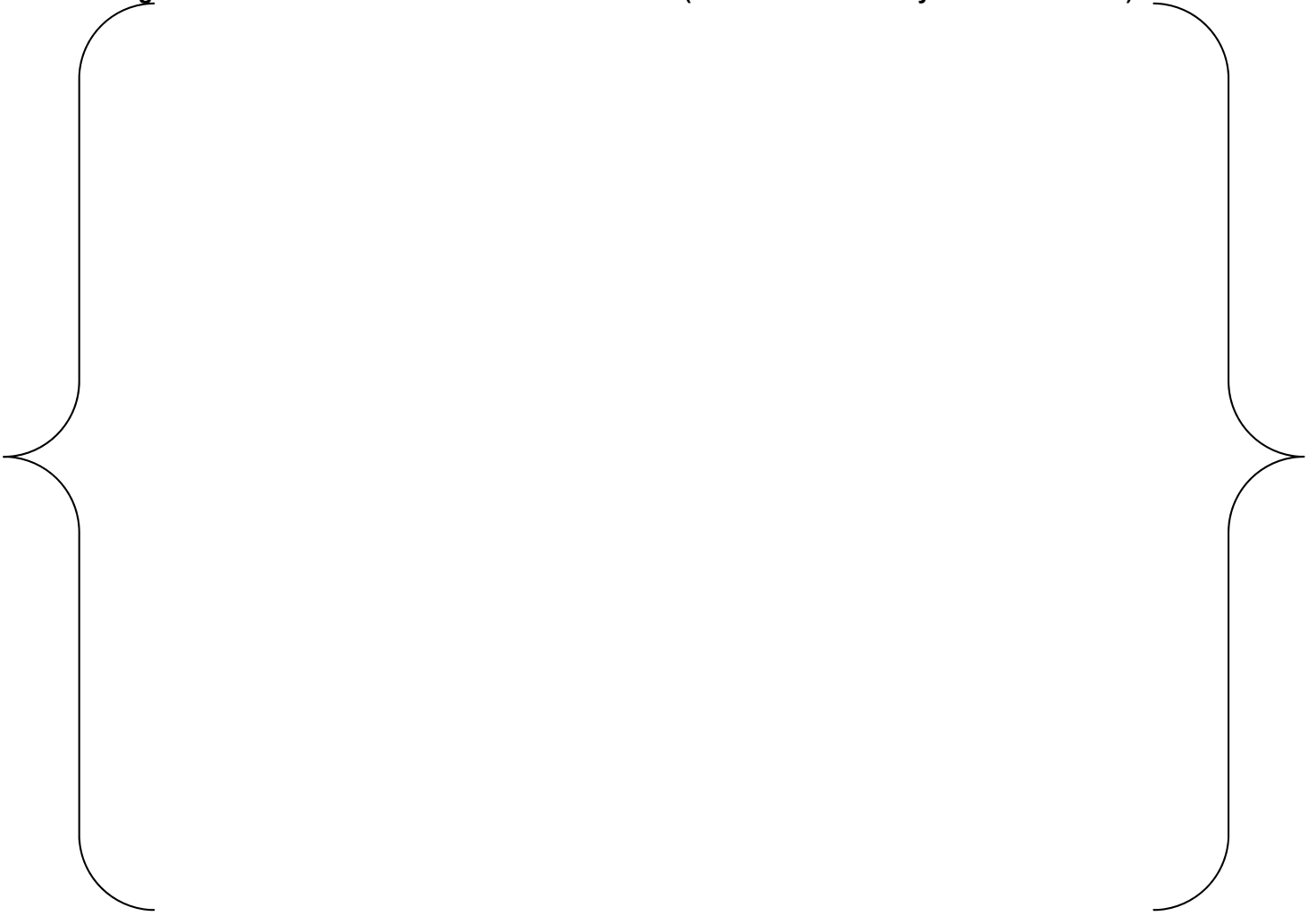


Figure 3-29: S06A U238 Fission Rate Distribution (Lower Right Assembly of SE Quadrant)

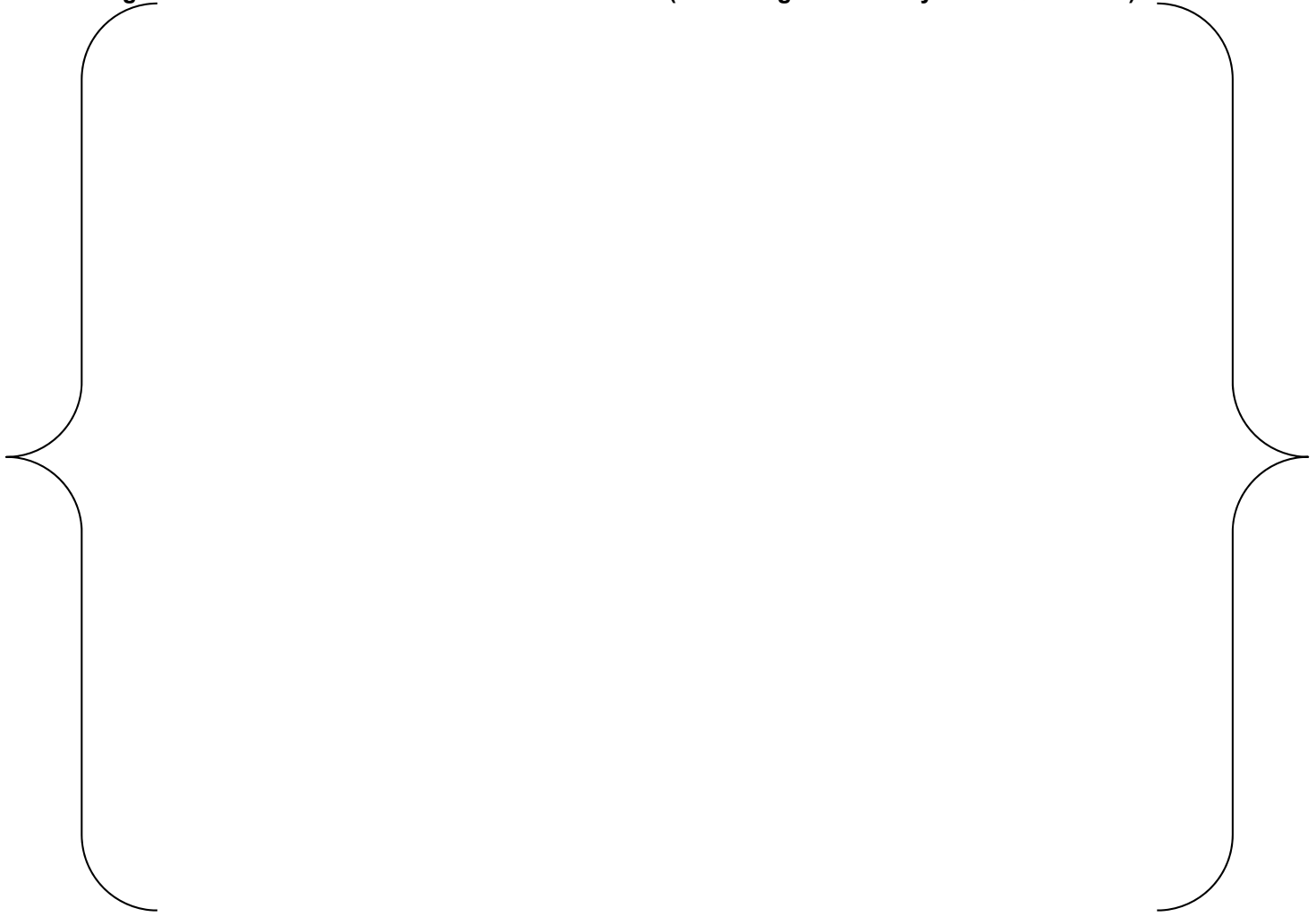


Figure 3-30: S06B U235 Fission Rate Distribution (Upper Left Assembly of SE Quadrant)

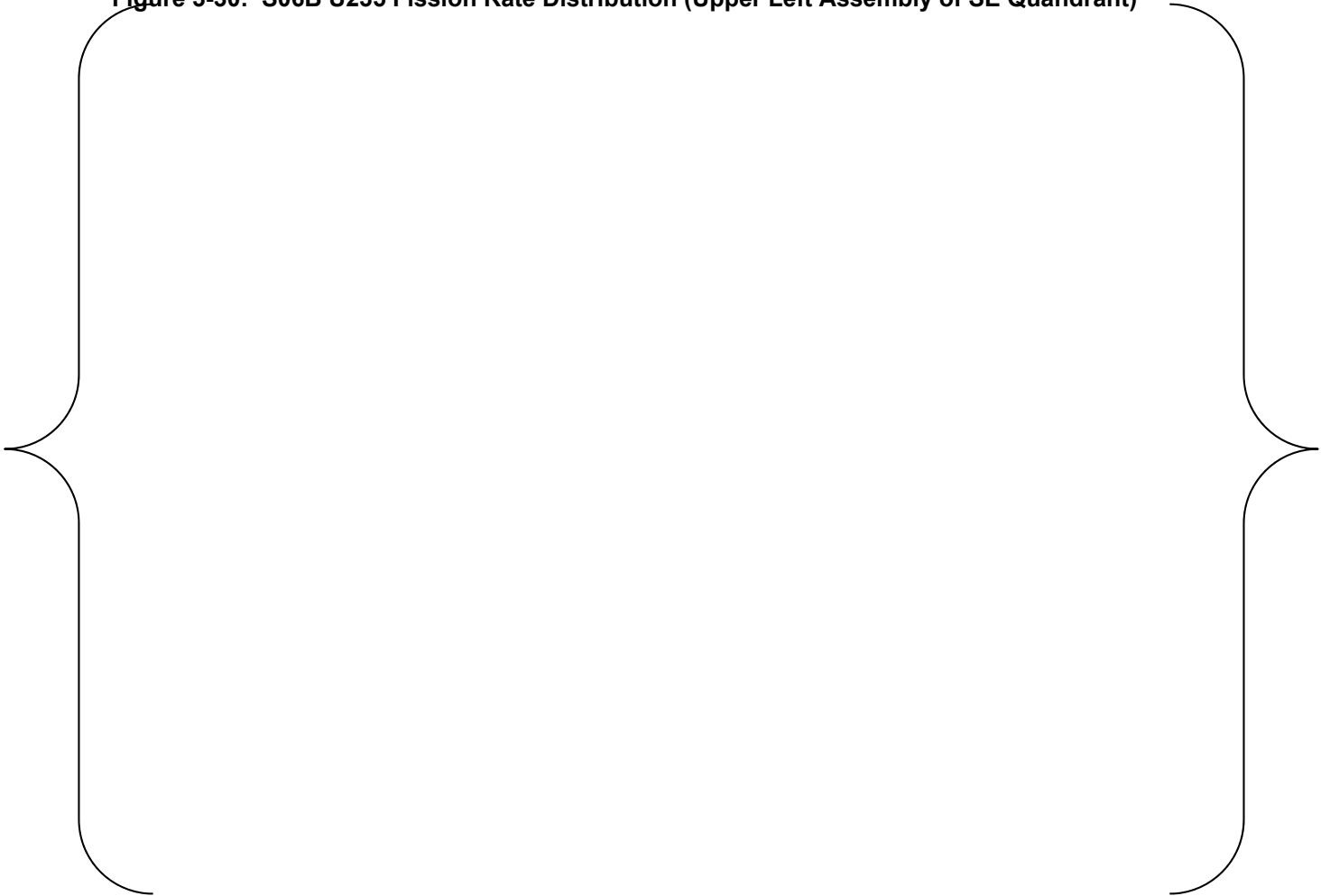


Figure 3-31: S06B U235 Fission Rate Distribution (Lower Left Assembly of SE Quadrant)

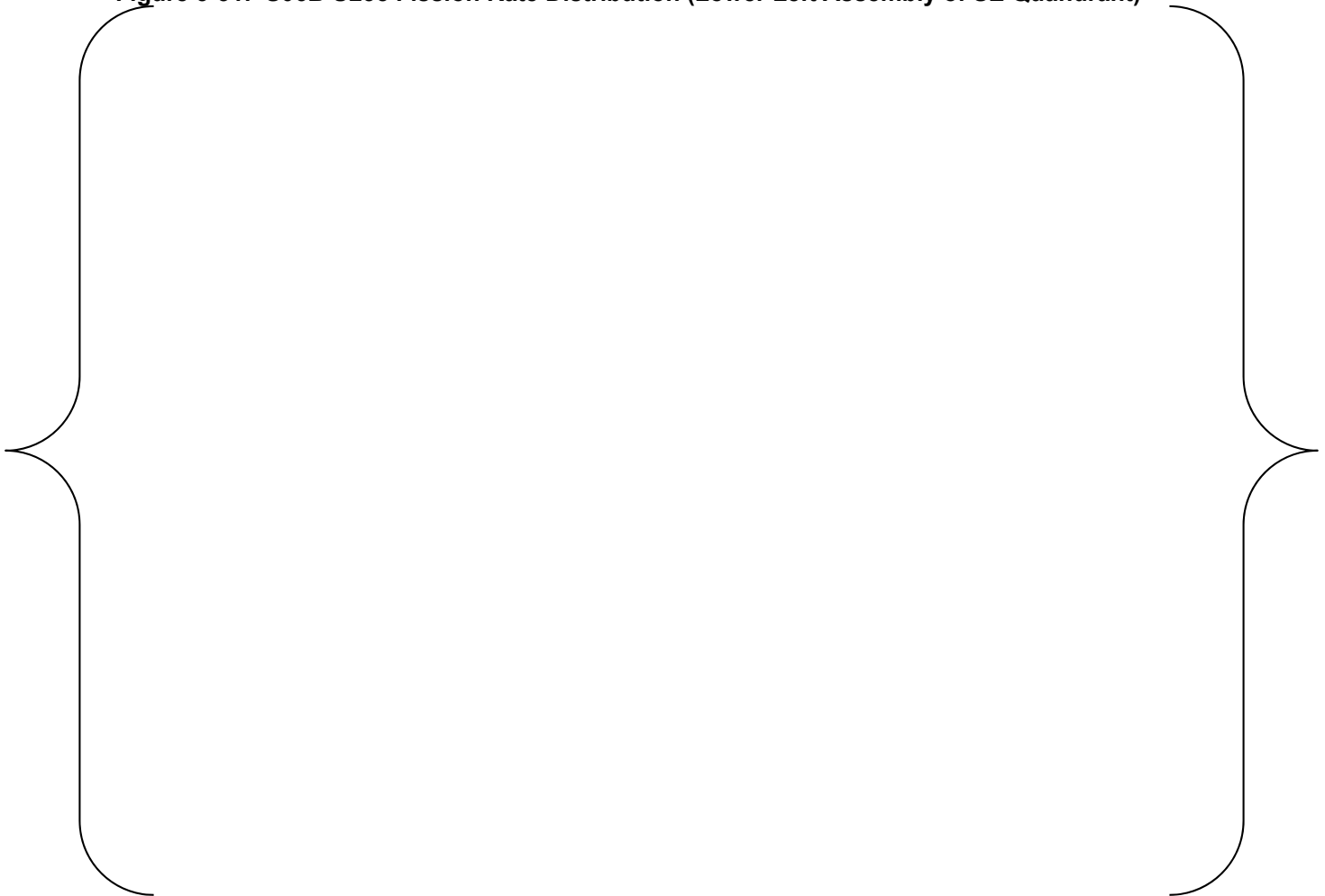


Figure 3-32: S06B U235 Fission Rate Distribution (Lower Right Assembly of SE Quandrant)

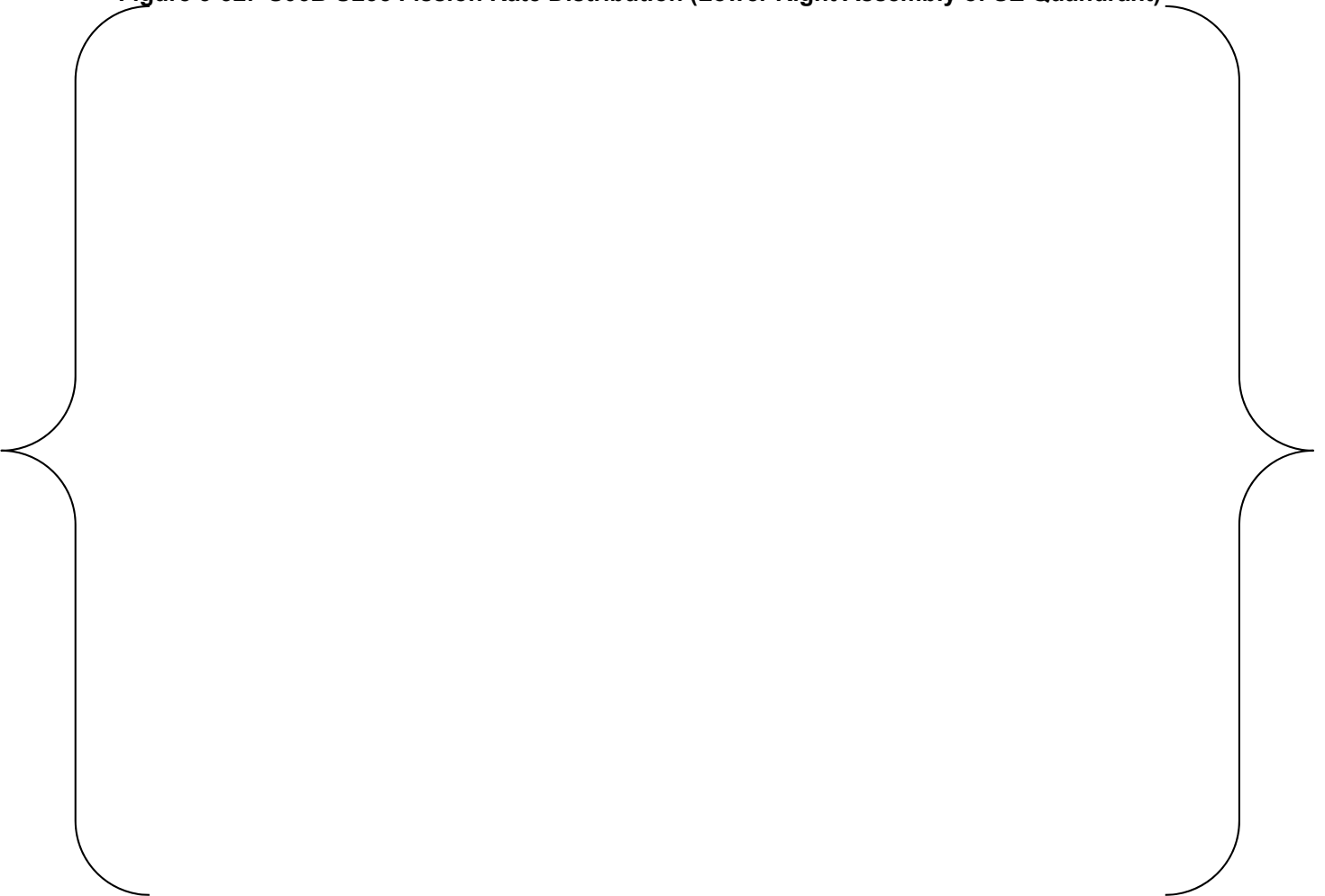


Figure 3-33: S06B U238 Fission Rate Distribution (Lower Left Assembly of SE Quadrant)

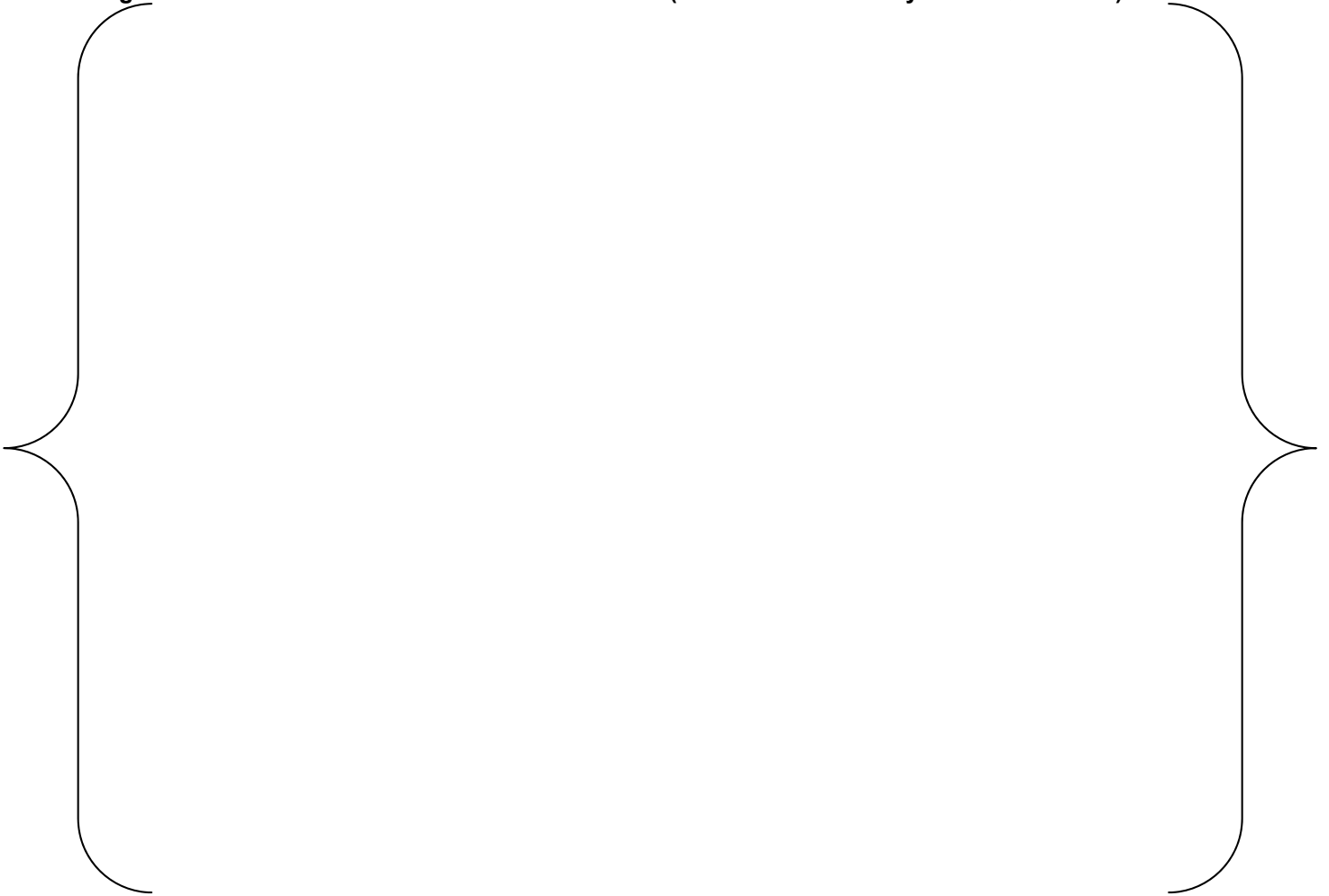


Figure 3-34: S06B U238 Fission Rate Distribution (Lower Right Assembly of SE Quadrant)

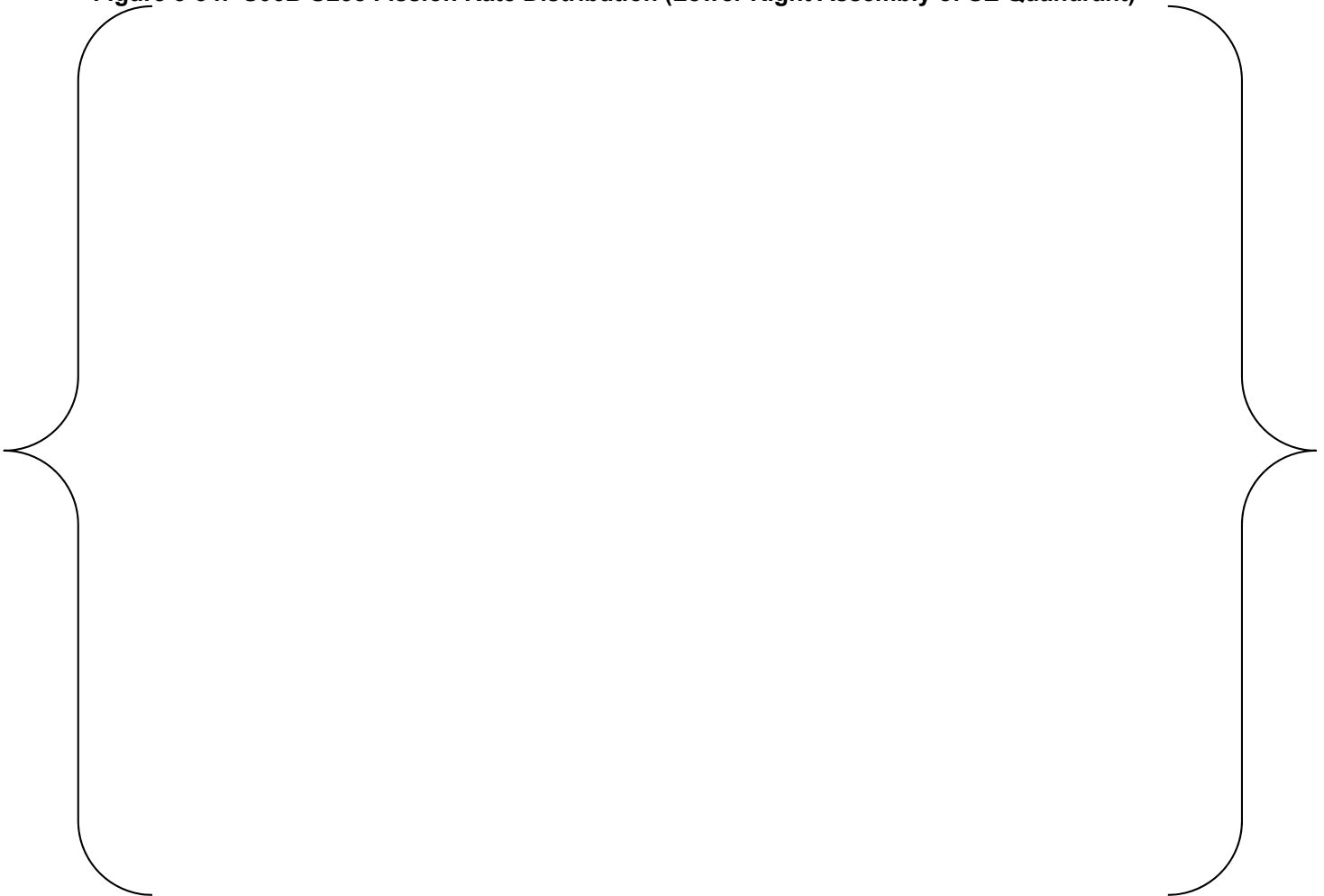


Table 3-9: CASMO5 DIMPLE Eigenvalue Results

Configuration	$K_{\text{effective}}$
S06A	{ }
S06B	{ }

Table 3-10: CASMO5 DIMPLE Fission Rate Summary Results

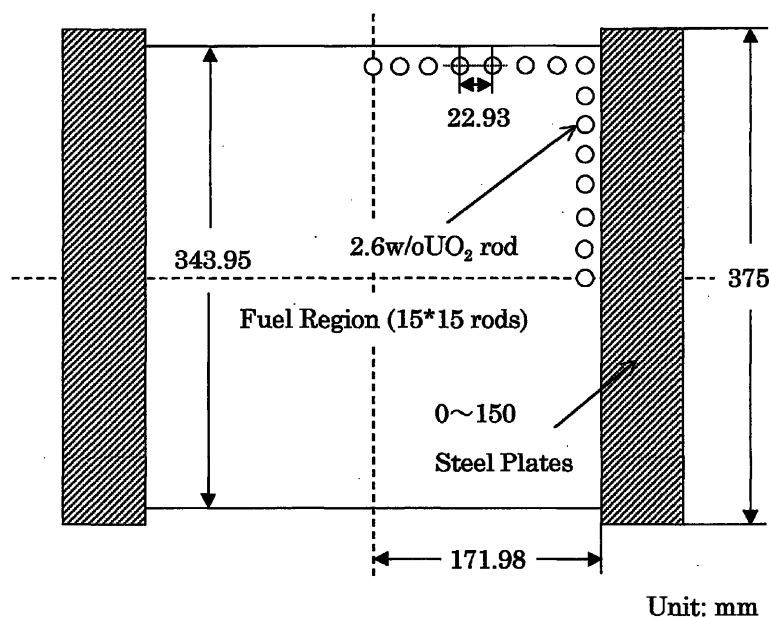
Core Type	Value	Number of Measured Points
S06A (Bare)		
Average Absolute Error	U235 { } U238 { }	U235 - 169 U238 - 126
Absolute Error Standard Deviation	U235 { } U238 { }	
RMSE	U235 { } U238 { }	
S06B (Baffle)		
Average Absolute Error	U235 { } U238 { }	U235 - 196 U238 - 172
Absolute Error Standard Deviation	U235 { } U238 { }	
RMSE	U235 { } U238 { }	

3.2.1.5 TCA Reflector Experiments

The TCA experiment was chosen to demonstrate that CASMO5 can appropriately model reflectors of varying thickness, and predict kinetic data as compared to measurement.

Experimental critical configurations were reported for 2.6% enriched typical 15x15 PWR fuel assemblies with various configurations of steel and steel/water reflector slabs in Reference 26. The experiments were carried out using the Tank type Critical Assembly (TCA) at Tokai Research Establishment of JAERI. The objectives were to measure the reactivity effect of the steel reflector plates and reflectors containing about 90% steel and 10% water. A diagram of the experiment configuration is shown in Figure 3-35.

Figure 3-35: TCA Reflector Experiment Configuration



The reported experimental conditions and results allow for benchmark comparisons of the reported reflector reactivity worth, and each critical configuration's calculated eigenvalue to CASMO5 (Reference 41) results under the same conditions. In addition, the CASMO5 calculated β_{eff}/l^* for a bare water reflected configuration is compared.

The eigenvalue results calculated in CASMO5 are shown below in Table 3-11. It can be seen that the results do compare well and there is an increasing trend of eigenvalue with increasing steel reflector thickness.

The comparison of the ratio of β_{eff}/l^* in Table 3-12 shows very good agreement with the measurement and is within the experimental uncertainty.

The reactivity effect of the different reflector configurations is compared in Table 3-13. The results of CASMO5 compare well with the benchmark and show very similar trends as can be seen in Figure 3-36 and Figure 3-37.

The overall results show that CASMO5 can appropriately model heavy reflectors. Also the kinetics data measurements show that the information used in CASMO5 is appropriate for PWR modeling.

Table 3-11: CASMO5 TCA Eigenvalue and β_{eff} Results

Reflector Configuration	CASMO5 β_{eff}	CASMO5 Eigenvalue	Delta (pcm) from Unity
0.0 cm steel	{ }	{ }	{ }
0.56 cm steel	{ }	{ }	{ }
2.80 cm steel	{ }	{ }	{ }
3.36 cm steel	{ }	{ }	{ }
6.16 cm steel	{ }	{ }	{ }
8.96 cm steel	{ }	{ }	{ }
11.76 cm steel	{ }	{ }	{ }
15.12 cm steel	{ }	{ }	{ }
3.73 cm steel/water	{ }	{ }	{ }
6.79 cm steel/water	{ }	{ }	{ }
9.96 cm steel/water	{ }	{ }	{ }
13.07cm steel/water	{ }	{ }	{ }
15.66 cm steel/water	{ }	{ }	{ }

Table 3-12: CASMO5 TCA β_{eff}/l^* Comparison (Bare Water Reflected)

	CASMO5	Measured
β_{eff}/l^*	{ }	{ }

Table 3-13: CASMO5 TCA Reflector Reactivity Comparisons

Reflector Configuration	"Reactivity Effect" CASMO5 (% $\Delta k/k$)	"Reactivity Effect" Reported (% $\Delta k/k$)	"Reactivity Effect" Percent Difference
0.0 cm steel	N/A	0.000	N/A
0.56 cm steel	{ }	{ }	{ }
2.80 cm steel	{ }	{ }	{ }
3.36 cm steel	{ }	{ }	{ }
6.16 cm steel	{ }	{ }	{ }
8.96 cm steel	{ }	{ }	{ }
11.76 cm steel	{ }	{ }	{ }
15.12 cm steel	{ }	{ }	{ }
3.73 cm steel/water	{ }	{ }	{ }
6.79 cm steel/water	{ }	{ }	{ }
9.96 cm steel/water	{ }	{ }	{ }
13.07 cm steel/water	{ }	{ }	{ }
15.66 cm steel/water	{ }	{ }	{ }

Figure 3-36: TCA Critical Steel Reflector Reactivity Effect

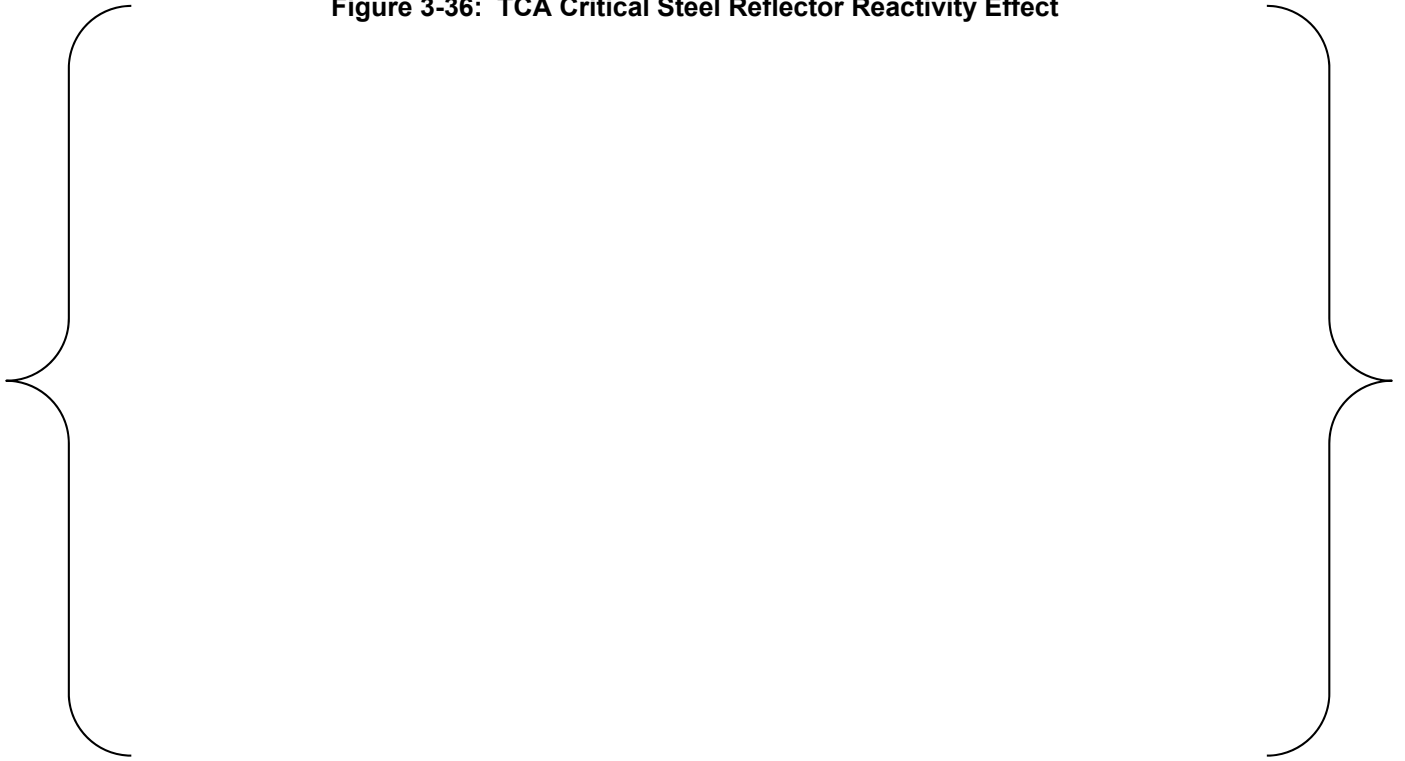
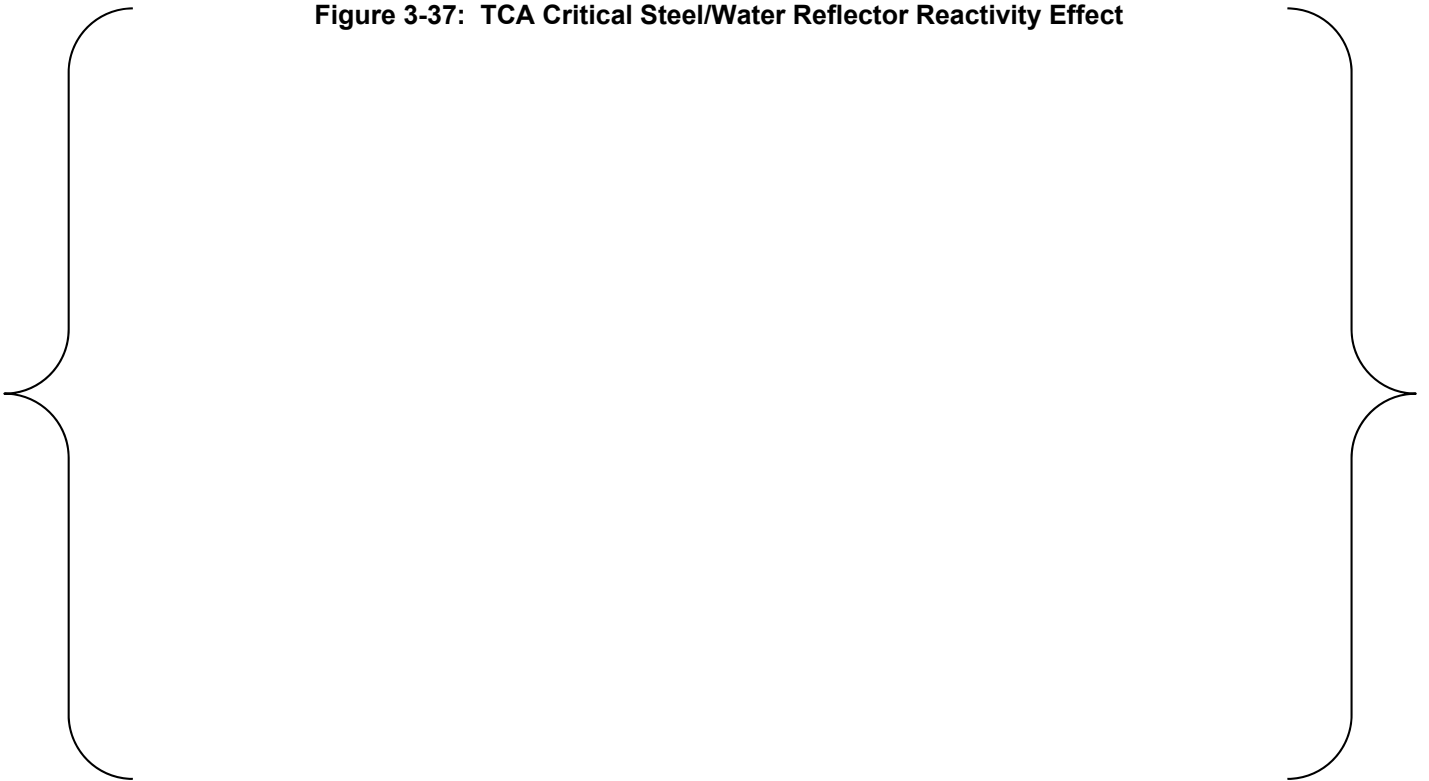


Figure 3-37: TCA Critical Steel/Water Reflector Reactivity Effect



3.2.2 Isotopic Measurements

This purpose of this section is to demonstrate that CASMO5 can predict isotopic burnup that is reasonable as compared to measurements.

3.2.2.1 Yankee Rowe Measurements

The Atomic Power Division of Westinghouse destructively analyzed samples from several burned PWR fuel pins of Yankee Rowe to measure nuclide composition for the purpose of verification of burnup codes, References 27 and 28.

An analysis has been performed with CASMO5, Reference 36 to compare the isotopic predictions with the measured reported data. Figure 3-38 through Figure 3-53 show the comparisons of isotope atom densities as a percent of initial ^{238}U between measurement and CASMO5.

The predictions are based on single assembly calculations depleted unrodded with a power history corresponding to core average conditions over the cycles containing the measured assemblies, including outages at zero power. The power levels for specific sample locations can differ significantly and these early cores of Yankee Rowe were operated at 0 ppm boron using control rods at power.

Isotopic concentrations in pins located far from the effects of the control blades/followers and corresponding variation in pin pitch are referred to as 'asymptotic'. Concentrations for pins adjacent to such components are referred to as 'perturbed', and pins located in regions in between are 'intermediate'.

Predictions are shown for representative asymptotic pins (near assembly centers, pin location CN f1), and the 'perturbed' location adjacent to the follower center (pin locations NW a1 and SW a5) for both assembly types A and B, as limiting examples. Assembly types A and B differ by control blade location.

The scatter in the measured data is, to some extent (depending on isotope) due to the variations in power level and local perturbations to the spectrum. The effects of variations in power level among the samples are not included in the predictions, since local pin powers are not available from published data.

The difference in the predicted curves for the asymptotic and perturbed locations indicate the sensitivity to local spectrum, and the sensitivity to power level is seen with short term variation in the trajectories corresponding to changes in power level. The isotopes ^{241}Am and ^{244}Cm exhibit a strong sensitivity to power while ^{238}U , ^{236}Pu and ^{232}U is much smaller. The other isotopes do not show the sensitivity. For isotopes sensitive to power level, local spectrum and for locations with significant control rod history, these predictions are qualitative and cannot be expected to match the measurements in detail.

The default option in CASMO5 simplifies some of the nuclide chains such that those leading to ^{232}U and ^{236}Pu , unimportant for reactivity and power distribution, are not complete. For comparisons to those nuclides only, the extended option is used to complete those chains. This option has negligible impact on the other nuclide concentrations.

Overall the results show that CASMO5 can reasonably predict the isotopic burnup trends of PWR fuel.

Figure 3-38: Yankee Rowe U232 CASMO5 Comparison to Measurement



Figure 3-39: Yankee Rowe U234 CASMO5 Comparison to Measurement

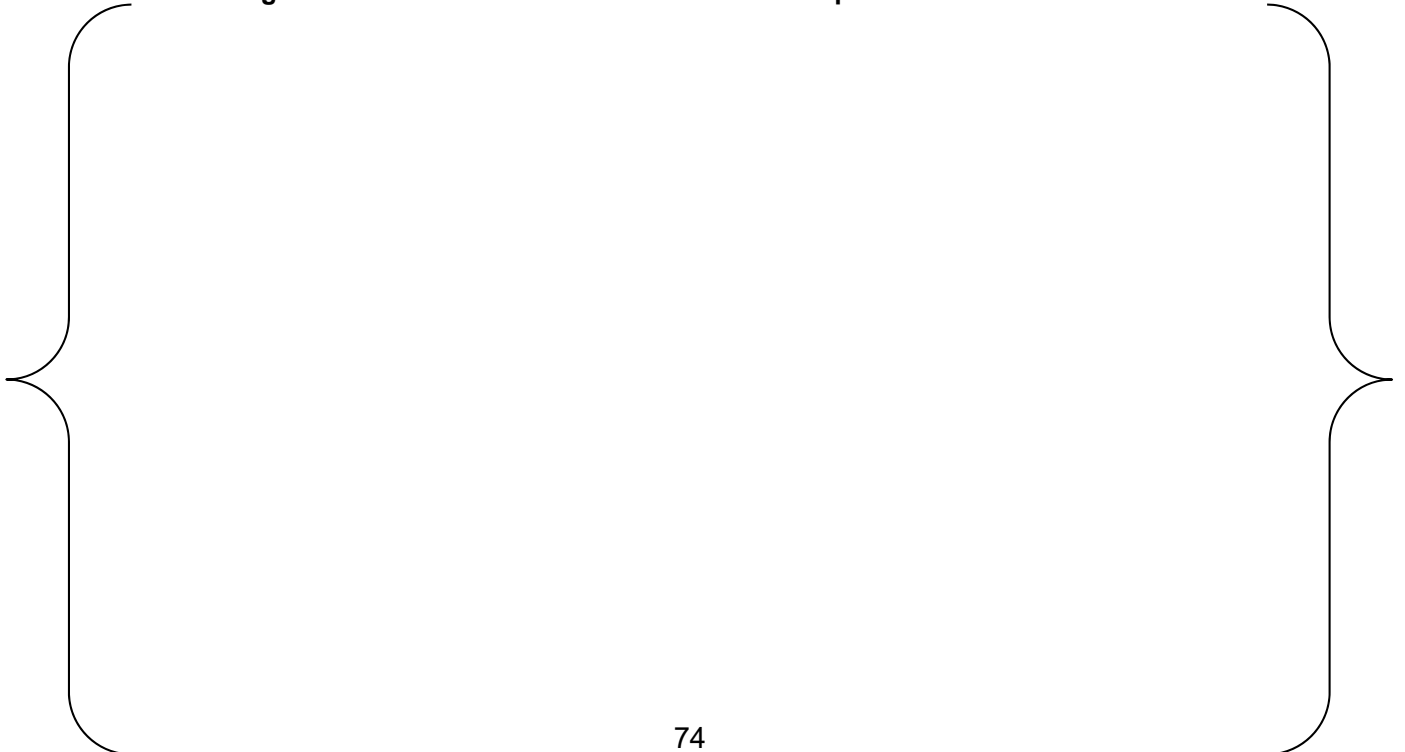


Figure 3-40: Yankee Rowe U235 CASMO5 Comparison to Measurement



Figure 3-41: Yankee Rowe U236 CASMO5 Comparison to Measurement



Figure 3-42: Yankee Rowe U238 CASMO5 Comparison to Measurement

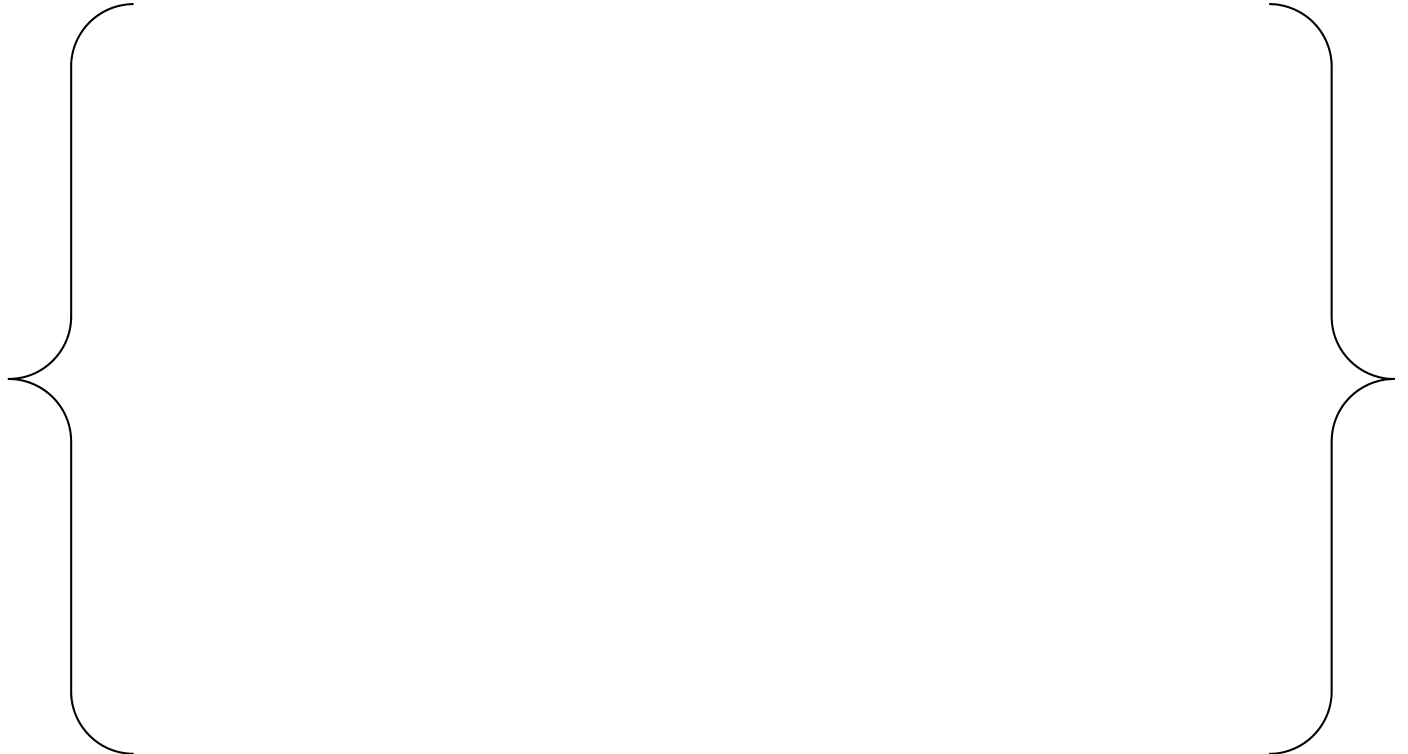


Figure 3-43: Yankee Rowe Np237 CASMO5 Comparison to Measurement



Figure 3-44: Yankee Rowe Pu236 CASMO5 Comparison to Measurement

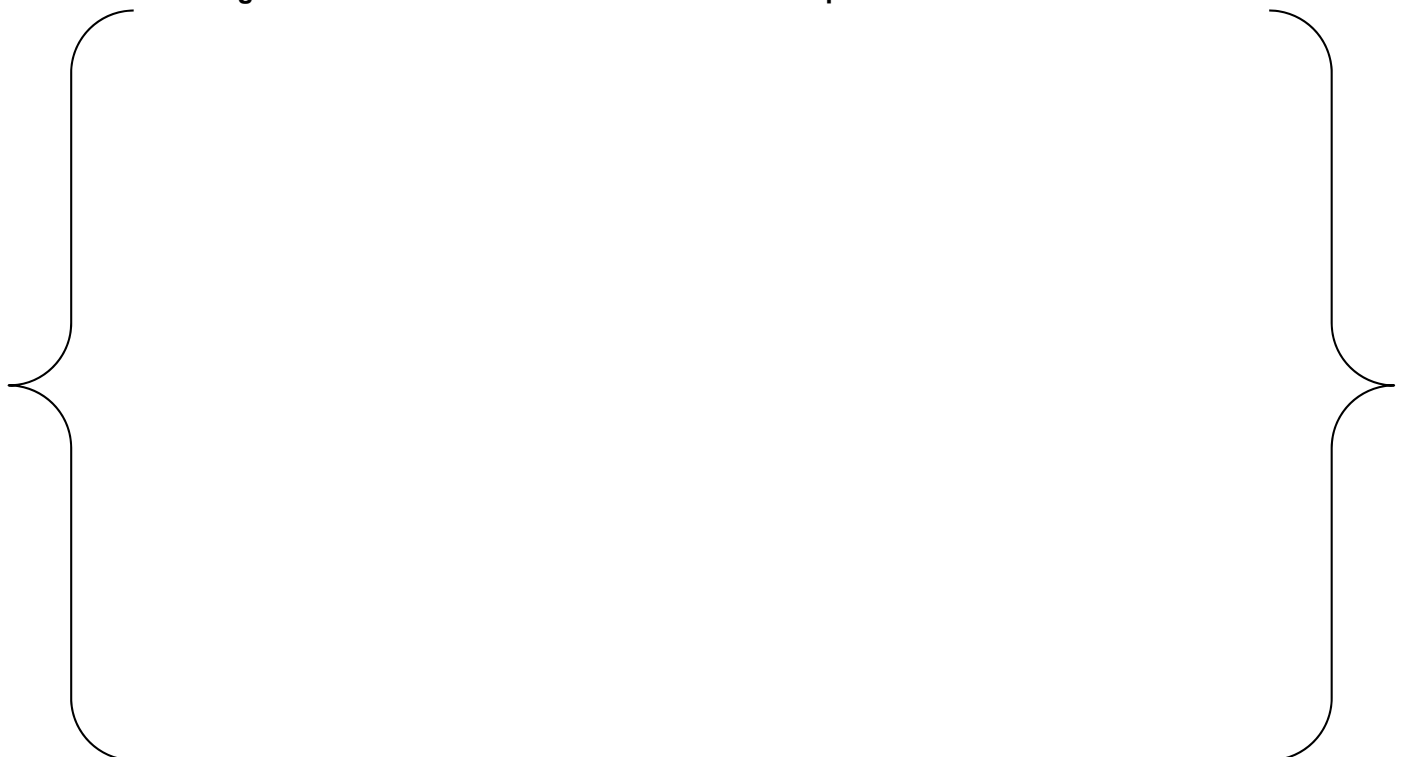


Figure 3-45: Yankee Rowe Pu238 CASMO5 Comparison to Measurement



Figure 3-46: Yankee Rowe Pu239 CASMO5 Comparison to Measurement



Figure 3-47: Yankee Rowe Pu240 CASMO5 Comparison to Measurement

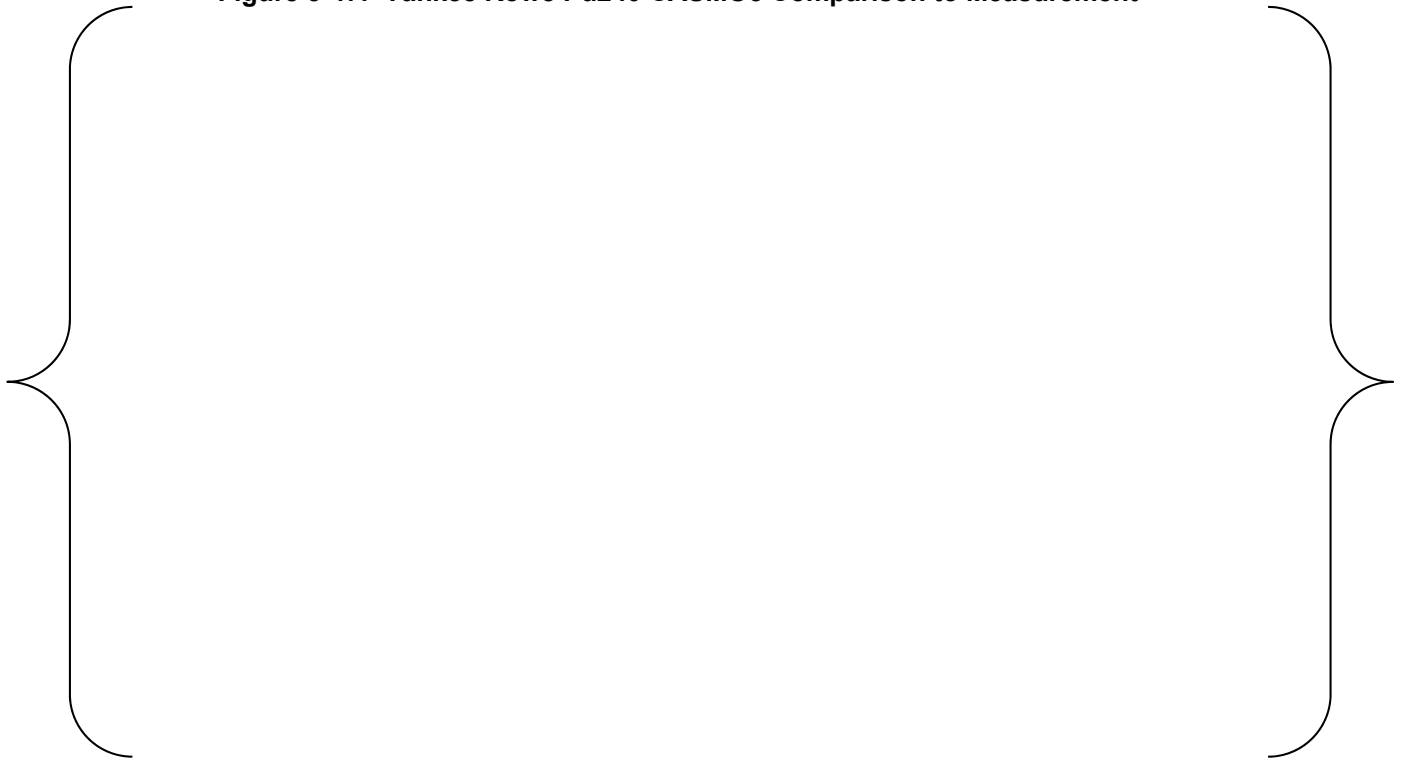


Figure 3-48: Yankee Rowe Pu241 CASMO5 Comparison to Measurement



Figure 3-49: Yankee Rowe Pu242 CASMO5 Comparison to Measurement



Figure 3-50: Yankee Rowe Am241 CASMO5 Comparison to Measurement

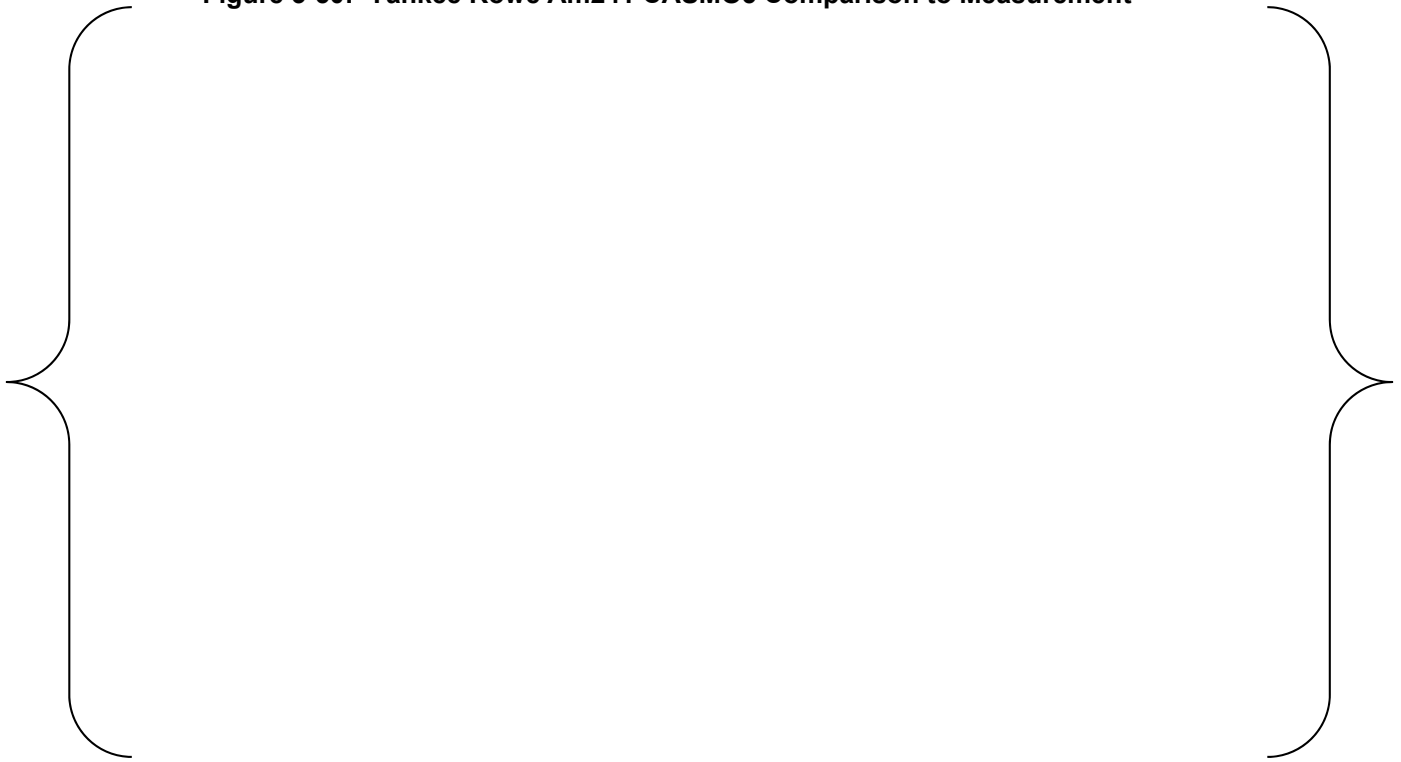


Figure 3-51: Yankee Rowe Am243 CASMO5 Comparison to Measurement



Figure 3-52: Yankee Rowe Cm242 CASMO5 Comparison to Measurement

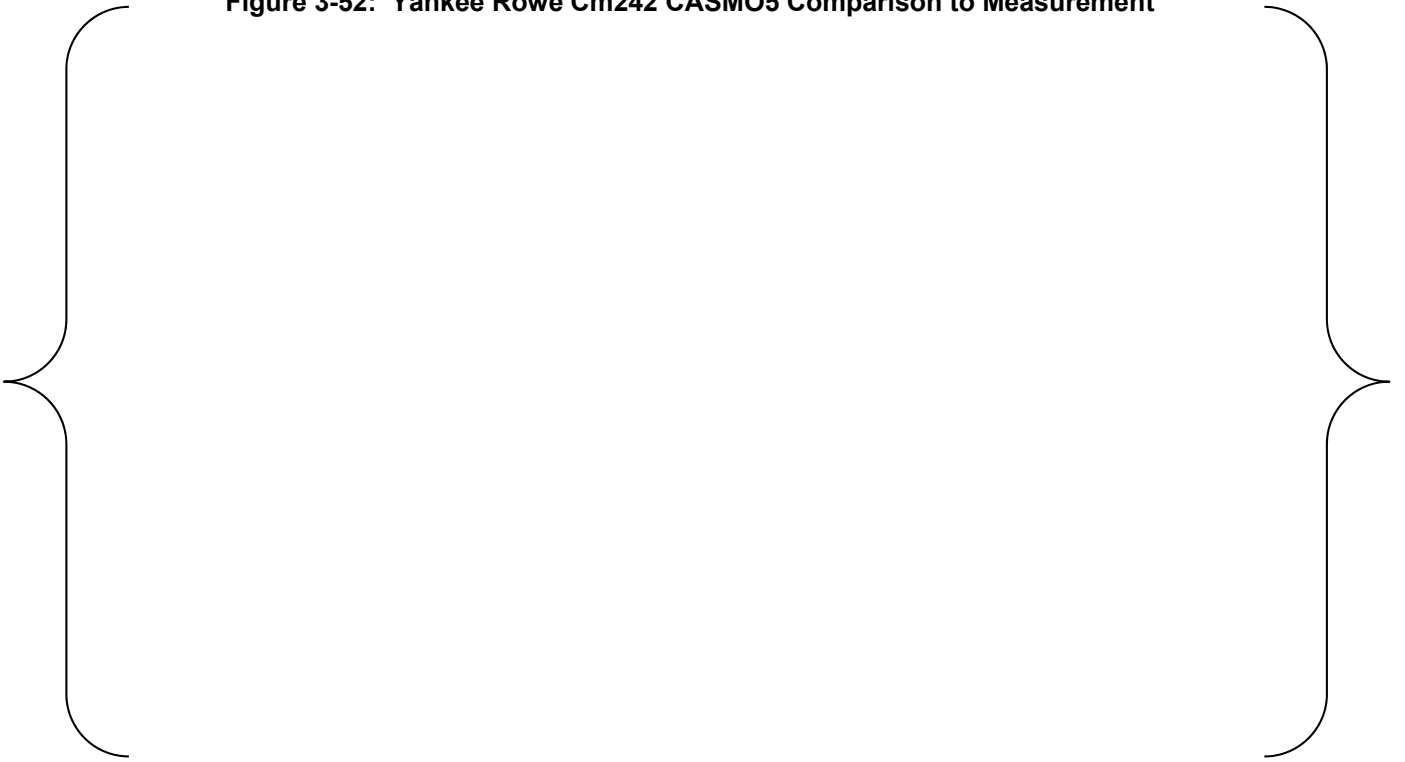


Figure 3-53: Yankee Rowe Cm244 CASMO5 Comparison to Measurement



3.2.2.2 JAERI PWR Isotopic Benchmarks

The Japan Atomic Energy Research Institute destructively analyzed samples from several burned PWR and BWR fuel pins (References 29 and 30) to measure nuclide composition for the purpose of verification of burnup codes.

An analysis was performed in CASMO5, Reference 37, to generate isotopic data for comparison to the measurements. These predictions are based on single assembly calculations depleted with power histories that correspond to the sample histories. Control rod history effects are not important for these cores.

The default option in CASMO5 simplifies some of the nuclide chains such that those leading to ^{232}U and ^{236}Pu , unimportant for reactivity and power distribution, are not complete. For comparisons to those nuclides only, the extended option is used to complete those chains. This option does not significantly impact the other nuclide concentrations.

The results of the analysis are shown in Figure 3-54 through Figure 3-66. The figures show the percent difference, calculated using equation 3.2, between the predicted and measure values. Most nuclides are represented well with some actinoids, such as Curium, resulting in larger differences.

Samples SF95-1, SF96-1 and SF97-1 were all located within a few cm of the top of the fuel pellet stack. The effects of the upper reflector region on the spectrum can be significant and is not included in the CASMO5 2-dimensional infinite lattice model.

Overall the results demonstrate that CASMO5 can reasonably predict the isotopic burnup of PWR fuel including fuel containing Gadolinia.

Figure 3-54: JAERI Isotopic Comparisons to CASMO5 for Sample SF95 Fission Products

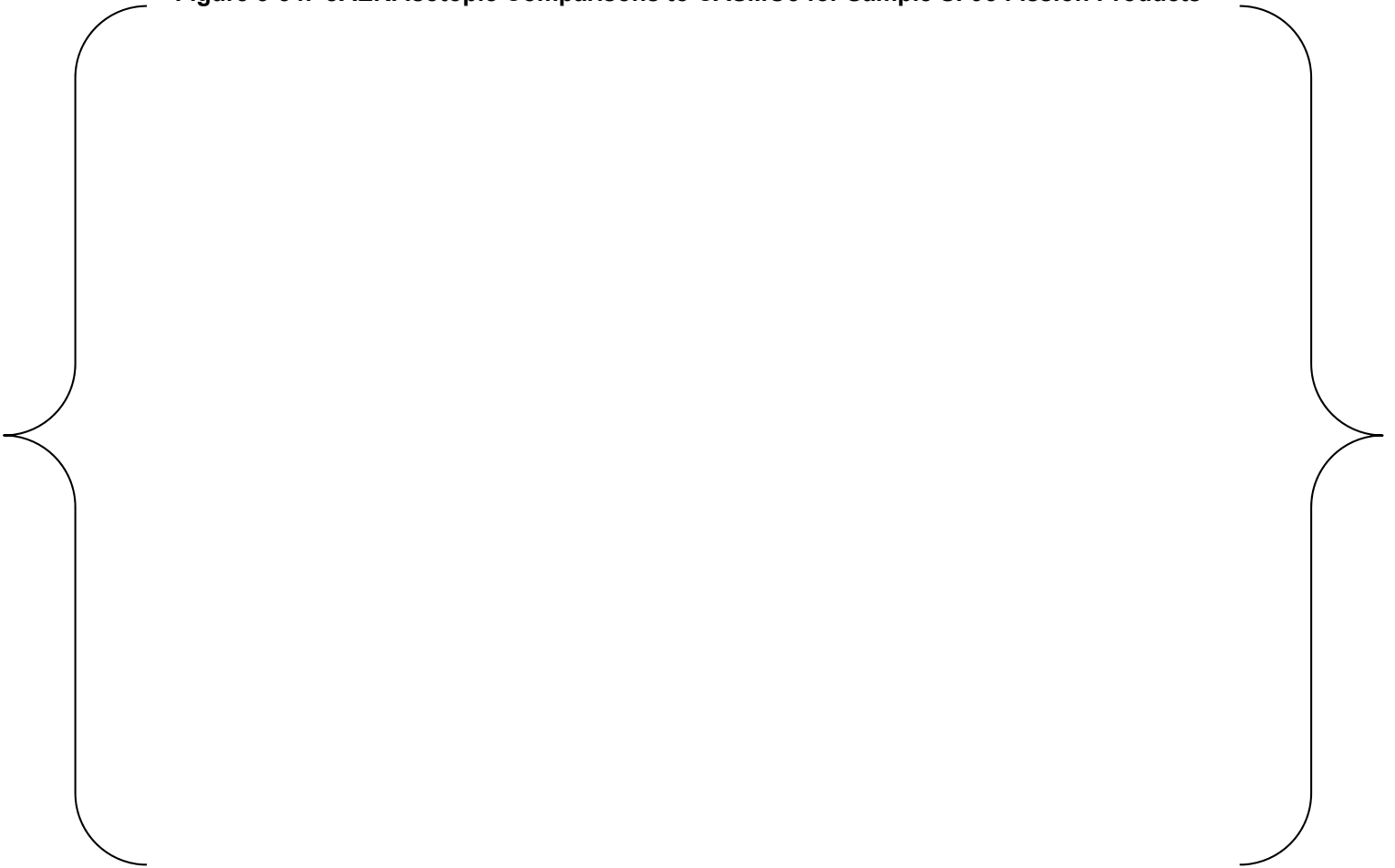


Figure 3-55: JAERI Isotopic Comparisons to CASMO5 for Sample SF95 Actinoids

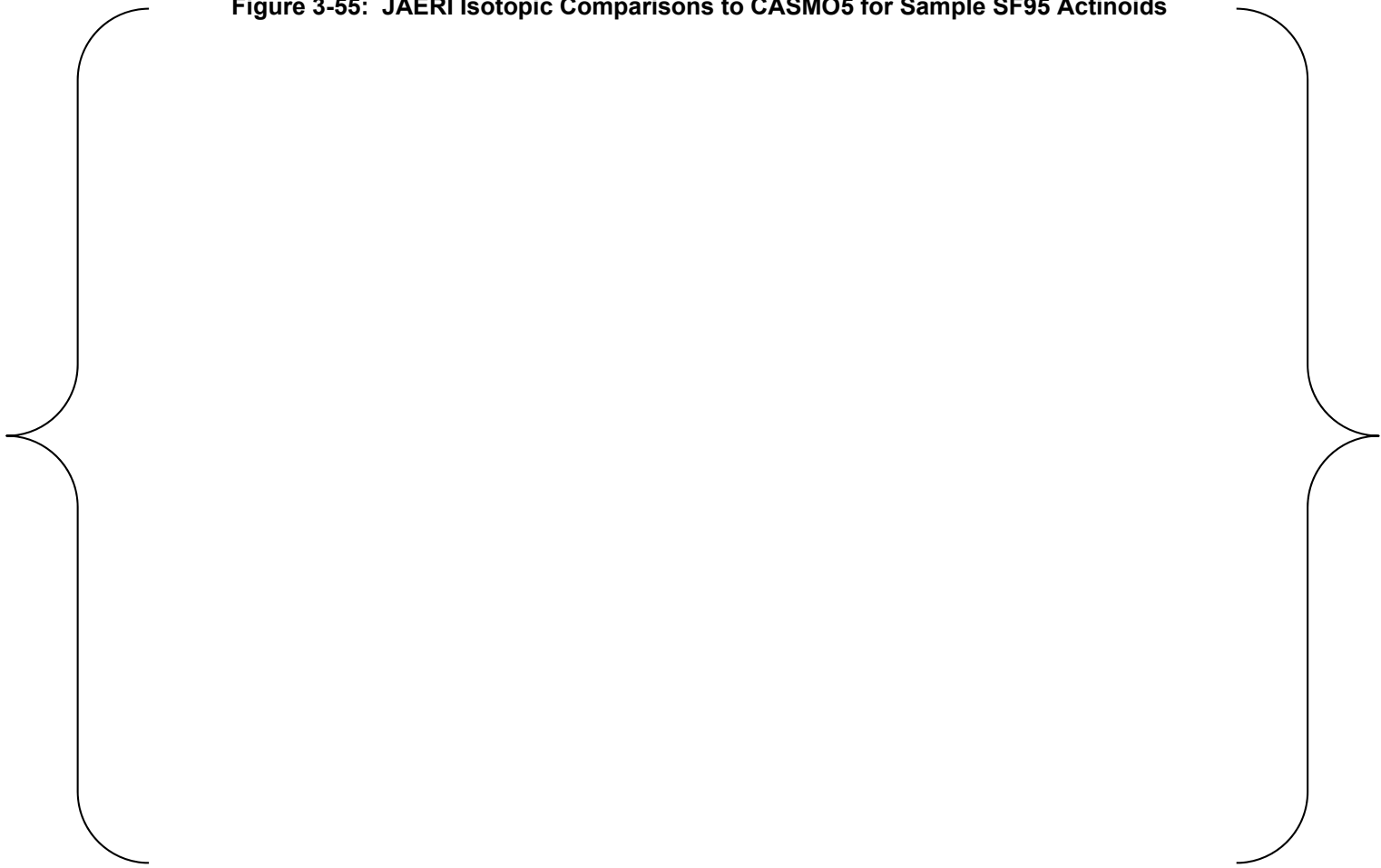


Figure 3-56: JAERI Isotopic Comparisons to CASMO5 for Sample SF96 Fission Products

Figure 3-57: JAERI Isotopic Comparisons to CASMO5 for Sample SF96 Actinoids



Figure 3-58: JAERI Isotopic Comparisons to CASMO5 for Sample SF97 Fission Products



Figure 3-59: JAERI Isotopic Comparisons to CASMO5 for Sample SF97 Actinoids

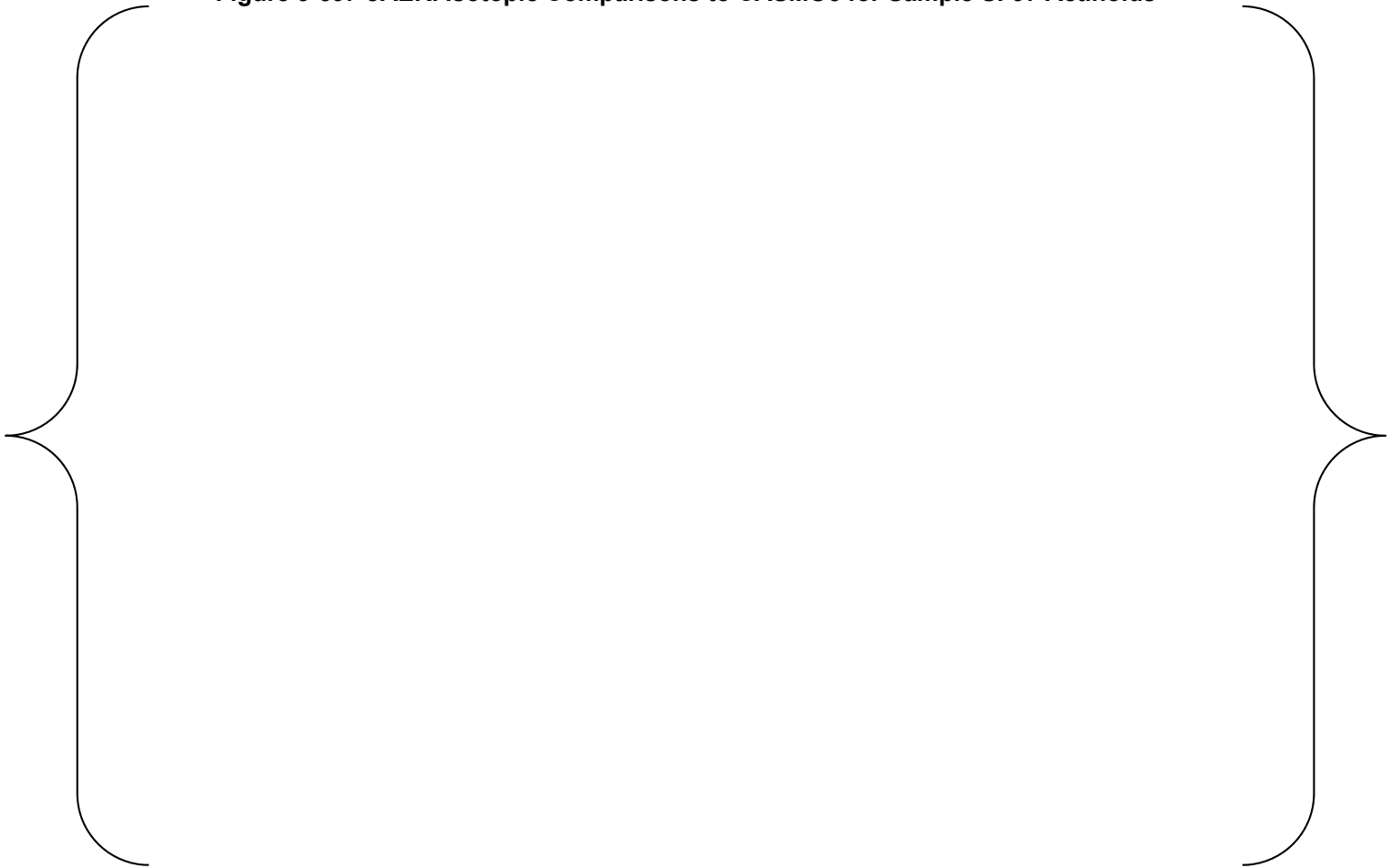
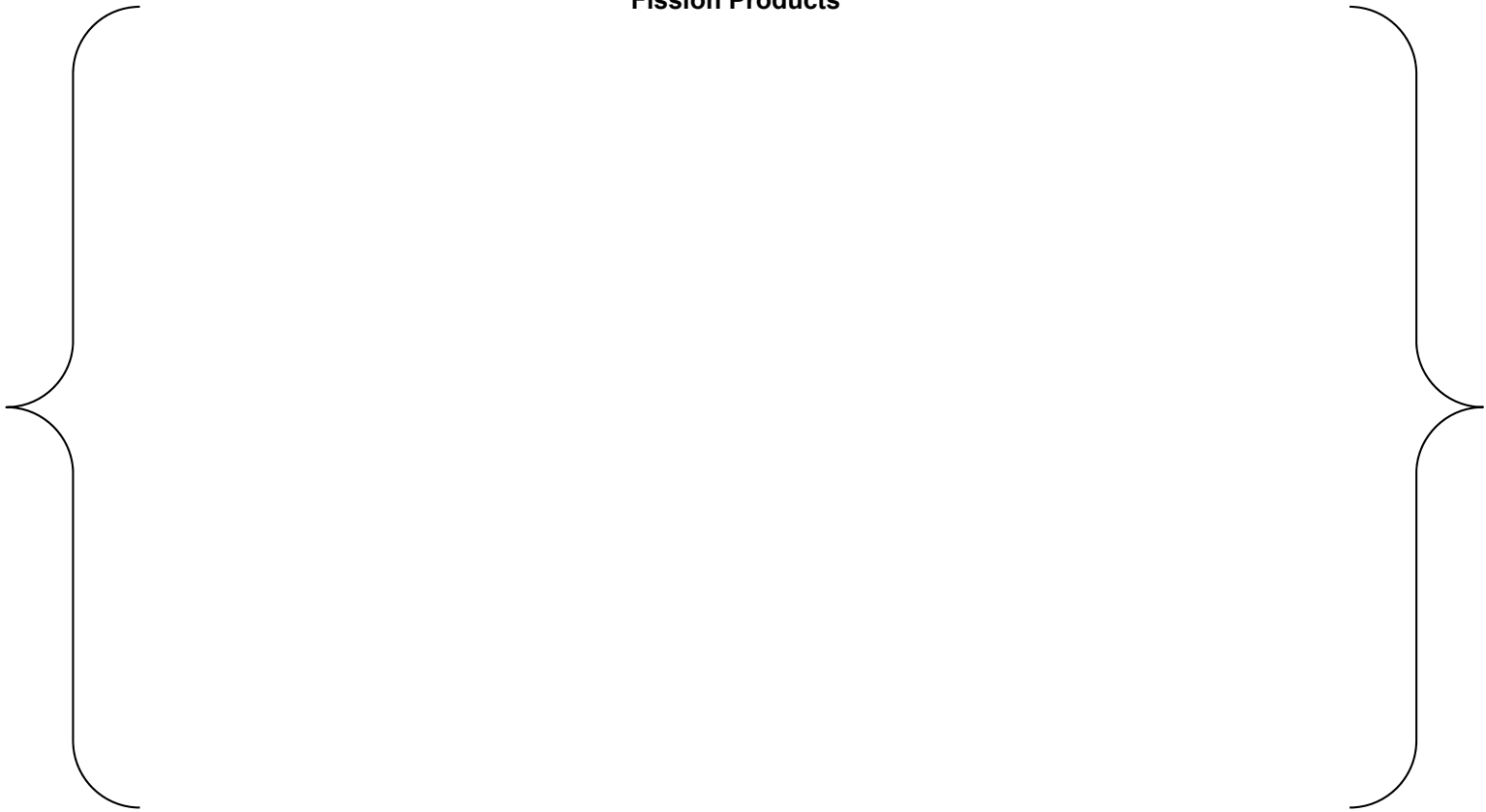


Figure 3-60: JAERI Isotopic Comparisons to CASMO5 for Sample 91E07 Fission Products

Figure 3-61: JAERI Isotopic Comparisons to CASMO5 for Sample 91E07 Actinoids

**Figure 3-62: JAERI Isotopic Comparisons to CASMO5 for Samples 89G01, 89G03 and 89G05
Fission Products**



**Figure 3-63: JAERI Isotopic Comparisons to CASMO5 for Samples 89G01, 89G03 and 89G05
Gadolinium Isotopes**

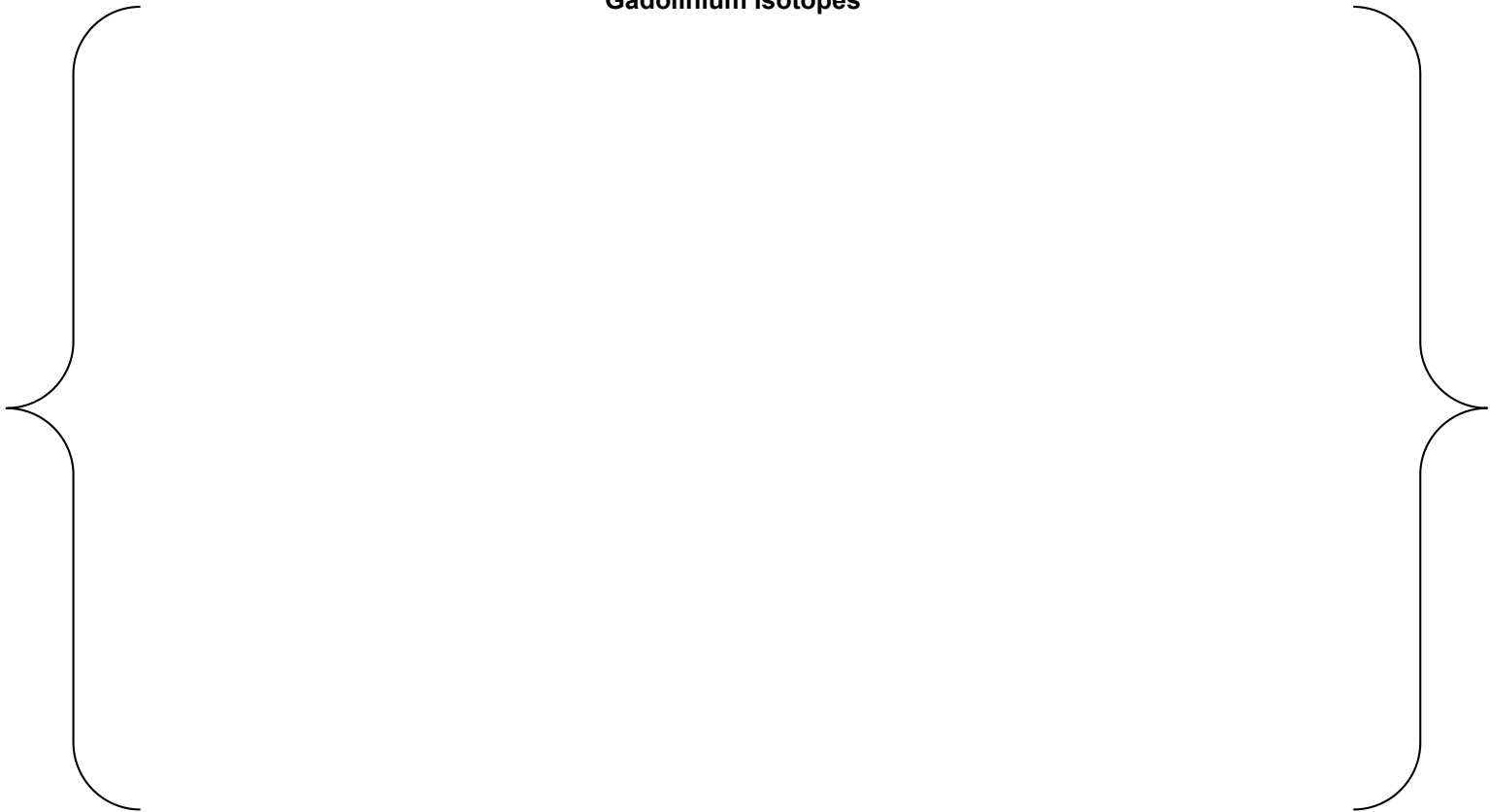


Figure 3-64: JAERI Isotopic Comparisons to CASMO5 for Samples 89G01, 89G03 and 89G05 Actinoids

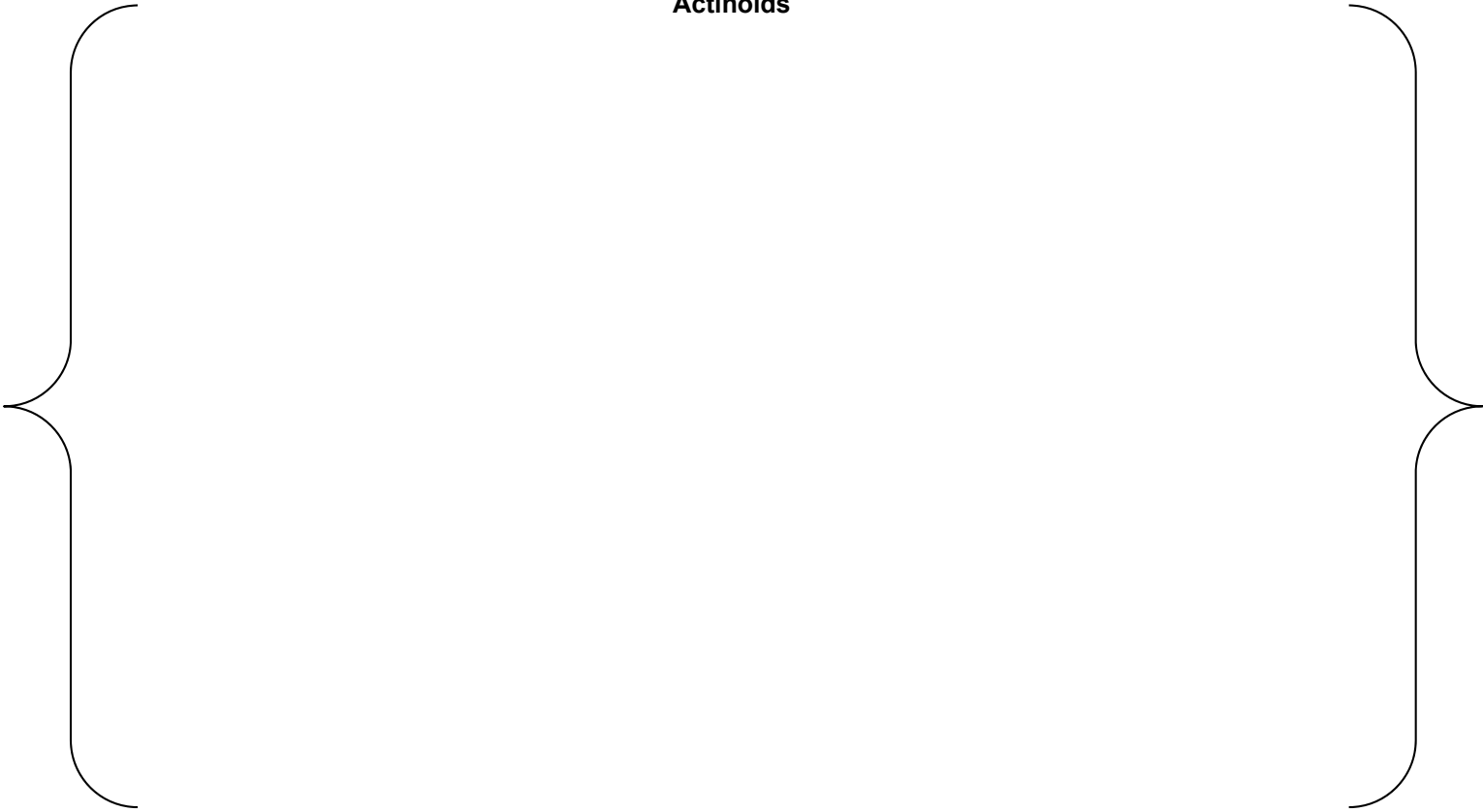


Figure 3-65: JAERI Isotopic Comparisons to CASMO5 for Samples 89G08, 89G10 Fission Products

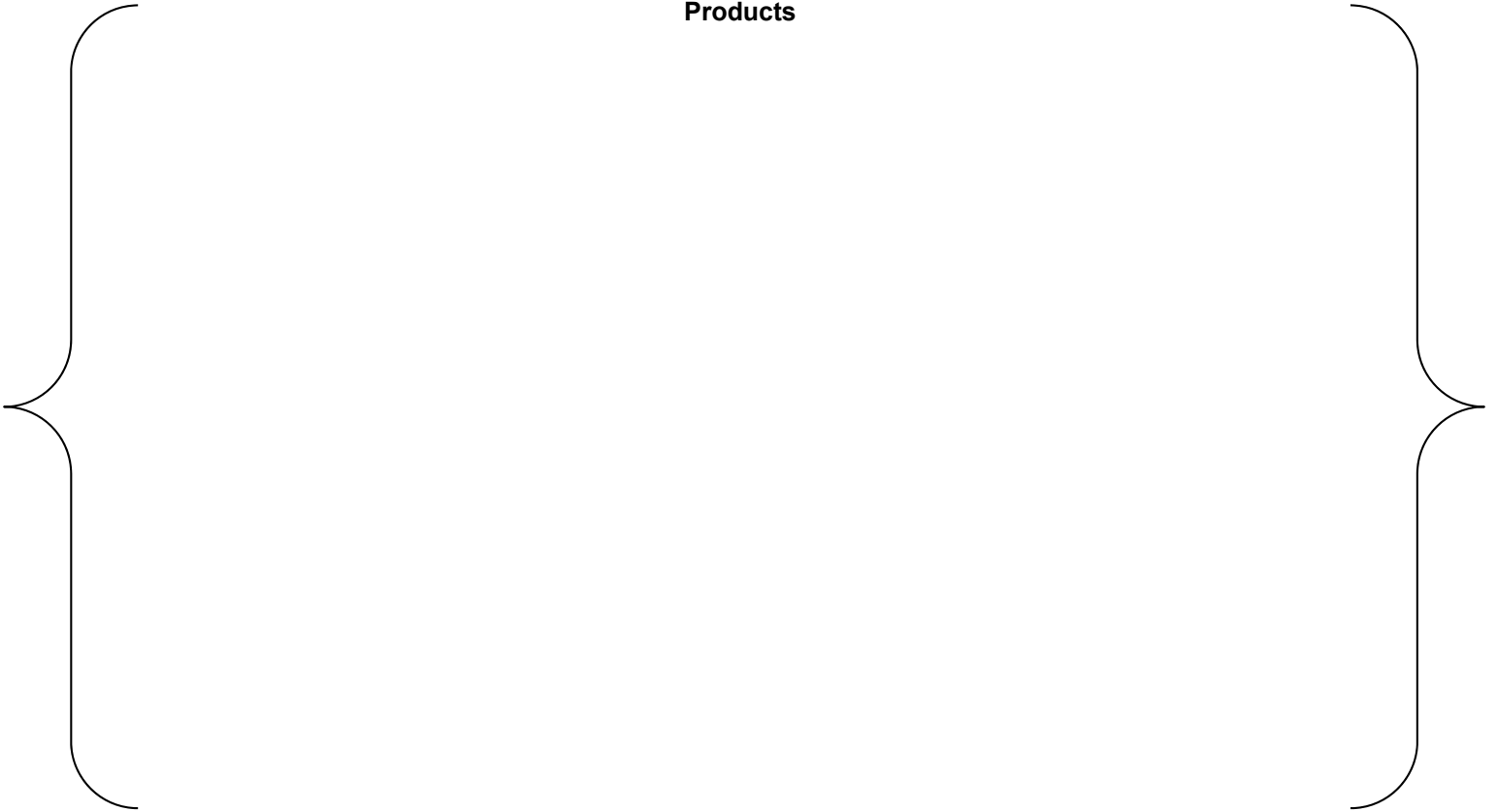
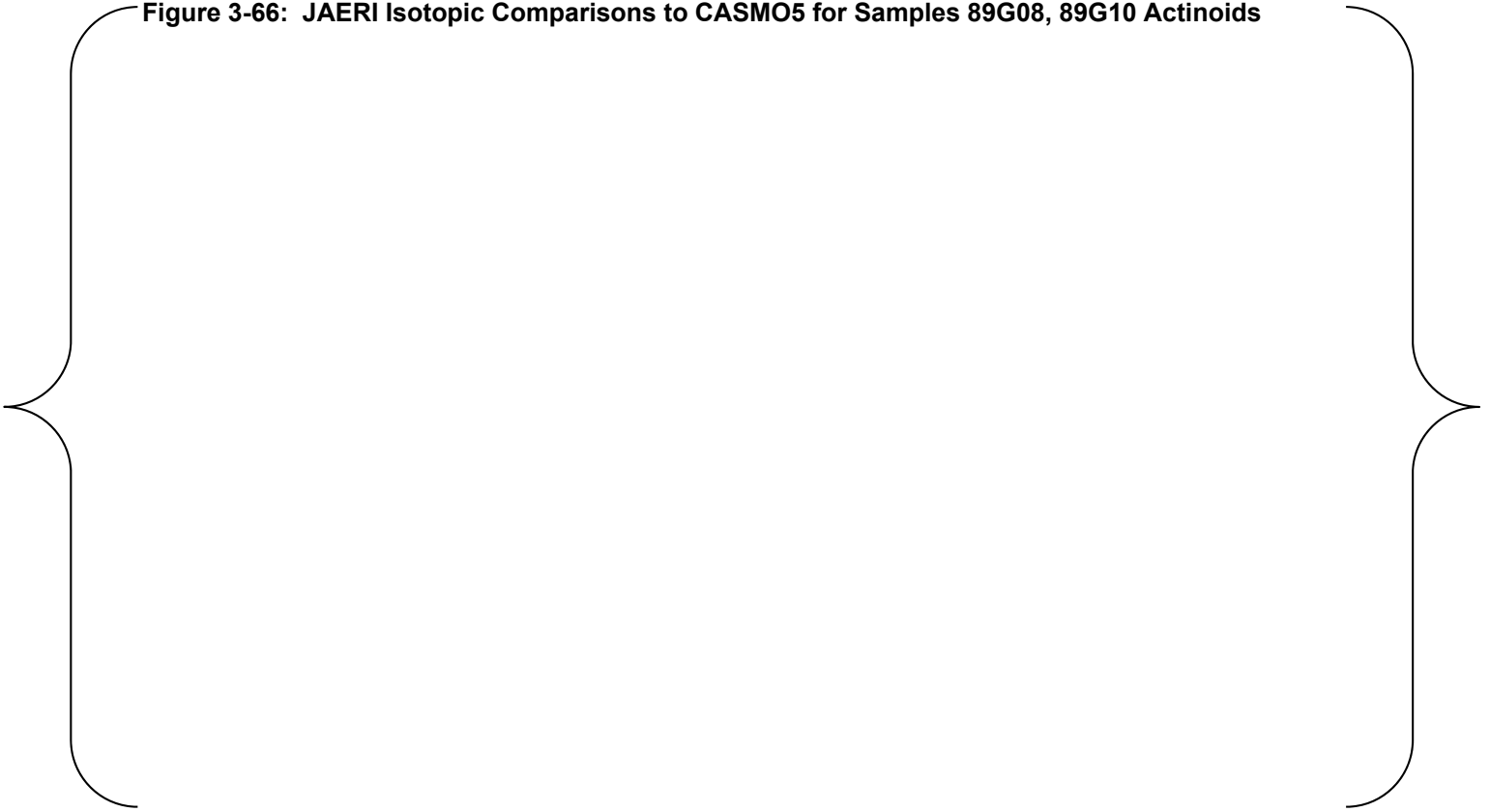


Figure 3-66: JAERI Isotopic Comparisons to CASMO5 for Samples 89G08, 89G10 Actinoids



3.3 Higher Order Code Validation and Computational Benchmarks

3.3.1 C5G7 MOX Lattice Benchmark

An OECD benchmark described in Reference 38 has been performed in CASMO5 to demonstrate the accurate implementation of the transport solution within the code.

The benchmark uses the 2D C5 computation geometry, which is a 17x17 fuel assembly lattice to construct a 16 assembly 1/4 core symmetric geometry (Figure 3-67). The cross-sections are supplied in the benchmark consisting of a 7 energy group structure.

The results of the benchmark calculation and comparisons to reference values are shown in Table 3-14 through Table 3-16. The errors in this case are calculated using equation 3.2. The very good agreement demonstrates that the transport method has been implemented correctly in CASMO5.

Figure 3-67: C5G7 Benchmark Geometry

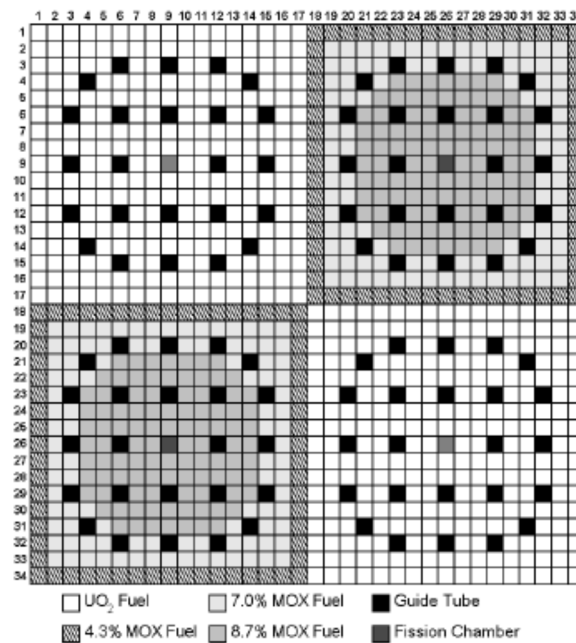


Table 3-14: CASMO5 C5G7 Eigenvalue Comparison

Code	$K_{\text{effective}}$
CASMO5	1.18650
MCNP4.1 (Ref)	1.18655

Table 3-15: CASMO5 C5G7 Power Distribution Comparison

% Error at the Maximum Pin Power Location	% Error at the Minimum Pin Power Location	Maximum % Error at any Location	% Error of Assembly Powers*
0.033	0.304	0.509	UO2 Inner = 0.034 MOX = -0.0013 UO2 Outer = -0.115

* Inner is defined as the NW assembly and outer is the SE from Figure 3-67.

Additional statistical quantities were defined in the benchmark to be calculated as a method to evaluate the quality of the power distribution calculation as a whole. These are shown in Table 3-16.

Table 3-16: CASMO5 C5G7 Power Distribution Statistics

Average Absolute Value Error	RMSE	MRE
0.134	0.005	0.110

3.3.2 MCNP6 Lattice Reactivity Comparisons

Comparison calculations have been made between CASMO5 and MCNP6 to examine the reactivity effects of different operating conditions. These include Doppler temperature defects, moderator temperature defects, soluble boron worth, and control rod worth. The calculations span a wide range of PWR lattice designs and conditions as listed below.

- Lattice Designs: 14x14, 15x15, 17x17, 14x14 CE
- Boron concentrations (ppm): 0 - 2500
- Fuel enrichment (wt% U-235): 2.5 - 5.0
- Moderator temperature (F): 70 - 620
- Fuel temperature (K): 293 - 1200
- Removable / Discrete BP type: PYREX, WABA, Discrete B₄C (CE)
- Integral BP Gadolinia (wt% Gd): 2.0 - 8.0
- Integral BP IFBA (ZrB₂) (mg/cm B10): 1.5 - 3.0
- Control rod absorber type: AIC, B₄C, HAF, W

The analysis is performed to augment the measured data compared earlier. Given that experimental data is not available over the range of conditions listed above, the use of Monte-Carlo and continuous energy cross-sections is the next best reference.

The two codes are compared with consistent nuclear data (i.e. ENDF-B-VII-R1) to provide insight into any significant modeling differences. The results presented in Table 3-17 through Table 3-20 and show reasonable agreement between CASMO5 and MCNP6.

A small negative bias in the reactivity worth of most absorber types is observed, which indicates the MCNP6 worth is slightly higher at the fresh fuel conditions analyzed. The Moderator Temperature and Doppler defects are compared in Figure 3-68 and Figure 3-69 respectively and show little trend. No other trends were noted with other variables.

The lattice reactivity comparisons with MCNP6 show there are no large systematic biases that need to be addressed before providing the CASMO5 data to SIMULATE5.

Additional comparisons for IFBA are presented since there is an absence of obtainable critical experiment data to validate against. The comparisons between CASMO5 to MCNP6 are used to show that CASMO5 calculations that contain IFBA perform as well as other materials. These include the single assembly comparisons of the total fission rate on a normalized basis. The comparisons for two 15x15 lattice designs at hot conditions are shown in Figure 3-70 and Figure 3-71. The comparisons for two 17x17 lattice designs at hot conditions are shown in Figure 3-72 and Figure 3-73. The figures show the SE symmetric octant of the lattice. A summary of the results using all pins in the lattice is shown in Table 3-21 and shows excellent agreement between CASMO5 and MCNP6.

Table 3-17: CASMO5 BOL Reactivity Benchmark vs. MCNP6, Global Perturbations

Parameter	Lattice Configuration	Average Relative Error (%)	Std. Deviation of Relative Error (%)	Number of Observations
Soluble Boron Worth	17x17	{ }	{ }	60
	15x15	{ }	{ }	60
	14x14 (W)	{ }	{ }	60
	14x14 (CE)	{ }	{ }	60
Moderator Temp. Defect	17x17	{ }	{ }	6
	15x15	{ }	{ }	6
	14x14 (W)	{ }	{ }	6
	14x14 (CE)	{ }	{ }	5
Fuel Temperature (Doppler) Defect	17x17	{ }	{ }	6
	15x15	{ }	{ }	6
	14x14 (W)	{ }	{ }	6
	14x14 (CE)	{ }	{ }	6

Table 3-18: CASMO5 BOL Reactivity Benchmark vs. MCNP6, Control Rod Worth

Parameter	Lattice Configuration	Average Relative Error (%)	Std. Deviation of Relative Error (%)	Number of Observations
AIC Control Rods	17x17	{ }	{ }	3
	15x15	{ }	{ }	3
	14x14 (W)	{ }	{ }	3
	14x14 (CE)	{ }	{ }	3
B4C Control Rods	17x17	{ }	{ }	3
	14x14 (CE)	{ }	{ }	3
Hafnium Rods	17x17	{ }	{ }	3
Tungsten Control Rods	17x17	{ }	{ }	3

Table 3-19: CASMO5 BOL Reactivity Benchmark vs. MCNP6, Integral Absorbers

Parameter	Lattice Configuration	Average Relative Error (%)	Std. Deviation of Relative Error (%)	Number of Observations
IFBA @ 1.5 mg/cm	17x17 (16 Rods)	{ }	{ }	3
	17x17 (264 Rods)	{ }	{ }	3
	15x15 (16 Rods)	{ }	{ }	3
	15x15 (148 Rods)	{ }	{ }	3
	14x14 (16 Rods)	{ }	{ }	3
	14x14 (120 Rods)	{ }	{ }	3
IFBA @ 3.0 mg/cm	17x17 (16 Rods)	{ }	{ }	3
	17x17 (264 Rods)	{ }	{ }	3
	15x15 (16 Rods)	{ }	{ }	3
	15x15 (148 Rods)	{ }	{ }	3
	14x14 (16 Rods)	{ }	{ }	3
	14x14 (120 Rods)	{ }	{ }	3
2.0 w/o Gadolinium	17x17 (4 Rods)	{ }	{ }	3
	17x17 (16 Rods)	{ }	{ }	3
	15x15 (4 Rods)	{ }	{ }	3
	15x15 (16 Rods)	{ }	{ }	3
	14x14 (4 Rods)	{ }	{ }	3
	14x14 (12 Rods)	{ }	{ }	3
	14x14 (CE) (4 Rods)	{ }	{ }	3
	14x14 (CE) (16 Rods)	{ }	{ }	3
8.0 w/o Gadolinium	17x17 (4 Rods)	{ }	{ }	3
	17x17 (16 Rods)	{ }	{ }	3
	15x15 (4 Rods)	{ }	{ }	3
	15x15 (16 Rods)	{ }	{ }	3
	14x14 (4 Rods)	{ }	{ }	3
	14x14 (12 Rods)	{ }	{ }	3
	14x14 (CE) (4 Rods)	{ }	{ }	3
	14x14 (CE) (16 Rods)	{ }	{ }	3

Table 3-20: CASMO5 BOL Reactivity Benchmark vs. MCNP6, Discrete Absorbers

Parameter	Lattice Configuration	Average Relative Error (%)	Std. Deviation of Relative Error (%)	Number of Observations
Removable Discrete BP Rods (Pyrex)	17x17 (4 Rods)	{ }	{ }	3
	17x17 (24 Rods)	{ }	{ }	3
	15x15 (4 Rods)	{ }	{ }	3
	15x15 (20 Rods)	{ }	{ }	3
	14x14 (4 Rods)	{ }	{ }	3
	14x14 (16 Rods)	{ }	{ }	3
Removable Discrete BP Rods (Wet Annular Burnable Absorber)	17x17 (4 Rods)	{ }	{ }	3
	17x17 (24 Rods)	{ }	{ }	3
	15x15 (4 Rods)	{ }	{ }	3
	15x15 (20 Rods)	{ }	{ }	3
Fixed Discrete Burnable Absorber (B4C)	14x14 (CE) (4 Rods)	{ }	{ }	3
	14x14 (CE) (16 Rods)	{ }	{ }	3

Figure 3-68: CASMO5 vs. MCNP6 Moderator Temperature Defect

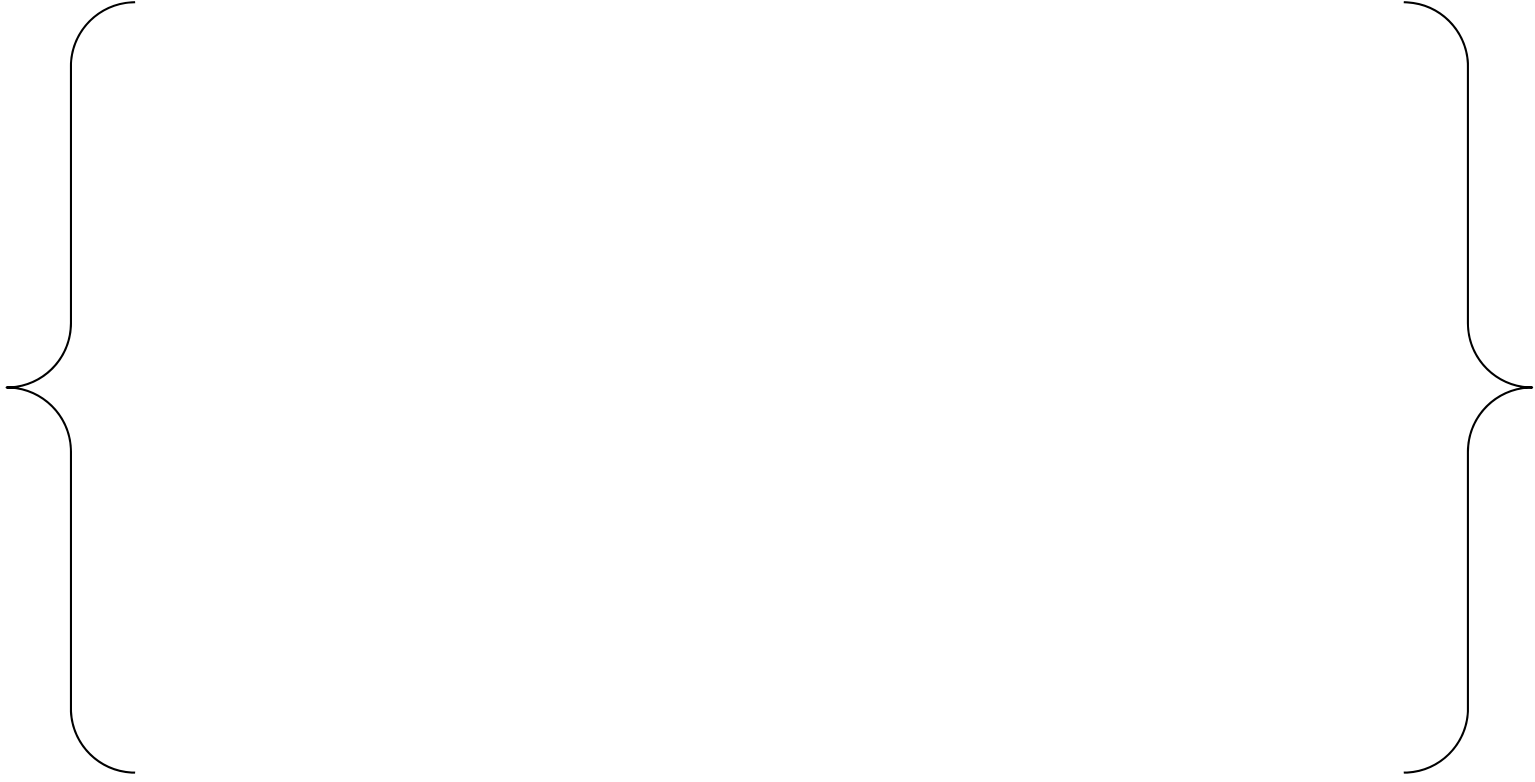


Figure 3-69: CASMO5 vs. MCNP6 Doppler Defect

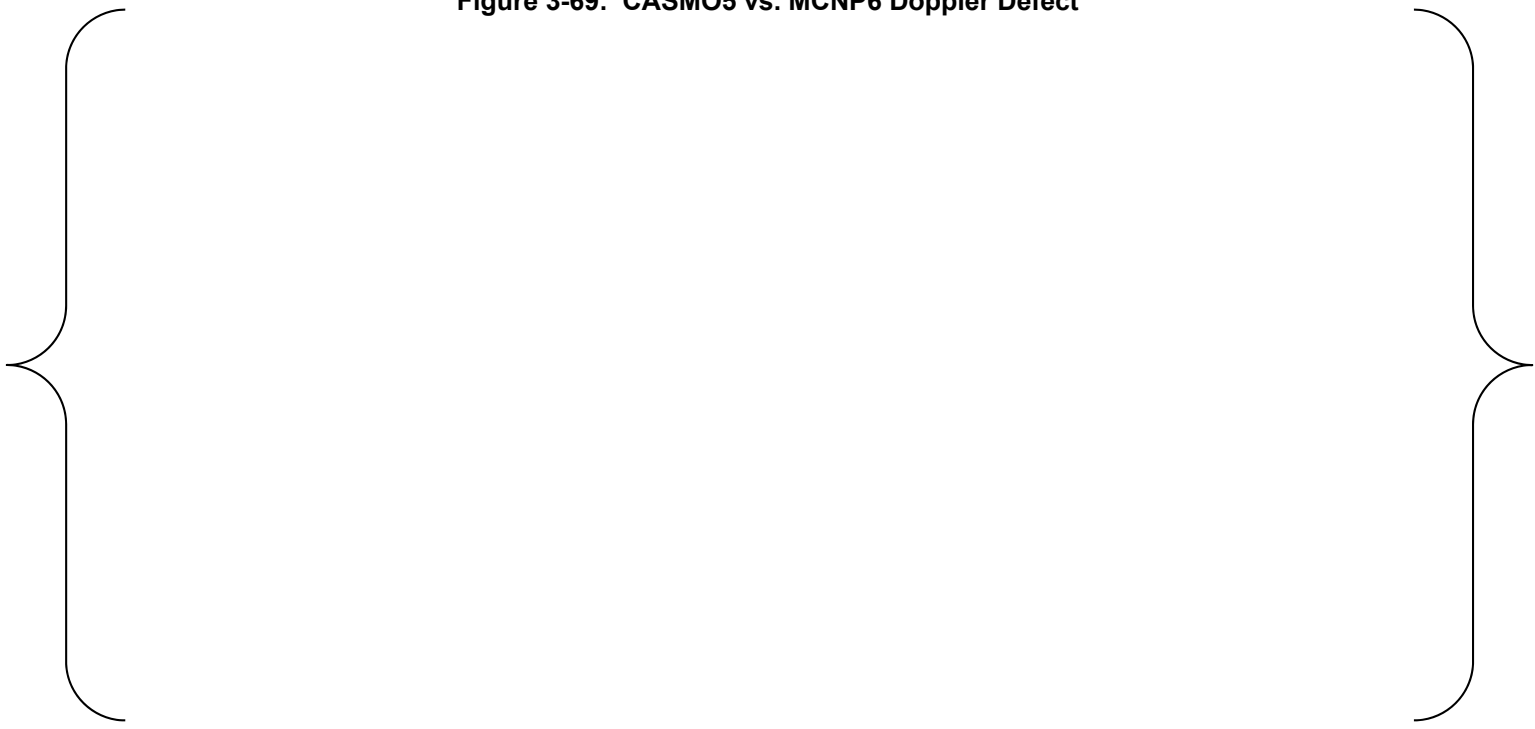


Figure 3-70: W15x15 Hot Fission Rate Comparison, 16 IFBA @ 3.0 mg/cm ¹⁰B

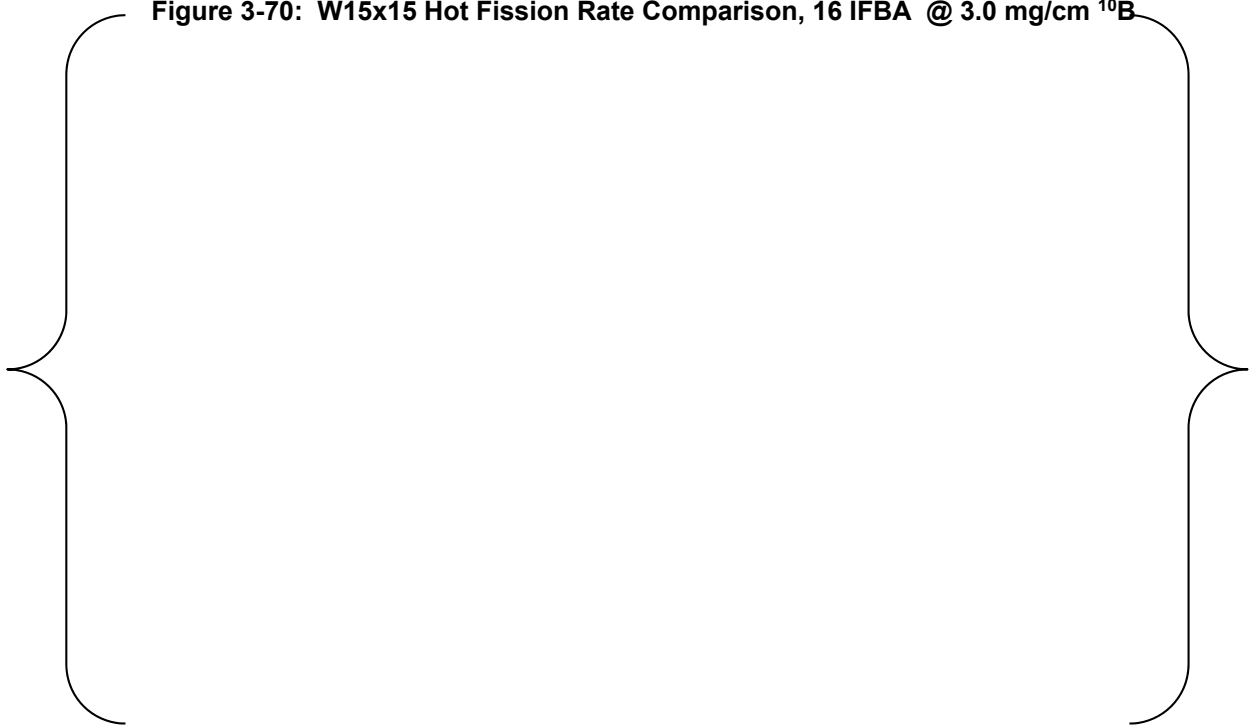


Figure 3-71: W15x15 Hot Fission Rate Comparison, 148 IFBA @ 3.0 mg/cm ¹⁰B

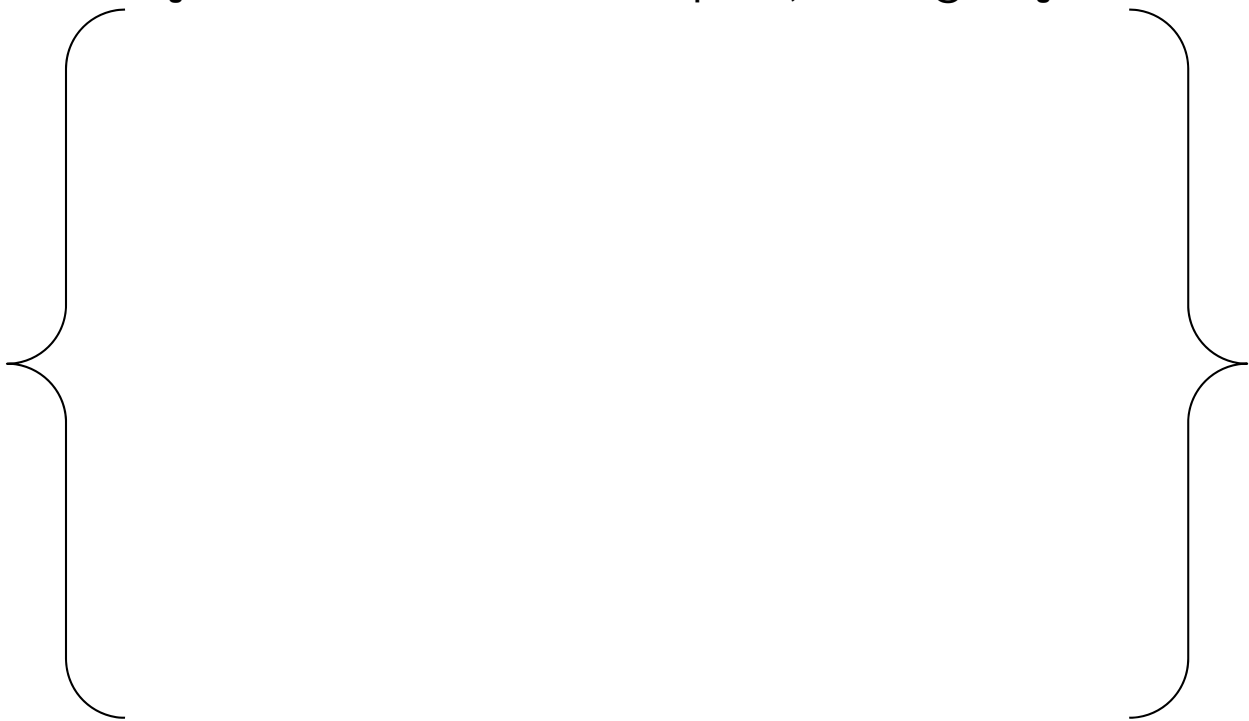


Figure 3-72: W17x17 Hot Fission Rate Comparison, 16 IFBA @ 3.0 mg/cm ¹⁰B



Figure 3-73: W17x17 Hot Fission Rate Comparison, 264 IFBA @ 3.0 mg/cm ¹⁰B



Table 3-21: IFBA Fission Rate Comparison Summary

Lattice Type	Value	Number of Points
All Lattice, All Pins		
Average Absolute Error	{ }	936
Absolute Error Standard Deviation	{ }	
15x15 Lattice, All Pins		
Average Absolute Error	{ }	408
Absolute Error Standard Deviation	{ }	
17x17 Lattice, All Pins		
Average Absolute Error	{ }	528
Absolute Error Standard Deviation	{ }	
All Lattice, IFBA Pins		
Average Absolute Error	{ }	444
Absolute Error Standard Deviation	{ }	
15x15 Lattice, IFBA Pins		
Average Absolute Error	{ }	164
Absolute Error Standard Deviation	{ }	
17x17 Lattice, IFBA Pins		
Average Absolute Error	{ }	280
Absolute Error Standard Deviation	{ }	

4 SUMMARY

The CASMO5 methods and associated data libraries have been discussed and the function of the code validated.

The methodology described in Section 2 will allow an individual to understand the information needed to properly apply CASMO5. It also provides the information in the public domain by reference to allow review of the mathematical models used.

The validation described in Section 3 demonstrates that CASMO5 performs as intended and compares well with measurements. This has been accomplished by comparing against 160 critical configurations that span the range of PWR lattice geometries, materials and conditions. The inclusion of isotopics measurements shows CASMO5 has an appropriate depletion scheme and data to handle the burnup predictions of PWR lattices. The C5G7 benchmark demonstrates that for a given set of data the transport solution in CASMO5 shows excellent agreement to the reference. And lastly CASMO5 was compared to MCNP6 over an extended range of geometric conditions and materials to demonstrate no shortcomings over operational regions that can be experienced in a PWR core.

In summary the methods and validation show that CASMO5 is suitable for modeling all PWR fuels with the following attributes:

- Pin lattice geometries ranging from 14x14 to 17x17 including both large and small water hole designs.
- Integral burnable absorbers types Gadolinia (Gd_2O_3) and IFBA (ZrB_2).
- Discrete absorber types: WABA, B_4C - AlO_3 , Boron Silicate Glass and Hafnium Suppression Rods.
- Control Rod absorber types: B_4C , Ag-In-Cd, W and Hafnium.
- Low enriched, ≤ 5.0 wt% ^{235}U , Uranium Oxide (UO_2) fuel.
- Soluble Boron in the coolant.
- In-Core Detector types of movable fission chambers and fixed designs.

5 REFERENCES

1. R. E. MacFarlane and D. W. Muir, "The NJOY Nuclear Data Processing System, Version 91, LA-12740-M," Los Alamos National Laboratory, Los Alamos, 1994.
2. R. E. MacFarlane, D. W. Muir, R. M. Boicourt and A. C. Kahler, "The NJOY Nuclear Data Processing System, Version 2012, LA-UR-12-27079," Los Alamos National Laboratory, Los Alamos, 2012.
3. J.D. Rhodes, R. M. Ferrer, and J. Hykes, "CASMO5 A Fuel Assembly Burnup Program User's Manual", SSP-07/431 Rev 8, Waltham, MA, 2013.
4. D. Knott and A. Yamamoto, "Lattice Physics Computations", *Handbook of Nuclear Engineering*, Springer, pp. 913-1239, 2010.
5. R. Stamm'ler, J. Blomstrand, and Z. Weiss, "Equivalence Relations for Resonance Integral Calculations", *Journal of Nuclear Energy*, vol. 27, p. 885, 1973.
6. R. Stamm'ler and M. J. Abbate, *Methods of Steady-State Reactor Physics in Nuclear Design*, Academic Press London, 1983.
7. J. Rhodes, K. Smith, and D. Lee, "CASMO-5 Development and Applications", PHYSOR 2006, Vancouver, BC, Canada, 2006.
8. D. Lee, K. Smith, and J. Rhodes, "The Impact of ^{238}U Resonance Elastic Scattering Approximations on Thermal Reactor Doppler Reactivity", *Annals of Nuclear Energy*, Vol. 36, pp. 274-280, 2009.
9. I. Carlvik, "A Method for Calculating Collision Probabilities in General Cylindrical Geometry and Applications to Flux Distributions and Dancoff Factors", in *U.N. International Conference on the Peaceful Uses of Atomic Energy*, Geneva, 1965.
10. R. Ferrer, J. Rhodes, and K. Smith, "Linear Source Approximation in CASMO5", PHYSOR 2012, Knoxville, TN, USA, 2012.
11. A. Yamamoto, M. Tabuchi, N. Sugimura, T. Ushio, and M. Mori, "Derivation of Optimum Polar Angle Quadrature Set for the Method of Characteristics Based on Approximation Error for the Bickley Function", *Journal of Nuclear Science and Technology*, vol. 44, No. 2, p. 129-136, 2007.
12. K. Smith and J. Rhodes, "Full-Core, 2-D, LWR Core Calculations with CASMO-4E", PHYSOR 2002, Seoul, 2002.
13. M. Pusa, "Rational Approximation to the Matrix Exponential in Burnup Calculations," *Nucl. Sci. Eng.*, vol. 169, no. 2, pp. 155-167, 2011.
14. J. Hykes and R. Ferrer, "Solving the Bateman Equations in CASMO5 Using Implicit ODE Numerical Methods for Stiff Systems", International Conference on Mathematics and Computational Methods Applied to Nuclear Science and Engineering (M&C 2013), Sun Valley, 2013.

15. M. Pusa, *Numerical Methods for Nuclear Fuel Burnup Calculations*, Aalto University, 2013.
16. R. J. Tuttle, "Delayed Neutron Yields in Nuclear Fission", *INDC Proceedings of the Consultants' Meeting on Delayed Neutron Properties*, Vienna, 1979.
17. A. F. Henry, *Nuclear-Reactor Analysis*, Cambridge, MA, MIT Press, 1975.
18. K. Smith, A. F. Henry, and R. A. Loretz, "The Determination of Homogenized Diffusion Theory Parameters for Coarse Mesh Nodal Analysis", *Proceedings of the Conference on Advances in Reactor Physics and Shielding*, Sun Valley, 1980.
19. K. Smith, "Spatial Homogenization Methods for Light Water Reactor Analysis", Ph.D. Thesis, Department of Nuclear Engineering, Massachusetts Institute of Technology, 1980.
20. J. Umbarger and A. S. Digiovine, "SIMULATE-3 User's Manual", Studsvik/SOA-92/01, Studsvik of America, Newton, MA, 1992.
21. T. Bahadir and S-O Lindahl, "Studsvik's Next Generation Nodal Code SIMULATE5", *Proc. Int. Conf. 2009 Advanced in Fuel Management IV*, Hilton Head Island, SC USA, April 12-15, 2009.
22. L.W. Lewman, "Urania-Gadolinia: Nuclear Model Development and Critical Experiment Benchmark," B&W 1810, DOE/ET/34212-41, Babcock & Wilcox, 1984.
23. M.N. Baldwin et. al., "Critical Experiments Supporting Close Proximity Water Storage of Power Reactor Fuel," BAW-1484-7, Babcock & Wilcox, 1979.
24. NEA/NSC/DOC(95)03/IV, LEU-COMP-THERM-055, "Light-Water Moderated and Reflected Low-Enriched Uranium (3 wt.% U235) Dioxide Rod Lattices".
25. E. Johansson *et al.*, "KRITZ-3 Experiments", Internal Report, AB Atomenergi, Studsvik, Sweden, 1973.
26. Y Tahara *et al.*, "Reactivity Effect of Iron Reflector in LWR Cores", *Nuclear Science and Technology*, Vol. 28, No.2, p. 102-111.
27. R. J. Nodvik *et al.*, "Evaluation of Mass Spectrometric and Radiochemical Analyses of Yankee Core 1 Spent Fuel", WCAP-6068, 1966.
28. R. J. Nodvik *et al.*, "Supplementary Report on Evaluation of Mass Spectrometric and Radiochemical Analyses of Yankee Core I Spent Fuel, including Isotopes of Elements Thorium through Curium", TID 4500, WCAP-6086, 1969.
29. K. Suyama *et al.*, "Re-evaluation of Assay Data of Spent Nuclear Fuel Obtained at Japan Atomic Energy Research Institute for Validation of Burnup Calculation Code Systems," *Annals of Nuclear Energy*, Vol. 38, p. 930 941, 2011.

30. K. Suyama *et al.* , "Nuclide Composition Benchmark Data Set for Verifying Burnup Codes on Spent Light Water Reactor Fuels," Nuclear Technology, Vol 137, p 111-126, 2002
31. NEA/NSC/DOC(2003)16, "Benchmark on Deterministic Transport Calculations Without Spatial Homogenisation, A 2-D/3-D MOX Fuel Assembly Benchmark"
32. E. Wehlage, "Modeling of the B&W 1810 Series of Critical Experiments in CASMO5," SSP-14-P01/003-C, 2014
33. B. Haugh, "Modeling of the B&W 1484 Criticals in CASMO5," SSP-14-P01/011-C, (2014)
34. M. Kruners, "Modeling of the KRITZ-3 Critical Experiment in CASMO5, " SSP-14-P01/002-C, 2014
35. B. Haugh, "Modeling of the AEA Winfrith Dimple Critical Experiments in CASMO5," SSP-14-P01/001-C, 2014
36. D. Dean, "Yankee Rowe PWR Isotopic Benchmark," SSP-14-P01/007-C, 2014
37. D. Dean, "JAERI PWR Isotopic Benchmark," SSP-14-P01/008-C, 2014
38. NEA/NSC/DOC(2003)16 "Benchmark on Deterministic Transport calculations without spatial homogenization A 2-D/3-D MOX fuel assembly Benchmark", ISBN 92-64-02139-6
39. B. Haugh, "C5G7 2D Benchmark Calculation with CASMO5," SSP-14-P01/006-C, 2014
40. E. Wehlage, "MCNP6 Lattice Reactivity Comparison to CASMO5," SSP-14-P01/009-C, 2014
41. S. Vanevenhoven, "TCA Reflector Critical Experiment Analysis in CASMO5," SSP-14-P01/005-C, 2014